Department of Applied Physics

Nanoscale Friction of Ice

Nino Samadashvili

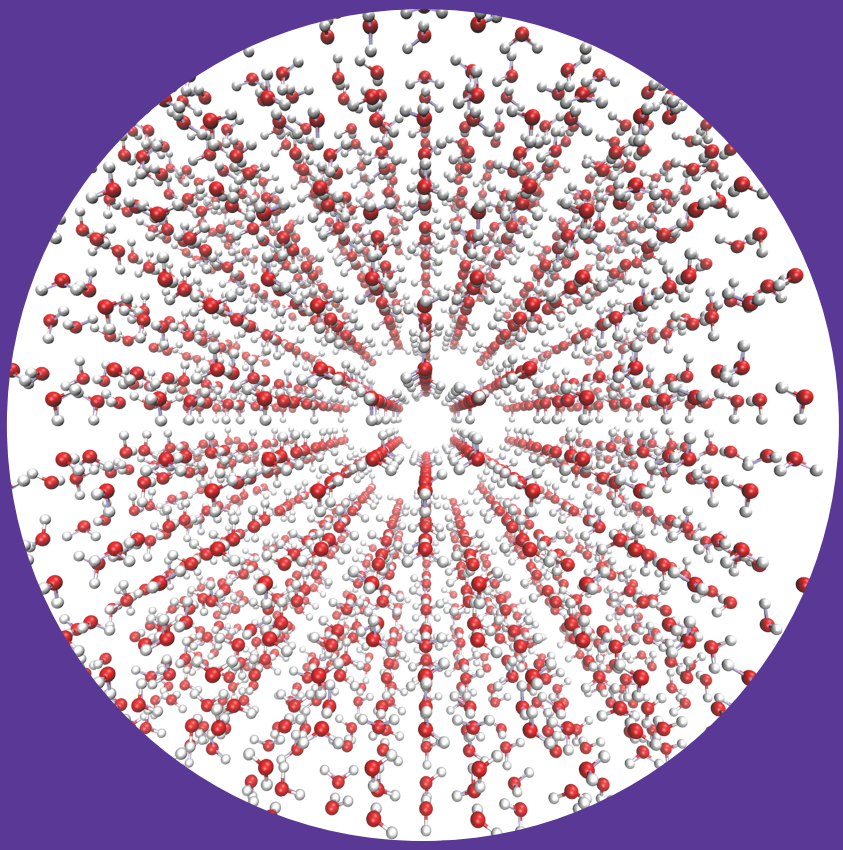

Aalto University

DOCTORAL DISSERTATIONS

Aalto University publication series
DOCTORAL DISSERTATIONS 217/2013

Nanoscale Friction of Ice

Nino Samadashvili

A doctoral dissertation completed for the degree of Doctor of Science to be defended, with the permission of the Aalto University School of Science, at a public examination held at the lecture hall F239a Auditorium of the school on 6 February 2014 at 13:00.

Aalto University
Aalto University School of Science
Department of Applied Physics
Surfaces and Interfaces at the Nanoscale

Supervising professor
Adam S. Foster

Thesis advisor
Adam S. Foster

Preliminary examiners
Professor Kai Nordlund
University of Helsinki, Finland

Associate Professor Ion Marius Sivebaek
Technical University of Denmark, Denmark

Opponents
Professor Lev Kantorovich
King's College London, UK

Aalto University publication series
DOCTORAL DISSERTATIONS 217/2013

ISBN 978-952-60-5509-1
ISBN 978-952-60-5510-7 (pdf)
ISSN-L 1799-4934
ISSN 1799-4934 (printed)
ISSN 1799-4942 (pdf)
http://urn.fi/URN:ISBN:978-952-60-5510-7

Images: 46

Unigrafia Oy
Helsinki 2013

Finland

Publication orders (printed book):
nino.samadashvili@aalto.fi

Aalto University

Abstract

Aalto University, P.O. Box 11000, FI-00076 Aalto www.aalto.fi

Author
Nino Samadashvili

Name of the doctoral dissertation
Nanoscale Friction of Ice

Publisher Aalto University School of Science

Unit Department of Applied Physics

Series Aalto University publication series DOCTORAL DISSERTATIONS 217/2013

Field of research Nanotribology

Manuscript submitted 21 August 2013 **Date of the defence** 6 February 2014

Permission to publish granted (date) 31 October 2013 **Language** English

☒ **Monograph** ☐ **Article dissertation (summary + original articles)**

Abstract

Friction between macroscopic surfaces sliding relative to each other has been long investigated, nevertheless it still remains one of the most complex and least understood processes in nature. In connection with the success in both experimental and theoretical fields, through the development of nanotribology offering the possibility of understanding atomic-level origins of friction, the subject continues to be re-examined.

In this work we use molecular dynamics simulations to study frictional behavior of an ice-ice system (one of the most interesting systems from friction point of view due to its unusually low friction coefficient and prevalence in life) at the nanoscale, particularly the influence of temperature, applied load and sliding velocity on calculated frictional force. We compare our results to experimental findings and discuss agreement within different ranges of parameters affecting friction. Our work provides useful insight into the field of nanoscale ice friction and can be used as a basis for future development of the field.

Keywords Ice, Friction, Nanoscale, Molecular Dynamics, TIP4P/Ice

ISBN (printed) 978-952-60-5509-1 **ISBN (pdf)** 978-952-60-5510-7

ISSN-L 1799-4934 **ISSN (printed)** 1799-4934 **ISSN (pdf)** 1799-4942

Location of publisher Helsinki **Location of printing** Helsinki **Year** 2013

Pages 116 **urn** http://urn.fi/URN:ISBN:978-952-60-5510-7

Publications

1. N. Samadashvili, B. Reischl, T. Hynninen, T. Ala-Nissilä, and A. S. Foster. Atomistic simulations of friction at an ice-ice interface. *Friction*, 1, 3, pp 242-251, 2013.

List of Conference Contributions
Oral Presentations

1. Nanoscale Interfaces with Ice, Material Research Society Spring Meeting, *San Francisco, California* 2012

2. Regelation and Surface Friction of Ice, Joint ICTP-FANAS Conference on Nanotribology, *Trieste, Italy* 2011

Poster Presentations

1. N. Samadashvili, T. Hynninen, and A. S. Foster, Nanoscale Friction of Ice, Towards Reality in Nanoscale Materials VI, *Levi, Finland* 2013

2. N. Samadashvili, T. Ala-Nissilä, T. Hynninen, C. L. Dias, and A. S. Foster, Nanoscale Friction of Ice, International Symposium on Surface Science, *Tokyo, Japan* 2012

3. N. Samadashvili, T. Ala-Nissilä, T. Hynninen, C. L. Dias, and A. S. Foster, Nanoscale Friction of Ice, Towards Reality in Nanoscale Materials V, *Levi, Finland* 2012

4. N. Samadashvili, T. Ala-Nissilä, T. Hynninen, C. L. Dias, and A. S. Foster, Nanoscale Friction of Ice, International Conference on Stick-Slip Dynamics: From Nano to Geophysical Scales, *Jerusalem, Israel* 2011

5. N. Samadashvili, T. Ala-Nissilä, T. Hynninen, C. L. Dias, and A. S. Foster, Premelting of Ice, FANAS Conference on Friction, *Saarbrücken, Germany* 2010

6. N. Samadashvili, T. Ala-Nissilä, T. Hynninen, C. L. Dias, and A. S. Foster, Premelting of Ice, Towards Reality in Nanoscale Materials IV,

Levi, Finland 2010

7. T. Hynninen, N. Samadashvili, V. Heinonen, C. L. Dias, M. Karttunen, T. Ala-Nissilä, and A. S. Foster, Cutting Ice: Nanowire Regelation, Psi-k Conference, *Berlin, Germany* 2010

8. T. Hynninen, N. Samadashvili, V. Heinonen, C. L. Dias, M. Karttunen, T. Ala-Nissilä, and A. S. Foster, Cutting Ice: Nanowire Regelation , Towards Reality in Nanoscale Materials III, *Levi, Finland* 2009

Contents

1. Introduction

A common assumption for the unusual slipperiness of ice includes the phenomena of surface premelting - the surface of ice already liquefies below its melting temperature [1–4]. Significant effort has been made to understand the properties of this liquid layer [5], particularly its thickness and atomic structure [6–9]. However, due to the complexity of understanding the nature of the surface at the atomic scale, very little work has been done to study friction or slipperiness, of ice at that scale. This contrasts strongly with the development of the field of atomic friction in general [10], with Atomic Force Microscopy (AFM) offering the possibility of characterizing the contact between a few atoms in the tip and the ice surface.

Despite the importance of ice-ice friction and its relevance to understanding the surface properties of ice, studies of ice friction have been mainly limited to heterogeneous materials [11–17]. The friction of ice on ice has received little attention - the few existing experimental studies show generally low coefficients of friction (from 0.05 up to 1.6) at temperatures close to the melting point, with a clear dependence on the sliding velocity and temperature [18–24]. However, low temperature studies at high pressure showed minimal dependence on temperature and velocity [25].

Due to the lack of theoretical studies of ice friction, and ice-ice friction in particular, the aim of this work is to systematically build a model of an ice-ice interface between two hexagonal ice (Ih) surfaces and use extensive molecular dynamics simulations to simulate in detail the mechanics of ice during friction. In order to directly compare with previous experimental studies, we calculate the frictional properties as a function of temperature, sliding velocity and load.

2. Friction

Pursuing the study of friction is not a recent scientific activity. On the contrary, due to the engineering aspects, investigation of friction, lubrication, adhesion and wear has a long history. By 200,000 B. C., Neanderthals were using friction to generate fire by rubbing wood on wood. Examples of the simple drill, in which a stick revolves between the palms, can be found in several of the earliest civilizations.

In early days (1880 B.C.), Egyptians were trying to solve problems arising while transporting very heavy things, such as large stone blocks and carved figures used in the construction of pyramids and palaces, by using lubricants [26].

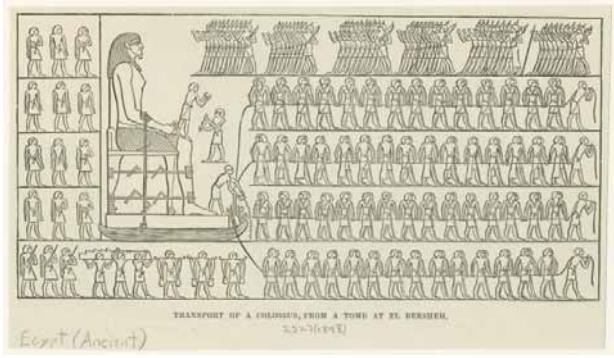

Figure 2.1. Transporting an Egyptian colossus. Painting from the tomb of Tehuti-Hetep, El-Bershed (1880 B.C.). Adapted from ref. [26]

The Egyptian method of moving a large stone statue is illustrated in Fig. 2.1, where the colossus is placed on a sledge. Instead of using rollers or levers, an old Egyptian is standing at the front of the pedestal pouring lubricant from a jar on to the ground immediately in front of a sledge.

In summary, techniques developed by early civilizations (Mesopotamia and Egypt, 3500 B. C.) that are of great tribological significance are listed below:

1. Drills developed for making fire and drilling holes.

2. The *potter's wheel* employing simple pivot bearings made from wood or stone was produced to facilitate the throwing of clay at relatively high rotational speed.

3. The wheeled vehicle.

4. Lubricants used in a number of applications involving rotation and translation.

5. Transportation of heavy stone statues and building blocks on sledges.

The field of tribology (another word for friction, wear; Originally comes from Greek and its direct translation would be "the science of rubbing".) has been developed since those days, considering how much we encounter tribological phenomena in our daily lives and technology [26–31].

The first qualitative studies of friction date back to Leonardo da Vinci (1452-1519). His contribution to the subject of friction, the development of bearing materials, studies of wear and ingenious schemes for rolling-element bearing, has a great scientific importance. A selection of Leonardo's notes demonstrate his recognition of the difference between rolling and sliding friction and the beneficial effect of lubricants.

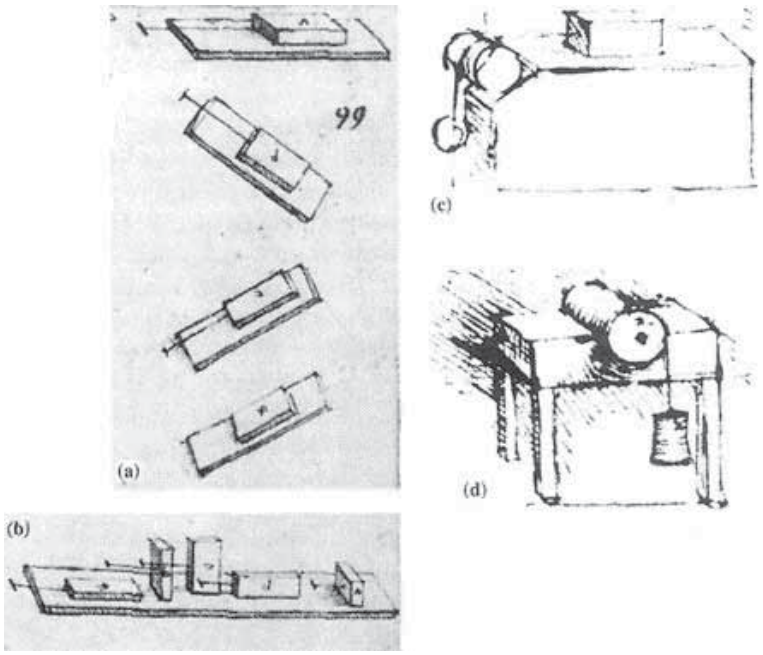

Figure 2.2. Leonardo da Vinci's studies of friction. (a) the force of friction between horizontal and inclined planes; (b) the influence of the apparent contact area upon the force of friction; (c) the force of friction on a horizontal place by means of a pulley; (d) the friction torque on a roller and half bearing. Adapted from ref. [26]

After studying sliding friction and its dependence on the area of contact and applied load he proposed two laws of friction, which later on were proved by the French physicist Guillaume Amonton (1663-1705) [27].

The laws of friction postulated by Leonardo da Vinci state that the force of friction is directly proportional to the applied load and the force is independent of the apparent area of contact for a given load. Leonardo's statements are the first recorded scientific studies of friction and the first statement in scientific history of laws governing the phenomena of friction.

Later on, Charles Augustin Coulomb (1736-1806) formulated the frictional force as an equation:

$$F = \mu F_N \tag{2.1}$$

where F and F_N are the frictional and normal forces, respectively, and μ is known to be the coefficient of friction which, based on observations, is often nearly velocity independent, in cases where the thermal activation can be neglected [28]. There is another law for the friction coefficient which states that μ is also independent of the apparent area of contact. This means that for the same load, the friction experienced upon sliding will be the same for a small block as for a large one.

Various experimental methods have been developed over the years to measure frictional force between sliding surfaces [27, 28, 32–40]. Almost all sliding devices include a finite mass M, and some elastic spring attached to it.

Figure 2.3. A block sliding on a flat substrate. A spring is attached to the block and the "free" end of the spring moves with the velocity v_s.

The free end of the spring is moving either with a constant velocity or with a velocity that varies over time. In case of a steady (constant velocity) sliding, the spring force increases linearly with time up to some threshold F_S value that needs to be overcome in order to initiate lateral motion

(this threshold force is known as the static frictional force F_S, while a minimum force that must be applied to keep the object moving is the kinetic frictional force F_K) [29, 41, 42]. In such a case, the spring force is equivalent to the frictional force. The motion of the block is either steady or shows stick-slip behavior depending on the surface structural properties of the materials, sliding velocity and elastic properties of the spring. The steady motion of the block is achieved when either the sliding velocity is high or the spring attached is stiff enough, while a periodic/chaotic stick-slip occurs when the spring force oscillates and it is not directly associated with the frictional force. Generally, even if the center of mass of the body is moving steadily, local stick-slip can occur at the interface between some group of molecules. Therefore, macrotribology has to be separated from micro or nanotribology. Cases where we have large mass transport which is associated with occurrence of wear and influence from the bulk material are addressed in macrotribology. However, nanotribology strongly depends on the material's surface and operates under very light loads.

Generally, the friction force can be calculated by integrating the shear stress over the area of real contact ΔA [28]. However, due to the surface roughness, which is present usually on many different length scales, calculation of ΔA is not straightforward.

When two surfaces of a material come into contact, a single contact area (junction) is formed. If the pressure, perpendicular to the contact area, starts to increase, more junctions are formed and the net area of these junctions is referred to as the area of real contact. Assuming that plastic deformation occurs at each junction after bringing the surfaces together and they are in a state of plastic flow, taking into account the penetration hardness of the material, one can easily calculate the real area of contact, which is given by:

$$\Delta A = L/\sigma_c \tag{2.2}$$

where L is the applied load and σ_c is the penetration hardness, or in other words the largest compressive stress that the material can withstand without plastic deformation. However, if the pressure on junctions is lower than the penetration hardness, the above formulation becomes inaccurate. This is usually the case for very smooth surfaces.

Nevertheless, further calculations revealed that the area of real contact is proportional to the load due to the continuous formation of new junctions with increasing load and the average size of micro junctions is

independent of the load [28].

While sliding on dry surfaces, the junctions are immediately formed between surface asperities and the frictional force is the force necessary to shear these junctions [27, 28, 43]. In case of lubricated surfaces, the effect from shearing the direct contact areas is small and the main contribution to the frictional force comes from shearing the lubricant film itself. The case when two sliding surfaces are separated by a thick lubricating film is known as hydrodynamic lubrication and the friction force greatly depends on the viscosity of the lubricant [28, 43, 44].

Generally, if the viscosity of the film and/or sliding velocity is not high enough, due to the applied pressure, the lubricating film can be squeezed out from the contact area, changing the hydrodynamic to a boundary friction regime. In the case of boundary lubrication, the frictional force is usually higher than that in the case of hydrodynamic lubrication, and the force is nearly velocity independent.

In the early days, it was assumed that when two surfaces slide with respect to each other, the friction between them increases because of the surface roughness (a traditional explanation of solid friction, mainly used in engineering sciences), meaning that asperities of opposing surfaces interlock during sliding. Later on the mechanism of adhesion (intermolecular forces between contacting surfaces) was proposed as the main source of sliding friction. In 1940, a model describing the connection between adhesive and friction forces was developed by Bowden and Tabor. According to the model, when two surfaces are brought into contact, contacting asperities experience elastic and plastic deformation. At these small contact areas, atoms come very close to each other, generating attractive and repulsive interatomic forces. If the shear stress developed over the contact regions while applying a tangential sliding force is low, then the interatomic forces keep atoms from sliding over each other. However, if the shear stress reaches some critical value, so-called shear strength s, the force between atoms can be overcome and therefore sliding occurs. Then this adhesive force over the total real contact area is given by:

$$F_{adh} = A_r s \tag{2.3}$$

In case of elastic deformation, the real area of contact which is proportional to applied load can be expressed as:

$$A_r \simeq 3 \left(\frac{R}{\sigma}\right)^{1/2} \frac{L}{E_c} \tag{2.4}$$

where R is the average radius of curvature of contacting asperities, σ the standard deviation of their heights, L the normal load applied and E_c the elastic modulus.

Now in case of plastic deformation:

$$A_r \simeq \frac{L}{H} \tag{2.5}$$

and,

$$\mu_{adh} = \frac{s}{H} \tag{2.6}$$

where H is the material hardness.

As can be deduced from above formulation, in both cases the real area of contact depends linearly on the applied load.

Historically, the notion that friction is strongly related to adhesion - a bonding mechanism between atoms that makes it difficult to slide surfaces over each other - goes back to studies of Desaguliers in 1734. When considering how friction originates at the atomic level, it is appropriate to discuss several models that have been developed over the years in order to explain the mechanism of friction at small scales [28, 44–48].

2.1 Frenkel-Kontorova model

The simple model for studying friction at the atomic scale was proposed by Frenkel and Kontorova in 1939, known as the Frenkel-Kontorova or simply the FK model [49–51]. In this model the surface is presented as a one dimensional chain of atoms, interacting through harmonic potential with each other, in the presence of an external periodic potential (corresponding substrate potential).

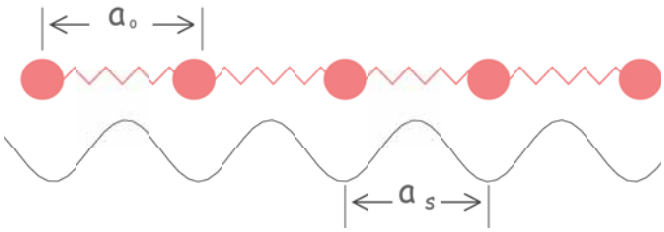

Figure 2.4. Schematic presentation of the Frenkel-Kontorova model: A chain of atoms placed in a periodic potential.

The spring potential between the atoms in the chain represents the interatomic interactions of the sliding material. If the number of atoms and

the number of potential minima are equal, then the equilibrium configuration is reached when each atom lies in the bottom of each minima. In order to slide the chain over the potential surface, one has to apply force large enough to overcome the potential barrier. Once the force is sufficient (force necessary to initiate sliding), atoms reach the potential barrier peak and slide into the next minima. The maximum lateral force, which is necessary to slide the chain, is reached when the density of atoms equals the substrate potential minima. However, the frictionless sliding is expected for incommensurate systems. The prediction of ultra-low friction is the most exciting aspect of the FK model.

However, the model has some limitations, namely it assumes that the chain atoms are moving only in one direction, also the chain potential consists only of the interactions between the nearest neighbors. The model also neglects the interactions of the interfacial layer (represented by the chain) with the rest of the slider body.

2.2 Tomlinson model

An even earlier one-dimensional model for studying friction was proposed by Tomlinson in 1929 [31,52]. The model consists of atoms that are sliding over a periodic potential while they are individually connected to a slider by harmonic springs.

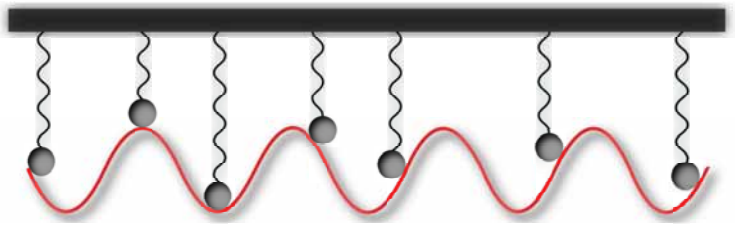

Figure 2.5. Schematic presentation of the Tomlinson model.

In the frame of this model, each atom is dragged by a spring that is moving with a constant velocity. Once the force is applied to the slider, initially, the elastic energy builds up in the spring which is converted into a kinetic energy (atom overcomes the potential barrier) and dissipated as a heat (sliding into the next energy minimum).

"*As the two bodies move relatively, there is a continuous change taking*

place in the pairs of molecules bearing the load, and the theory assumes that when two molecules come into contact, i.e., come into each other's repulsion field, and then separate, a loss of energy occurs which is manifest as friction - Tomlinson".

The interaction potential between each atom with the substrate has a sinusoidal form for an ideally ordered crystalline surface with lattice constant a. The total potential energy is composed of two terms: the interaction between the atom with the substrate potential and its interaction with the slider:

$$V(x,\,t) = -\frac{U}{2}\,\cos\left(\frac{2\,\pi\,x}{a}\right) + \frac{1}{2}\,k\,(v\,t - x)^2 \tag{2.7}$$

where U is the amplitude, x the atom displacement, k the elastic constant of the spring, v velocity of the slider and t time. The dynamics of the atom in the Tomlinson model is governed by the following equation:

$$m\,\frac{d^2x}{dt^2} + m\,\mu\,\frac{dx}{dt} = -\frac{\partial V(x,\,t)}{\partial x} + \xi\,(t) \tag{2.8}$$

where m is the mass of the atom, μ the damping coefficient and $\xi\,(t)$ the thermal activation force.

While the Tomlinson model for friction has been widely used for many systems, it fails in description of interactions between the slider surface atoms.

In recent years, molecular dynamic (MD) simulations have been applied to three dimensional systems to study friction at the atomic scale and its dependence on the atomic structure of the sliding materials and interatomic interactions.

2.3 Friction at the small scale

A nanometer is roughly ten times the size of an individual atom, therefore nanotribology is the study of friction/wear at atomic length and time scales. The main feature by which nanotribology differs from tribology is the involvement of atomic forces in the determination of the final behavior of the system. Significant efforts to determine the nanoscale origins of the tribology phenomenon has been made in the 20th century, facilitated by the development of new experimental and theoretical techniques for characterizing materials at that scale [46, 49].

The study of the microscopic origins of friction becomes difficult due to the nature of the contact. Generally, contact between sliding materials occurs at the apexes of small asperities which are sandwiched between two solids, and therefore it is inaccessible without application of proper techniques. The atomic and friction force microscopies (AFM/FFM), the surface force apparatus (SFA) and the quartz-crystal microbalance (QCM), have become principle tools for investigating nanoscale contacts and frictional forces.

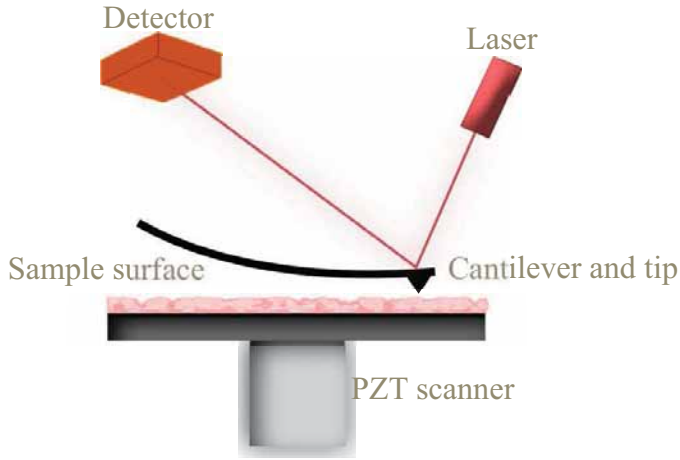

Figure 2.6. General design of the AFM instrument, most widely used for nanoscale single-asperity studies. A sharp tip with a radius between 10-100nm is brought in close proximity to the sample surface. Forces between the tip and the sample cause the cantilever deflection which leads to the laser beam deflection reflected off the back of the cantilever and collected by a detector.

In addition, the dramatic increase in computer performance in recent years has made molecular dynamics simulations applicable for directly addressing the atomistic origins of friction. Access to the new, microscopic level of investigation involves the study of the contacts themselves in terms of chemical bonding and the process of excitation and energy

dissipation [53]. The relative importance of electronic and phononic contributions is a matter of particular interest [54].

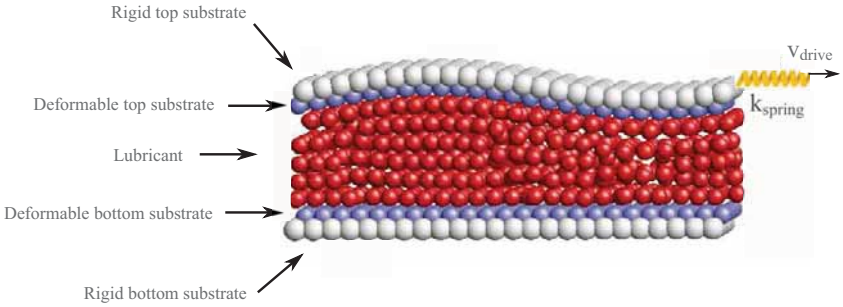

Figure 2.7. Schematics of the MD simulation of friction. The top and the bottom substrate layers are separated by a lubricant, driving force is applied only to the top rigid substrate while the bottom substrate is fixed. Adapted from ref. [49]

Studies of frictional processes show substantial differences in the behavior at the molecular level and that observed in macroscopic devices. Macroscopically, contact mechanics is mostly based on continuum elasticity theory (e.g. Hertzian Theory of Elastic Deformation that relates the circular contact area of spheres to the elastic deformation properties of the materials while neglecting any surface interactions such as near contact van der Waals or contact adhesive interactions [55]) which is poorly applicable at the microscopic level due to the discrete nature of matter that cannot be overlooked [56].

It is well known that a macroscopic contact is rough, containing a large number of smaller contacts (asperities) and the total area of these contacting asperities is much smaller than the apparent area of contact. The frictional force is proportional to this true contact area:

$$F_f = \tau \sum A_{asp} \tag{2.9}$$

where τ is the interfacial shear stress, thus representing the frictional force per interfacial atom. In order to isolate surface roughness from other parameters that influence friction, many experiments focus on single asperity (typically from tens of nanometers to micrometers in size) studies. These measurements have been very successful due to the possibility that deformation of an asperity can be described in the framework of continuum mechanics theories. As predicted by the Hertz theory, the contact area is not linearly proportional to the load, but rather varies with $L^{2/3}$, which is in contrast to macroscopic observations. However, deviations from single asperity theories have also been observed in experiments at these small scales due to the large sensitivity of contact behavior to spe-

cific experimental conditions such as surface chemistry or tip geometry. Even though these issues can be eliminated in molecular dynamics simulations, results regarding friction laws are still contradictory. For instance, based on the studies of Wenning and Müser [57] for commensurate interfaces $F_f \sim L$, while for incommensurate non-adhesive contacts $F_f \sim L^{2/3}$, which disagrees with the later simulations by Gao [58], who found that $F_f \sim L$. According to Wenning and Müser, friction is not defined by the contact area itself. Rather, the friction experienced by an individual atom at the interface is caused by the local normal stress which is influenced by the atomic structure of the interface, thus giving a distinct power law dependence for each atomic arrangement.

Later on, molecular dynamics simulations of SFM experiments of an amorphous carbon tip sliding on a diamond surface under a normal load and with a presence of adhesion at the interface demonstrated that single-asperity theories break down at the nanoscale [59]. According to the results $A_{asp} \sim L^{0.7}$ and $F_f \sim L$, resulting in $F_f \neq \tau A_{asp}$. According to the authors, the breakdown of single-asperity theories of friction is due to the fact that at these length scales the real contact area (the sum of contact areas per atom (see Fig. 2.8) is different from A_{asp} and the friction laws should be defined in terms of A_{real}. They demonstrate that a single nanoscale contact still consists of smaller atomic size contacts and therefore its behavior can be described via macroscopic theories of roughness.

Atomic scale wear is another topic of interest as it changes the landscape of the interface and therefore affects friction [60]. Many tribology experiments and simulations have reported a wearless friction regime at the atomic scale. However, few studies have been dedicated to the atomic origins of wear. Large enough adhesive forces at the sliding interface can be responsible for rupture within the body of material instead of the interface which leads to a change of the material surface. Such transfer has been seen in MD simulations of Si/Si [61] interfaces and of Cu/Cu [62] contacts. The transfer phenomena can have a dramatic effect on friction, either reducing or increasing it. Atomic scale wear was also found in experiments performed by Gnecco with a Si SFM tip, in UHV, scanning the KBr (001) surface [63]. It was observed in the experiment that sliding, accompanied with removal and rearrangement of ion pairs, caused continuous increase of the lateral force due to formation of regular terraces with the same periodicity and orientation as the substrate. Generally, if wear is due to material transfer, then the mechanisms and the amount

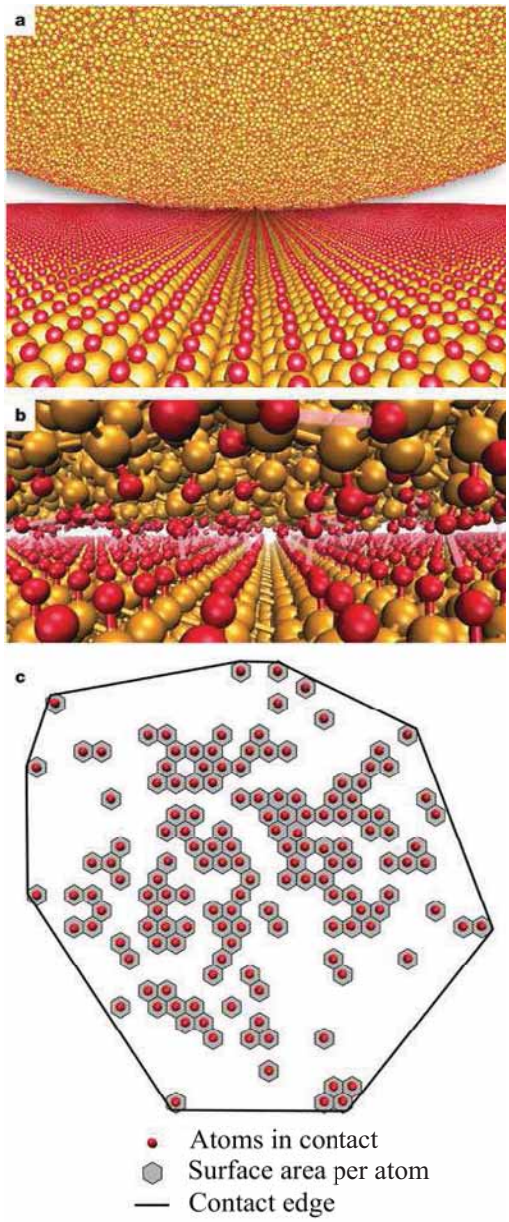

Figure 2.8. Contact between an amorphous carbon tip and a diamond sample. (a) Far view showing contact geometry. (b) Close view. (c) Contact area definition. Contact area per atom is represented by gray hexagons. Real contact area is the sum of the areas of the hexagons. The contact area of an asperity is enclosed by the edge (solid line) of the contact zone. Adapted from ref. [59]

of transferred material will depend on the relative humidity, applied load and the chemistry (bonding strength at the interface and in the bulk) of the material itself. The possible mechanisms that commence wear have been summarized as follows: formation and propagation of voids, fracture,

and nucleation and motion of dislocations. The primary process initiating wear was suggested to be the formation of voids under the indenter, which grow together to cracks providing nucleation sites for dislocations [56]. The MD technique has been a primary tool for investigating the atomic scale friction and wear process. When the size of a single contacting asperity reaches nanometers, the process governing friction and wear cannot be fully understood without atomistic simulations.

Atomistic simulations are quite useful for understanding not only single-asperity contacts, but nanotribology in general. Through their ability to follow the motion of each individual atom, simulations have determined the atomic origins of many experimental results. However, molecular modeling of any tribological system has its challenges [49]. The major issue which deserves particular focus is the availability of accurate interatomic potentials (force fields) to describe the interactions between all the atomic sites in the system. The force acting on an atom is defined as a negative gradient of the total energy of the system, which is a function of all atomic coordinates. Unfortunately, an accurate description of the total energy involves the quantum mechanics of electrons that raises complications for big (typically containing more than hundreds of atoms) systems. Therefore, most of the tribological MD simulations are carried out with empirical force fields which must be chosen carefully as each force field is developed to fit a given set of experimental data. However, in real tribological situations involving wear, atoms are essentially changing their coordination, chemistry and sometimes charge which requires a potential capable of describing chemical reactions and process of interface wear.

Another great challenge of investigating frictional behavior of a system through MD simulations is description of energy dissipation during sliding. The kinetic friction involves energy generation at the sliding interface which must be transferred through the bulk, converted to the internal degrees of freedom and the heat produced has to be removed from the system. In MD simulations, the excitations generated at the sliding interface travel through the system and are reflected back by the cell boundaries. In order to avoid overheating of the system the heat must be removed. A solution to this problem is to modify the equations of motion inside the simulation cell. A standard approach in such situations is the introduction of a thermostat (such as velocity rescaling, Nose-Hoover or using Langevin equations of motion [64–66]). On the other hand, using such unrealistic damping dynamics may lead to unphysical motion of

atoms in the system. Therefore, a dissipation scheme where the motion of all the atoms near the sliding interface are described via Newtons equation and the boundary atoms are treated as Langevin atoms (experiencing friction and random forces) has been widely applied. A realistic way to minimize accumulation of the heat during non-equilibrium MD simulations has been proposed by Benassi, through implementation of the non-Markovian Langevin terms in the equations of motion of the dissipative boundary layer [67].

Despite some complications that arise while studying tribological systems via MD simulations, it can explore some extreme frictional situations. For instance, MD simulations can be used for studying the flash temperature regimes caused by local heating through a wear process where surface melting takes place. Such regimes cannot be explored experimentally by AFM, since the surface melted layer wets the tip before the contact. Besides the ability of accessing high temperatures, the MD simulations are useful for high speed nanofriction studies. While the AFM experiments operate with lower speeds than 1 m/s, molecular dynamics studies of gold clusters sliding over graphite surfaces demonstrated a new ballistic nanofriction regime [68] at higher speeds than 10 m/s where the temperature dependence on sliding friction is opposite from that found in case of low speed drift sliding.

Generally, MD simulations are able to more directly correlate microscopic interactions to sliding behavior, but they are still unable to cover length and time scales of macroscopic experiments.

In the end, MD simulations as well as experimental techniques have their challenges and each of the approach is related to a different aspect of the problem. Ultimately, more simulations and experiments need to be performed in order to bridge nanotribology to macroscopic behavior.

3. Ice

Ice or snow covers a small, but significant part of the Earth's surface, both land and sea, and plays an important role in our atmosphere. Ice is not a static medium, but a dynamical one showing strong variations of its characteristics with time and place, as can also be experienced by any human. A better understanding of the structures and properties of ice (most of its properties have been interpreted in terms of its crystal structure) is therefore a topic of current research in physics.

However, compared to liquid water, ice is fairly well understood. Throughout the last century, properties of ice such as crystal structure, the forces between its constituent molecules etc., have been experimentally analyzed by ellipsometry, X-ray scattering, proton channeling, nuclear magnetic resonance (NMR), scanning tunneling microscopy (STM) and atomic force microscopy (AFM).

The ordinary ice known from every day life is in the so-called ice Ih phase (there exist a number of other ice phases for lower temperatures and higher pressures) and this work has been mainly dedicated to the investigation of the surface properties of ice Ih as it has been a matter of great importance in physics, chemistry and many technical applications.

3.1 Water

Water is necessary both for the evolution of life and its continuation. It possesses particular properties that cannot be found in other materials and that are required for life-giving processes. Besides the fact that water covers two-thirds of the planet's surface and controls its climate, its extremely simple chemical formula shows numerous unusual (anomalous) properties. It has been stated that life depends on these anomalous properties. The large heat capacity, high thermal conductivity and high wa-

ter content in organisms contribute to thermal regulation and prevent local temperature fluctuations. The large heat capacity of water allows oceans and seas to act as heat reservoirs so that sea temperatures vary only a third as much as land temperatures, therefore moderating climate. Hence the study of the properties of water has been a fundamental scientific challenge for many years [69–71].

The water molecule is the smallest molecule containing more than one atom. The experiments of Cavendish and Lavoisier in the 1780's, established that a water molecule is composed of the elements hydrogen and oxygen. Later on, it was found that 11 per cent of the weight of liquid water is hydrogen and 89 per cent is oxygen.

Molecular dimensions such as, the bond angle and the bond lengths of the molecule are known with remarkable accuracy. The arrangement of the nuclei in a molecule forms a triangle with an H-O-H angle of $104.5°$ and 0.957 Åbond length.

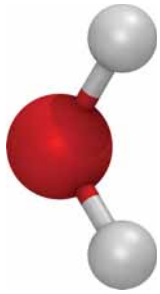

Figure 3.1. Schematic representation of a water molecule.

These values are obtained for a vibrationless and rotationless water molecule, in other words for the equilibrium state of the molecule when even zero-point vibrational energy (a residual vibrational energy possessed by a molecule) is excluded [69].

The molecule consists of 10 electrons, eight from the oxygen atom and one from each of the hydrogen atoms. Of these ten electrons, two occupy the $1s$ state and remaining eight fill $2s$ and $2p$ states. Each hydrogen atom shares an electron pair with the p orbital of the oxygen atom. This results in complete occupation of the first shell of the hydrogen atom and the second shell of the oxygen atom. Therefore, atoms in the water molecule are considered to be covalently bonded.

The fact that the oxygen atom is more electronegative than the hydrogen results in the arising of electrostatic forces of attraction between hydrogen and oxygen atoms. Two of the four outer orbitals of oxygen atom are

directed towards two hydrogens and other two orbitals are on the opposite side from the hydrogen nuclei, these orbitals are called the lone-pair orbitals. Therefore, the configuration of these four orbitals have a tetrahedral shape.

The bond that arises when a hydrogen atom interacts with oxygens in another molecule is called a hydrogen bond. This is considerably weaker than covalent bond and considerably strong relative to the natural thermal energy. When two water molecules form a hydrogen bond O-H–O, the hydrogen nuclei stay covalently bonded to one of the oxygen atoms and the H–O distance is much larger than the length of the covalent bond. In other words, a hydrogen bond in a water molecule is the attractive interaction between hydrogen and oxygen atoms. In a hydrogen bond, a hydrogen atom is called bond donor while a negative oxygen atom in called a hydrogen bond acceptor. It is also possible that a hydrogen atom forms two bonds rather than one, in this case the bond is called a bifurcated hydrogen bond.

The consequences of the deviation of the hydrogen bond strength in water from its natural value appears to be essential. The behavior of water changes dramatically upon strengthening (water would behave similar to a glass) or weakening (water would be a gas, existing as a liquid only at sub-zero temperatures) of the hydrogen bond [72]. The bond strength strongly varies with the hydrogen bond length and angle, which can be affected by polarization shifts in different hydrogen-bonded environments also with binding of a water molecule to ions. Further investigations revealed that the hydrogen bond strength becomes almost linearly dependent on the bond length (shorter length gives rise to stronger bonding) if the H-O-H angle reaches 180 °. The hydrogen bond strength also depends on temperature and pressure, as it has been reported by Doughety in 1998 [72], due to the fact that the bond length increases with temperature increase and decreases with pressure increase.

An important feature of the hydrogen bond is that it possesses direction and accommodation of these directions creates an expanded arrangement of water molecules. Such a change in structure takes place at low temperatures and leads to a stronger binding of water molecules.

Water is not simply a liquid with hydrogen bonds between its molecules, rather it is a substance with these bonds forming a three-dimensional network. It has been often stated that the hydrogen binding is responsible for some of the unusual properties of water. Its unusual high viscosity, high

melting and boiling temperatures, negative slope of the melting curve, density maximum of a liquid water slightly above the freezing point, generally the fact that many properties, such as volume, heat capacity, compressibility, viscosity, diffusion coefficient, depend non-monotonically on temperature and pressure and many others are considered to be anomalous.

It must be mentioned that some of its anomalies are not unique for water, for instance the negative slope of the melting curve, which is a consequence of the fact that the volume of water increases during freezing, also characterizes Si and Ge showing low-density structures in the solid state [73]. However, the set of unusual properties of water is exceptionally large for one substance.

3.2 Bulk ice

The tendency of the hydrogen bond to form an open tetrahedral network at low temperatures is responsible for the configuration of solid water [74–76]. Some scientists believe that there is a three dimensional network in water perturbed by thermal motion [73]. Molecules fall into cavities, at high enough temperatures, of the network which results in higher density of water compared to ice. Others reported that water is a mixture of distorted ices Ih and III [73].

Statistical physics shows that the probability to meet any particular configuration in the ensemble is proportional to the Boltzmann factor $e^{-\frac{E}{kT}}$. The fact that energies E of all ice configurations are very close, leads us to assume that water can contain any number of ice configurations, but water structure does not exhibit long-range order [73].

The solid phase of water is a three dimensional network of water molecules that form hydrogen bonds between each other. Molecules are packed with fourfold coordination, which leads to a diamond structure of the ice crystal. While in liquid water, each molecule is hydrogen bonded to approximately 3.4 other molecules.

Hexagonal ice (known as ice Ih) has a very open, tetrahedrally coordinated lattice structure, with $O-O$ distances of 2.76 Å and $O-O-O$ angle of 109 degrees. The open crystalline structure of ice causes its low density (0.931 g/cm^3) compared to a liquid water (1.00 g/cm^3), explaining the fact of ice floating on water. Amongst a number of well known crystallographic structures of ice, the hexagonal configuration (ice Ih) is most prevalent in

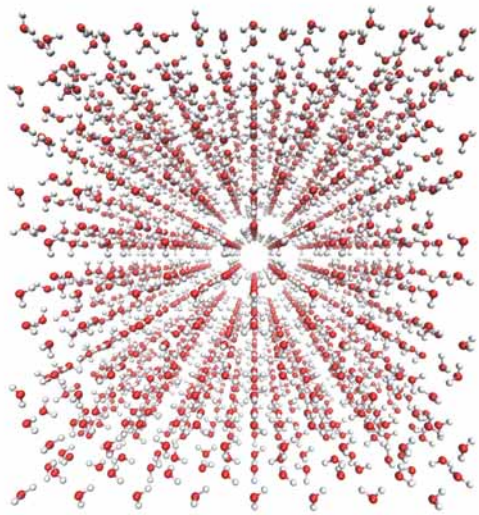

Figure 3.2. Crystalline structure of ice Ih.

nature. There exists a statistical model for the structure of ice based on the following assumptions:

- Each oxygen atom has two hydrogen atoms attached to it, at distances of about 0.95 Å, thereby forming a water molecule.

- Each water molecule is oriented so that its two hydrogen atoms are directed approximately towards two of the four oxygen atoms which surround it tetrahedrally.

- The orientations of adjacent water molecules are such that only one hydrogen atom lies between each pair of oxygen atoms.

- Under ordinary conditions, ice Ih can exist in any one of a large number of configurations, each corresponding to a certain distribution of the hydrogen atoms with respect to the oxygen atoms.

The above formulation is known as the Bernal-Flower rules [77]. Based on these rules, in ice Ih, each oxygen atom is surrounded by four nearest neighbors and involved in hexagonal rings. However, it is well known that

bulk ice is orientationally disordered, meaning that there are a number of proton configurations which meet hydrogen bonding rules. In 1935, Pauling suggested that all possible arrangements that satisfy the ice rules are equally probable and by estimating the number of configurations in two different ways calculated a residual entropy [78].

If we consider a system of crystalline ice with N number of molecules per mole and W_N number of accessible configurations, the residual entropy is given by:

$$S_0 = k \, \ln (W_N) \tag{3.1}$$

where k is the Boltzmann factor. A molecule can be found in six different orientations in a tetrahedral structure satisfying ice rule 2. However, the chance that adjacent molecules allow location of both hydrogen atoms of the original molecule according to the given orientation is 1/4, therefore the total number of accessible configurations is:

$$W_1 = (6/4)^N = (3/2)^N \tag{3.2}$$

Now only fulfilling the ice rule stating that one hydrogen atom lies between two oxygens, gives $2^{2\,N}$ ($2\,N$ is the number of bonds) number of possible arrangements. In addition, there are sixteen possible arrangements of the four hydrogen atoms surrounding any given oxygen atom, ten of which lead to generation of $(H_4O)^{++}$; $(H_3O)^{+}$; $(O\,H)^{-}$ or O^{--}, leaving only 6/16 = 3/8 number of the possible hydrogen configurations. Consequently the same result is obtained for the total number of configurations:

$$W_2 = 2^{2\,N} \, (3/8)^N = (3/2)^N \tag{3.3}$$

and the calculated residual molar entropy equals:

$$S^{Pauling} = R \cdot \ln(\frac{3}{2}) = 0.80574 \ldots J\,K^{-1}\,mol^{-1} \tag{3.4}$$

where R is the universal constant. This result is in good agreement with experimental value. It is believed that disordered arrangement of hydrogen atoms gives ice its high dielectric constant and additional stability to the solid phase.

Studies of the electrical polarization of ice when an electric field is applied led N. Bjerrum (1952) to specify crystallographic defects, known as

Bjerrum defects (L and D defects). Formation of the L or D orientational defects involves violation of one of the ice rules.

Assuming that there are two or zero hydrogen atoms per bond gives us a D or L defect. All this results in non-zero entropy of ice [79].

After Bjerrum, many scientists studied the defect formation and their arrangement in the ice crystal. In 1999, R. Podeszwa and V. Buch suggested that formation of L and D defects is confined by electrostatic repulsive forces that arise between two positively charged hydrogen atoms in D defect and two electronegative oxygen atoms in L defect [80]. They carried out molecular dynamic simulations of large enough ice structures and found out that initially introduced idealized Bjerrum defects migrate with a low migration barrier. The figure below shows a molecular dynamic study of a jump of defects in an ice lattice. The drift is not random but rather presenting preferred migration paths.

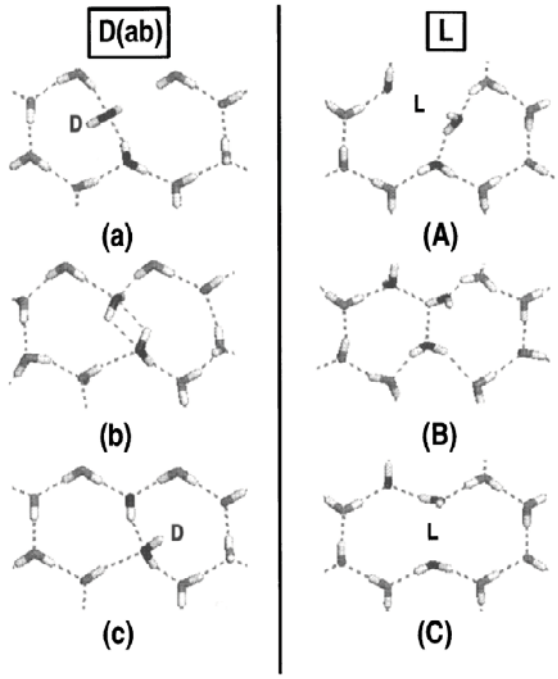

Figure 3.3. A jump of D and L defect in ice crystal at 230 K. Adapted from ref. [80].

Based on their studies, the number of possible defect arrangements is actually quite large. As we have mentioned before, solid water is polymorphic. Each crystalline modification obeys ice rules and involves molecules forming hydrogen bonds with the surrounding four neighbors. Most of the ice modifications, except hexagonal ice, exist under high pressure or at very low temperatures. Polymorphism is not unique for ice, there are

several different crystalline modifications of Si and Ge known, but unlike ice, the transition from one to another crystalline phase involves the change of intermolecular forces and causes transitions from semiconductors to metals [73]. The transformation of ice from one phase to another causes changes in crystal structure, density, symmetry and dielectric constant. Most of the high pressure modifications are metastable at ambient pressure and low temperatures.

When ice Ih is subjected to a pressure around 2.20 kbar at temperatures between -30 and -50 $^{\circ}\mathrm{C}$ ice III is formed, which is denser than ice Ih because of reduced volume and occupies the smallest ($p,\ T$) region on the ice phase diagram. At temperatures below $-70^{\circ}\mathrm{C}$ ice Ih transforms into ice II.

Discoveries of ice II and ice III were made by Tammann in 1900. Investigations of high pressure ice modifications were carried out later by Bridgman at higher pressures than 2.20 kbar. According to his findings, at pressures 3.7 kbar ice V is formed, which remains stable roughly between 210 and 270 K. A further increase of pressure (6.3 kbar) results in the formation of ice VI [81].

Investigations were continued and so far 16 different crystalline phases are known. It is also important to mention that all modifications contain H_2O molecules, except ice X, which is an ionic crystal. In ice X, the distance between oxygen atoms is shorter than that of all the other configurations mentioned before and protons are equidistant from the oxygen atoms. Protons in ice X rapidly swap, thus creating short lifetime ions, $OH^-$and H_3O^+. In addition the crystalline structure of ice X looks identical from all three directions.

It was known long ago that not only liquid water has a density maximum, but the density of ice Ih reaches its maximum at 80 K at ambient pressure, which is again not unique for solid water, but characterizes also Ge, ZnS etc. Accordingly, not only hydrogen bonds are responsible for anomalies of solid water but also their arrangement inside the crystal.

Amongst the many remarkable properties of solid water is one known as the premelting of ice - the existence of a liquid water at the surface of ice at temperatures well below melting point. Premelting was suggested first by Faraday as an alternative explanation for the unusually low friction of ice and has received considerable attention in recent years.

3.3 Ice surface

The slipperiness of snow and ice has been the basis for some of the oldest forms of transportation and has also found an important place in the field of winter sports. Nevertheless, its unusual slipperiness sometimes present difficulties to automobile or foot travel. These concerns have motivated scientific studies of snow and ice for many years and still the field is not completely understood. The slipperiness of ice has prompted the common speculation that lubrication is supplied by a water film. Since then, understanding of the origin of such a lubrication and generally, studies of the surface structural properties of ice has been a subject of systematic experiments. Some of the experimental findings are reviewed in the following sections.

3.3.1 Surface melting of a material

The theory of the stable existence of liquid at the surface of a solid material below its normal transition temperature implies lowering of the free energy due to melting. Various mechanisms explaining the surface melting (also known as surface premelting), as well as the experimental proof on many classes of solids such as metals, semiconductors, rare gas crystals etc., have been provided.

The first experimental evidence of surface premelting was seen in ion backscattering experiments of lead (100) carried out by Frenken and van der Veen in 1985 [82].

The surface premelting of Al (110) was observed by W. Theis and K. Horn (1994). Core-level photoemission was applied to study the density and long-range order of Al in order to distinguish a liquid-like layer from the crystalline bulk. The surface disorder was found to start at 150 K below the melting point and the logarithmic increase of its thickness with temperature was established [83].

In 1987, anisotropy of the surface melting was detected in a single crystal of Pb, exposed with different faces [84]. Later on, similar behavior was found in computer simulations of copper. According to the results, the (110) face disorders first followed by the (111) face while the (100) face does not show premelting at all [85]. Generally, the anisotropy of surface melting is strongly related to the order and packing density of different faces of a crystal.

Other experimental techniques have been applied for direct surface mea-

surements, such as X-ray [86], low-energy electron diffraction [87], neutron diffraction [88], and He atom scattering methods [89]. Along with the experiments, computer simulations have also provided the evidence for the existence of the structural disorder at a solid surface [85, 90–92], beginning from the surface/vapor interface due to the weaker binding and anharmonicity of the outermost atoms and its stable existence. This very thin liquid film is often called 'liquid-like' due to the crystalline ordering of the bulk affecting its dynamic and thermodynamic properties namely, lowering its mobility and causing a decrease in entropy, and it remains as an intermediate between the bulk solid and liquid phases.

3.3.2 Premelting of ice

One of the many remarkable properties of ice is its low friction coefficient. It is generally accepted that ice is slippery because of a liquid layer that covers its surface, but the mechanism of formation of such a lubricating layer has been a matter of systematic study since the 19th century [1, 3].

In attempts to understand the unusual slipperiness of ice, Michael Faraday (1850) proposed a theory of surface premelting, the spontaneous formation of a liquid layer at the surface of ice well below its melting temperature [1, 3, 4]. However, the theory soon became controversial - an alternative approach was proposed by James Thomson (1857) who formulated the linear dependence between the freezing point depression and applied pressure, and suggested a mechanism of pressure melting as an explanation for liquid layer formation [4]. For many years pressure melting was considered to be the main reason responsible for the low friction coefficient of ice, but later calculations (Bowden and Hughes, 1939 [11]) revealed that in standard sliding scenarios, the pressure effect is not sufficient to cause surface melting and the biggest contribution comes from frictional heating.

However, neither pressure melting (at very low temperatures) nor frictional heating explains why ice can be slippery when one is standing motionless on it. Therefore, a number of experimental techniques, such as atomic force microscopy (AFM), nuclear magnetic resonance (NMR), X-ray diffraction, and photoelectron spectroscopy, have been used to study the structural properties of the surface of ice [82, 93–100]. Most of the experiments provided evidence for the existence of structural disorder at the surface at temperatures below the bulk melting point. The fact that the

periodic crystal structure terminates at the surface results in relatively weaker bonding and therefore higher mobility of the surface molecules at temperatures as low as 200 K, consequently the surface molecules show a more disordered arrangement. However, the temperature range in which the premelted layer is seen in experiments, as well as its thickness, varies over the techniques applied, as each of them measures different physical properties of the system.

Experiments focused on using AFM to measure the thickness of the liquid film, by studying the "jump-in" distance of the tip, induced by capillary forces, revealed that the temperature dependence on the layer thickness can be described with $d \propto -\log \triangle T$, where $\triangle T$ is the difference between the melting temperature and the actual temperature [95].

In typical force experiments, the sample is moved toward the tip and the interaction forces between the tip and surface cause a deflection of the cantilever which is then used for force calculations. While approaching the ice surface, at a certain distance the tip jumps through a layer which is identified with the liquid-like layer and the jump-in distance is assumed to be its thickness. However, the van der Waals attraction may cause a jump-in before the tip touches the surface, which is the case if the gradient of the attraction exceeds the spring constant of the cantilever. The second unfavorable situation rises from the vapor condensation possibility, which may take place between the tip and the ice surface causing local increase of the premelted layer thickness. Therefore, determination of the exact thickness of the liquid layer includes few corrections that have to be done in order to avoid possible artifacts.

The model developed for the liquid layer thickness calculations is based on division of the ice-vapor interface into the ice-liquid and liquid-vapor interfaces. The importance of this model lies in its ability of describing the temperature dependence of the layer thickness that contains information about the intermolecular forces causing its formation.

The combination of the interface energy of the ice-liquid γ_{SL} and liquid-vapor γ_{LV} interfaces, along with the term containing the liquid layer thickness $\triangle\gamma$, gives the total surface energy γ of the system. The equilibrium thickness of the liquid-like layer is then derived from the Gibbs free energy as follows [95]:

$$q_m \frac{\triangle T}{T_m} = -\frac{\triangle\gamma}{\rho_L} \frac{\partial f}{\partial d} \tag{3.5}$$

where q_m is the latent heat of fusion, $\triangle T$ is the difference between the

melting T_m and actual T temperatures, ρ_L is the density of the liquid and d is the liquid layer thickness.

For van der Waals forces acting at the interface, with σ interatomic distance, $f(d) = d^2/\left(d^2 - d\sigma^2\right)$, and the thickness can be expressed as:

$$d = \left(-\frac{2\,\sigma^2\,\triangle\gamma\,T_m}{\rho_L\,q_m\,\triangle T}\right)^{1/3} \tag{3.6}$$

and for an exponentially decaying force $f(d) = 1 - \exp(-d/\lambda)$:

$$d = \lambda \ln\left(-\frac{\triangle\gamma}{\rho_L\,q_m\,\lambda}\,\frac{T_m}{\triangle T}\right) \tag{3.7}$$

Strictly thermodynamically speaking, the model is limited due to the assumptions that have been made while developing it. Nevertheless, the logarithmic dependence of the liquid layer thickness on $\triangle T$ has been confirmed by more detailed calculations.

The orientation disorder of the surface dangling bonds, which is the direct consequence of the crystal structure termination at the surface, has been studied by sum-frequency generation (SFG) vibrational spectroscopy for the temperature range 173-271 K. According to the author's report, the disorder is first seen at around 200 K and becomes more and more detectable with the temperature increase [101, 102].

Nuclear magnetic resonance (NMR) studies provided an additional evidence for the disordered arrangement of molecules at the surface. Their results showed that the rotational frequency for the surface molecules is five orders of magnitude greater than that for the bulk molecules [97].

In addition to the experimental studies, extensive molecular dynamics (MD) simulations have been performed on the surface of ice, demonstrating the presence of a quasi-liquid layer at the surface, although it's thickness and temperature dependence is somewhat a function on the parametrization of the potential that is applied in simulations to represent the intermolecular interactions [103].

Simulations carried out with the TIP4P/Ice potential demonstrated the surface melting dependence on the crystallographic face orientation, namely the basal face showed the first indication of the surface disorder at about -100 °C [8].

Here again, we use the term 'liquid-like layer' instead of water layer. The reason is the same as in case of any other material - premelted liquid phase does not possess usual water properties. It is an intermediate phase between the solid and liquid which is caused by the proximity of the ordered crystallographic structure of ice (phenomena known as the

proximity effect). Motion of the surface molecules is limited by Coulomb interactions with the bulk, therefore exhibit more ordered structure which falls off approximately exponentially with distance, with a characteristic length typically equal to a few molecular diameters [3].

3.4 Ice friction

Generally, the amount of friction encountered during sliding strongly depends on the different physical properties of the sliding materials. One of the most important parameters affecting properties of a material, and therefore friction, is temperature. When the temperature is raised, either by setting a system of investigation near the melting point or locally at the contact region by pressure melting/frictional heating, most of the materials become soft, creating larger areas of a real contact. Since the frictional force is the result of the local adhesions at the sliding interface, increasing temperature leads to high values of the frictional force (as has been observed in case of two gold surfaces sliding relative to each other). However, the situation is reversed if the melted fluid possesses a low viscosity leading to a condition of lubricated sliding. Ice is a solid having these properties, demonstrating very low friction upon sliding.

Friction plays a critical role in both terrestrial and extraterrestrial ice mechanics [22]. Examples include fracture of the Arctic sea ice cover [104–114], brittle compressive failure during interactions between natural ice features and engineered structures [115, 116] and tectonic activity of ice-encrusted bodies within the outer solar system [117–125]. For most of these systems, it is the friction of ice sliding upon itself that dominates the mechanics and heat generated at the interface. However, the knowledge obtained from the studies of ice friction in other field applications, such as ice sports or winter transportation, where ice against different materials are investigated, can be applied to the areas mentioned above and may offer a better insight into the driving mechanism of ice friction.

Generally, the complexity of a problem increases with the number of parameters influencing it. Existing experimental data show generally low coefficients of friction (from 0.05 up to 1.6) at temperatures below the melting point, with a clear dependence on the sliding velocity, temperature and applied load.

As we have discussed before, solid surfaces are always covered with asperities. Sharing bonds (chemical and/or physical nature) that are formed

between these asperities when surfaces are brought into contact determines the amount of friction during sliding. In addition, the surface of ice also has a thin premelted layer, which increases in thickness during sliding due to the frictional heating. This water film reaches its steady-state thickness because if it becomes too thin the friction and consequently heat generation increases and if it becomes too thick the friction is reduced. The regime in which friction operates changes based on the liquid-like layer thickness, causing a change of the friction coefficient itself.

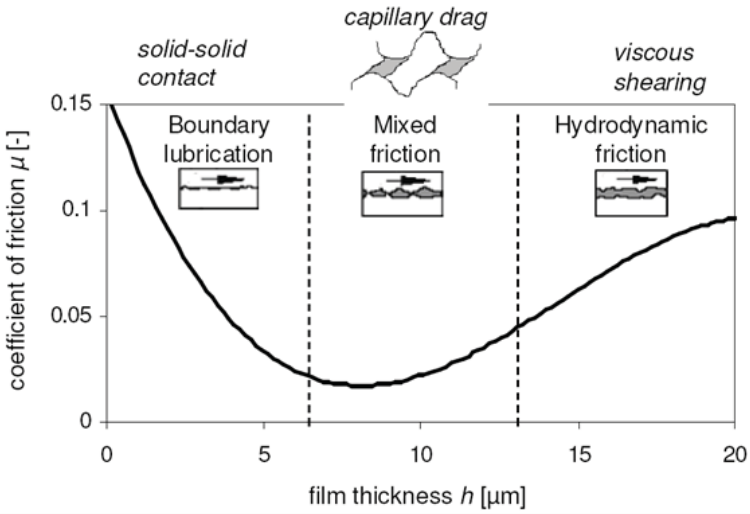

Figure 3.4. Friction coefficient as a function of the film thickness. Adapted from ref. [126]

Figure 3.4 shows the friction coefficient in different regimes characterized by the thickness of the interface liquid layer [126]. The boundary friction regime describes a case when the interface layer thickness is much smaller than surface roughness and the friction is the result of solid-solid adhesion. Once the thickness of the liquid layer increases, the friction becomes partly caused by sharing the lubricating layer itself, which is the case of the mixed friction regime [29].

Finally, in the hydrodynamic regime, the surface is completely covered by a liquid layer. Hence, there is no solid-solid contact and the main contribution to the frictional force comes from the capillary drag forces between the slider and ice surface.

Thus temperature is one of the crucial parameters in defining the friction regime that takes place during sliding. Early findings of the influence of temperature on the friction of ice originate in the experiments conducted by Bowden and Hughes in 1939, showing the reduction of the

kinetic friction (more pronounced from $0°C$ to $-40°C$) with increasing temperature, for the range of $0°C$ to $-160°C$. However, the simple supposition that the lubricating action of a water layer at the surface of ice reduces friction contradicts the experimental data. It has been established that in the case of repeated sliding on the same track, when the lubricating layer can only increase in thickness, friction does not decrease but, on the contrary, increases.

A mathematical model based on the assumption that the very low friction between ice and different materials is caused only by viscous shear of a water layer between them has been developed by Oksanen and Keinonen in 1982 [18].

Based on their assumption, the friction is formulated as follows:

$$F_\mu = \tau\, A = \eta_0 \frac{v}{d} A \tag{3.8}$$

where τ is the shear stress, A the contact area, η_0 the viscosity of water, v the velocity of the slider and d the thickness of the water layer. The frictional energy generated during a time interval b/v (b being the length of a rectangular slider, fig. 3.5) is given by:

$$Q_f = \mu\, F_N\, v \frac{b}{v} \tag{3.9}$$

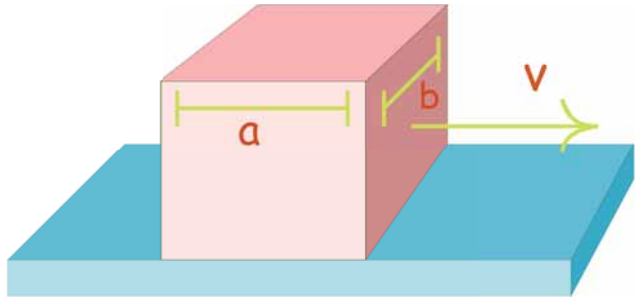

Figure 3.5. Schematic drawing of a rectangular slider moving on smooth ice with a velocity v.

The generated heat is partially conducted in to the slider and partially used for melting the ice surface. The amount of heat transferred in to ice during the same time interval b/v, can be estimated as:

$$Q_{c1} = \frac{\lambda_1\, a\, b\, \triangle T_1}{\delta} \frac{b}{v} \tag{3.10}$$

where λ_1 is the thermal conductivity of ice, $\triangle T_1$ the temperature difference between the interface and the bulk and δ the thickness of the layer

into which the heat is conducted. Equation (3.10) can be re-written in terms of the density ρ_1 and the specific heat capacity of ice c_1 as:

$$Q_{c1} = \rho_1 \, a \, b \, \delta \, c_1 \, \frac{\triangle T_1}{2} \tag{3.11}$$

The heat conducted in to the slider can be calculated similarly and then the total heat flow is obtained as:

$$Q_c = Q_{c1} + Q_{c2} = a \, b \, \left(\frac{b}{2 \, v} \right)^{1/2} \left\{ \triangle T_1 \left(\lambda_1 \, c_1 \, \rho_1 \right)^{1/2} + \triangle T_2 \left(\lambda_2 \, c_2 \, \rho_2 \right)^{1/2} \right\} \tag{3.12}$$

(where the subscript 2 corresponds to the slider). Considering the energy required for melting of ice:

$$Q_m = a \, b \, d \, h \, \rho_0 \tag{3.13}$$

where h is the latent heat of melting and ρ_0 the density of water and combining eq. (3.9), (3.12) and (3.13) one can formulate the coefficient of friction as:

$$\mu = n^{1/4} H_1^{-3/4} \, F_N^{-1/4} \frac{1}{2} \, \frac{1}{\left(2 \, v \right)^{1/2}} \left\{ \triangle T_1 \left(\lambda_1 \, c_1 \, \rho_1 \right)^{1/2} + \triangle T_2 \left(\lambda_2 \, c_2 \, \rho_2 \right)^{1/2} \right\} + n^{1/4} H_1^{-3/4} \, F_N^{-1/4} \left[\frac{1}{8 \, v} \left\{ \triangle T_1 \left(\lambda_1 \, c_1 \, \rho_1 \right)^{1/2} + \triangle T_2 \left(\lambda_2 \, c_2 \, \rho_2 \right)^{1/2} \right\}^2 + \eta_0 \, v \, h \, \rho_0 \right]^{1/2} \tag{3.14}$$

where the parameter $H_1 = F_N / A$ is the indentation hardness of ice. Considering the case when the temperature difference $\triangle T_1$ is large, the constant term in eq. (3.14) can be ignored and the friction coefficient becomes:

$$\mu = n^{1/4} H_1^{-3/4} \, F_N^{-1/4} \, \frac{1}{\left(2 \, v \right)^{1/2}} \left\{ \triangle T_1 \left(\lambda_1 \, c_1 \, \rho_1 \right)^{1/2} + \triangle T_2 \left(\lambda_2 \, c_2 \, \rho_2 \right)^{1/2} \right\} \tag{3.15}$$

so in this case the friction is determined simply by the heat conducted in to the sliding materials.

Now if the temperature differences are small then the viscous term in eq. (3.14) becomes dominant and the friction coefficient is determined as:

$$\mu = n^{1/4} H_1^{-3/4} \, F_N^{-1/4} \left(\eta_0 \, v \, h \, \rho_0 \right)^{1/2} \tag{3.16}$$

According to the model, at low temperatures, the coefficient of friction decreases linearly with $v^{1/2}$, while at higher temperatures (close to $0^{\circ}\mathrm{C}$)

it increases linearly with $v^{1/2}$. The experimental data by Oksanen and Keinonen indicate that hydrodynamic effects become dominant at around $-1°\mathrm{C}$ and the same behavior was shown by Forland and Tatinclaux for ice against steel experiments at $-1.5°\mathrm{C} \pm 1°\mathrm{C}$.

The effect of temperature studied by Evans in friction experiments carried out for 10 mm diameter rods of various materials sliding on about 120 mm diameter ice also showed a non-linear drop of the friction with temperature increase. The hydrodynamic drag component of friction that tends to increase as the temperature approaches $0°\mathrm{C}$ states the possible reason for the results.

The ice friction experiments that have been carried out with different sliding materials by various researchers are summarized in fig. 3.6 [127–131].

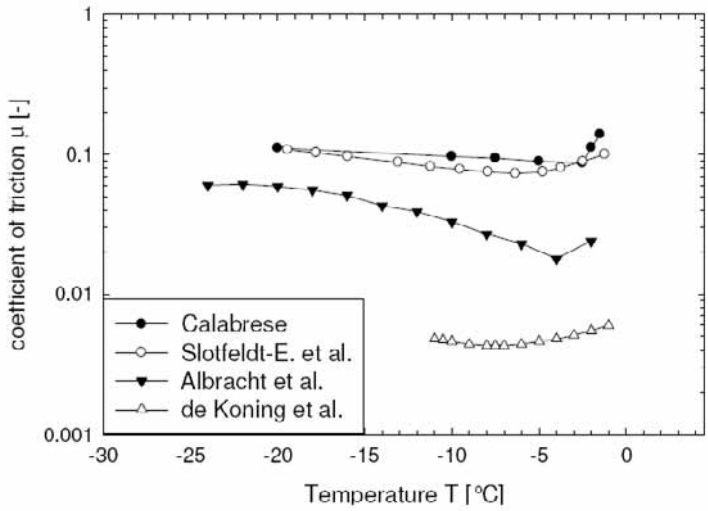

Figure 3.6. Friction coefficient as a function of temperature. Adapted from ref. [126]

At first friction drops with increasing temperature due to decreased solid-solid contact and increases again close to the melting temperature, indicating an increased contribution from the capillary drag forces. In general, measurements are very sensitive to the techniques and materials used in experiments, which explains existing differences in the reported results.

From a theoretical point of view, friction should decrease also with increasing sliding velocity because at higher velocities more frictional heat is generated, resulting in more melting and thicker lubrication at the con-

tact zone.

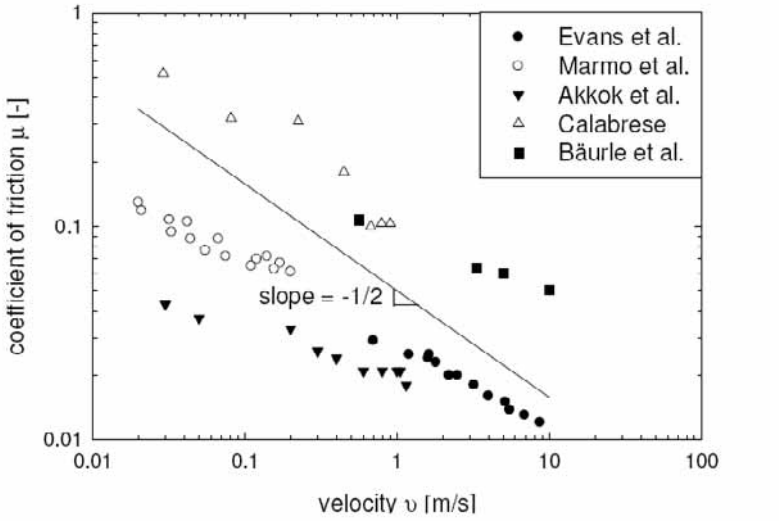

Figure 3.7. Coefficient of friction as a function of sliding velocity. Adapted from ref. [126]

The data shown in fig. 3.7 confirms the theoretical predictions in frames of boundary lubrication [14,16,127,128,131]. Here again, once the friction regime becomes hydrodynamic, the dependence changes dramatically and friction begins to increase.

As was already mentioned above, according to the mathematical model by Oksanen and Keinonen [18], the coefficient of friction is proportional to $v^{1/2}$, for temperatures close to the melting point. Other researchers have confirmed these findings and experimental results of ice against different sliding materials are illustrated in fig. 3.8.

Another important contributor to overall friction force is the applied load. The reduction in the coefficient of friction with increasing load is a well known feature of many materials and ice is not an exception [11,14,17,18].

Fig. 3.9 represents the data obtained by Oksanen and Keinonen in their ice against ice experiments, indicating that the coefficient of friction decreases with increasing normal force. Nevertheless, at higher temperatures decrease of the friction coefficient becomes less evident [126].

A numerical model for polyethylene sliding on ice including dry friction and water film generation has been proposed by Bäurle. Generally, dry friction hardly characterizes ice, nevertheless, during sliding on snow or ice, there are regions at the interface which are poorly lubricated and the friction arises from elastic and plastic deformation of the surface and

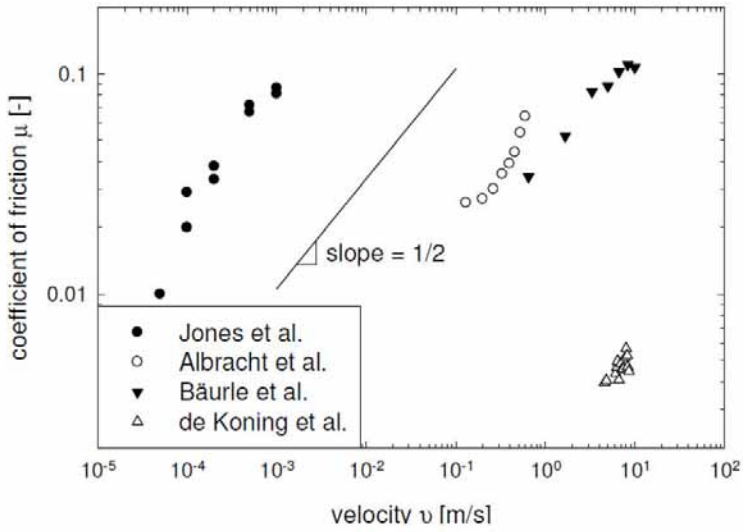

Figure 3.8. Friction coefficient as a function of sliding velocity showing contribution of drag forces. Adapted from ref. [126]

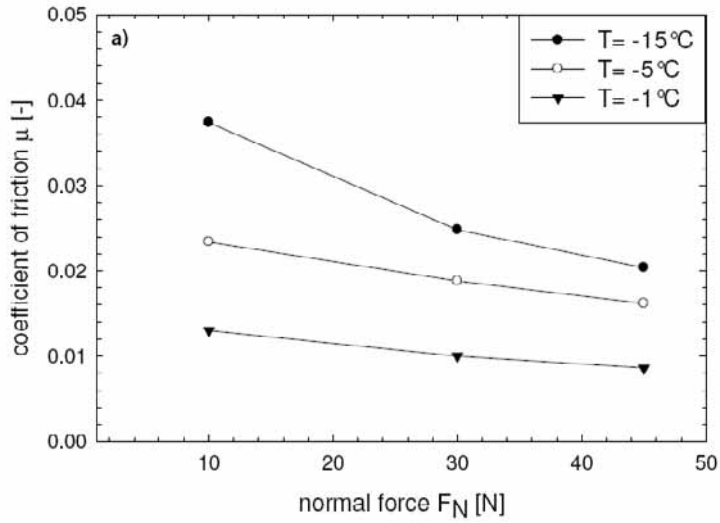

Figure 3.9. Friction coefficient dependence on applied normal force. Adapted from ref. [126]

shearing a very thin lubricating water film.

The frictional heat is generated while sliding on ice, by converting kinetic energy in to heat, which can cause local increase of the temperature

at the sliding interface (so-called flash temperature). The heat generated is partly conducted into slider and ice, depending on their thermal conductivity and partly consumed in the phase change process. Now, the dry friction can be calculated as:

$$\mu_{dry} = \frac{\eta\, v}{h_{wf}\, \sigma_0} \tag{3.17}$$

where η is the viscosity of water at $0°\mathrm{C}$, v the sliding velocity, h_{wf} the thickness of the lubricating water film and σ_0 the perpendicular stress at the contact region. In the case of dry friction, heat generation at the contact region is given by:

$$P_{dry} = \mu_{dry}\, F_N\, v \tag{3.18}$$

where F_N is the normal force. Once sliding becomes lubricated, the heat generation is then determined as:

$$P_{wet} = \eta \left(\frac{\partial v}{\partial z}\right)^2 h_{wf}\, \frac{\eta\, v^2}{h_{wf}} \tag{3.19}$$

and an energy balance determining behavior of the water layer, according to this model, is governed by:

$$\frac{\partial h_{wf}}{\partial t} = \frac{1}{L}\left(\frac{\eta\, v^2}{h_{wf}} - \lambda\, \partial_z T\, |_{z=0}\right) \tag{3.20}$$

This differential equation describes the progression of the water layer. The model was further extended, using comparisons with tribometer experiments, in order to include the dependence of the friction coefficient on normal force:

$$\frac{\partial h_{wf}}{\partial t} = \frac{1}{L}\left(\frac{\eta\, v^2}{h_{wf}} - \lambda\, \partial_z T\, |_{z=0}\right) - \frac{8\, h_{wf}^3\, \sigma_0}{3\, \eta\, D^2} \tag{3.21}$$

Here σ_0 is the perpendicular pressure and D the contact-spot diameter.

Simulations with two different loads revealed that a maximum water layer thickness is calculated for lower loads and a lower value of the friction coefficient corresponds to the higher load. While there have been extensive studies of the friction of ice at the macroscopic scale, there exists data only a few experimental investigations of ice friction at the nanoscale.

3.5 Nanoscale friction of ice

Typically, studies of the surface properties of ice at the atomic scale are motivated by the fact that a real contact between materials, sliding relative to each other, occurs at a small fraction of the apparent area. Therefore, understanding what happens at a single contact is a matter of great importance for friction analyses.

The Atomic Force Microscope (AFM) has been proven to be very effective for the atomic scale investigation of surfaces, providing the possibility of determining a single asperity contact.

The AFM has been used by Döppenschmidt to study velocity-dependent friction of ice, at a constant load of 5 n N, in the velocity range of 0.2 - 60 μ m/s. The friction force was measured by using the voltage difference between reversed and direct line scans:

$$\triangle U_{fr} = U_{fr}^{retrace} - U_{fr}^{trace} \tag{3.22}$$

where $U_{fr}^{retrace}$ and U_{fr}^{trace} are a detector output voltages due to the constant lateral deflection of the tip during scanning the surface. Experiments showed high values of friction at low velocities (at 0.2 μ m/s sliding velocity, friction was more than one order of magnitude higher than at 60 μ m/s), which can be possibly explained by the fact that at low velocities the tip penetrates more into the ice causing higher resistance during sliding.

Later on, investigations of the surface frictional properties of nanometer-thin ice islands was carried out by Bluhm, using AFM, in the temperature range from $-24°\mathrm{C}$ to $-40°\mathrm{C}$. Experiments showed that the contribution from pressure melting or frictional heating was negligible to the measured friction. The results for the friction coefficient, of value 0.6, was found to be comparable to the static friction measured in experiments at the macroscopic scale. The high friction has been explained by the fact that a liquid-like layer with 8 nm thickness, present at the surface of ice, is squeezed out due to the low scan speed (micrometers per second).

4. Methods

Molecular modeling is the science of representing molecular structures numerically and simulating their behavior by solving equations of quantum and classical physics. Very often, solving a problem in classical or quantum mechanics, electrodynamics etc., through a simple analytical approach is not possible, instead evaluation of complicated equations is necessary. However, computer performance has become very powerful in recent years, which gives us possibility of simulating complex physical problems in a reasonable time [132].

Despite the fact that nowadays the majority of simulations are conducted within the framework of classical molecular dynamics [132–134], some processes such as electron transfer, tunneling, etc. are beyond the classical limits.

Handling a molecular problem using quantum mechanics involves solving the Schrödinger equation for particles [132, 135, 136]. In a most simple case, when a single particle moves in one dimension, the Schrödinger equation is a normal differential equation. Nevertheless, considering a problem of many interacting particles moving in more than one dimension arises additional complications, since in such a case solving of the partial differential equations will be needed. Therefore, some approximations must be introduced in order to extend the utility of the method to more complex systems. The first approximation is the Born-Oppenheimer approximation that aims to discriminate electrons and nuclei, which is done by considering nuclei as a heavy and nearly motionless particles relative to electrons, so that a physical system is considered as electrons moving in a field of fixed nuclei. The potential energy surface is obtained by calculating the effective electronic energies for different nuclei coordinates and the lowest energy point on the surface is considered to be the ground state energy of the molecule.

Generally, the quantum mechanical description of the system would be preferred but, for relatively large scale simulations (systems with large number of particles) a classical mechanical approach is more common [66, 132].

4.1 Molecular dynamics simulations

Molecular dynamics (MD) is a widely used method for studying classical many-body systems (by classical we mean systems for which the motion of particles obeys laws of classical mechanics). The MD method integrates a number of equations of motion in order to predict the time evolution of a physical system [66, 137]. We start by selecting the system of interest for study and as an initial step of the MD simulation, we calculate Newton's equations for the system until its properties reach some equilibrium values. Only after the system has been equilibrated, an actual MD simulation can be performed. The algorithm takes initial atom positions, velocities and interaction potential between particles (the mathematical description of the potential energy surface) as an input. Once the time step is defined (usually 10^{-15} second or 1 femtosecond. It is expected that the efficiency of the MD simulations is maximized by using the smaller time step compared to the period of the highest vibrational frequency of the molecule.) forces between each particle pair are calculated (taking the negative gradient of the potential energy function). This is followed by updating of the positions.

There exist many integration schemes for calculating equations of motion in order to find new positions of particles and one of the most popular is the Verlet algorithm [66, 138], which takes the Taylor expansion of the coordinate of a particle at times $t + \Delta t$ and $t - \Delta t$, so that we have:

$$r\left(t+\Delta t\right)=r\left(t\right)+v\left(t\right)\,\Delta t+\frac{f\left(t\right)}{2\,m}\,\Delta t^{2}+\frac{\Delta t^{3}}{3!}\,\frac{d^{3}r}{dt^{3}}+O\left(\Delta t^{4}\right) \tag{4.1}$$

and,

$$r\left(t-\Delta t\right)=r\left(t\right)-v\left(t\right)\,\Delta t+\frac{f\left(t\right)}{2\,m}\,\Delta t^{2}-\frac{\Delta t^{3}}{3!}\,\frac{d^{3}r}{dt^{3}}+O\left(\Delta t^{4}\right) \tag{4.2}$$

where $O\left(\Delta t^{4}\right)$ is the truncation error that varies as Δt^{4}. Summing of the last two equations gives us a new position:

$$r\left(t+\Delta t\right)\approx 2\,r\left(t\right)-r\left(t-\Delta t\right)+\frac{f\left(t\right)}{m}\,\Delta t^{2} \tag{4.3}$$

The algorithm does not directly generate velocities. Knowledge of these is required for kinetic energy calculations (in order to verify correctness of the MD simulation, the conservation of the total energy needs to be tested). The velocity calculations are done as follows:

$$v\left(t\right) = \frac{r\left(t + \Delta\, t\right) - r\left(t - \Delta\, t\right)}{2\,\Delta\, t} \tag{4.4}$$

As a means to handle velocities somewhat better, the velocity Verlet scheme [66, 139] has been developed that has the benefit of having positions and velocities at the same time:

$$r\left(t + \Delta\, t\right) = r\left(t\right) + v\left(t\right)\ \Delta\, t + \frac{a\left(t\right)\ \Delta\, t^2}{2} \tag{4.5}$$

$$v\left(t + \Delta\, t/2\right) = v\left(t\right) + \frac{a\left(t\right)\ \Delta t}{2} \tag{4.6}$$

$$a\left(t + \Delta\, t\right) = -\left(1/m\right)\ \nabla V\ \left(r\left(t + \Delta\, t\right)\right) \tag{4.7}$$

$$v\left(t + \Delta\, t\right) = v\left(t + \Delta\, t/2\right) + \frac{a\left(t + \Delta\, t\right)\Delta\, t}{2} \tag{4.8}$$

The calculations are done in every pre-defined simulation time step, which is a very crucial aspect of any integration algorithm. The aim is to follow the real trajectory of the system. Therefore, if the integration time step is too large, the system will follow a trajectory that seriously deviates from the real trajectory of the system, while choosing too small a time step will result in a very long simulation.

4.1.1 Periodic boundary conditions

Since the physical systems, for which the MD simulations are usually performed, are quite small, they exhibit size related limitations. This means that the system can have many unwanted boundaries with vacuum which can lead to a unrealistic situation, unless we really want to simulate a cluster of atoms. This can be avoided by applying periodic boundary conditions (PBCs) where motion of particles is explicitly considered in the so-called supercell, while the supercell is surrounded by its infinitely replicated, periodic images [132].

Hence if, during the simulation, a particle leaves the supercell, one of its images will enter the cell from the opposite face, ensuring that the number of particles in the supercell is conserved.

It is also implied that through PBCs, each particle in the cell interacts not only with other particles in the cell, but also with their images in neighboring cells and having a short interaction range for the potential ensures that number of interacting pairs won't increase tremendously. However, sometimes applying PBCs to a system that has no periodicity (eg. gases, solids) can also cause some errors, but normally those errors are less severe than those caused by the edge effects.

4.1.2 Ensembles

The most common ensembles in statistical physics such as the microcanonical (NVE), canonical (NVT), and isothermal-isobaric (NPT), refer to a distribution of initial conditions [140, 141].

The microcanonical ensemble is used to treat the case of an isolated systems only, where the total energy (E) stays constant along with the volume (V) and number of particles (N). Hence every system in the ensemble possesses the same energy (every system has an energy which lies in the small range between E and $E + \triangle E$).

If number of accessible microstates is $W(E)$, then the probability that a system will be in any of these microstates is equal to $1/W(E)$. Then the statistical entropy is given by Boltzmann relation:

$$S = k_B \ln W(E) \tag{4.9}$$

where k_B is known as Boltzmann's constant. Using eq. (4.9), other thermodynamical quantities can be calculated for the system. Considering the thermodynamic definition of the temperature $\left(\frac{dS}{dE}\right)_{N,V} = \frac{1}{T}$, one can obtain the microscopic definition of temperature:

$$\beta = \frac{1}{k_B T} = \left(\frac{\partial \ln W}{\partial E}\right)_{N,V} \tag{4.10}$$

Most of the time, simulations are performed under the conditions of controlled temperature and/or pressure rather than total energy. The case of a system with a constant number of particles (N), volume (V) and temperature (T), is referred to as the canonical ensemble.

In real systems, keeping the temperature constant is achieved by bringing the system in contact with a larger heat bath, so that heat exchange is established caused by the collisions of the particles. In this case the probability to find a system in a microstate with energy E_i is given by:

$$p_i = \frac{e^{-\beta E_i}}{Z_N}, \qquad \beta = \frac{1}{k_B T} \tag{4.11}$$

$$Z_N = \sum_i e^{-\beta E_i} \tag{4.12}$$

where Z_N is so-called canonical partition function for a system containing N particles which defines the free energy of an NVT system as:

$$f = k_B T \, \ln Z_N \tag{4.13}$$

Another statistical ensemble which is widely used in molecular dynamics simulations is the so-called isothermal-isobaric ensemble which describes a system with a constant number of particles (N), pressure (P) and temperature (T). The system is coupled to an infinite thermal reservoir as was done for the canonical ensemble and also subjected to the action of a movable piston under the influence of an external pressure P. In this case, both the temperature of the system and its pressure will be controlled, and the energy and volume will fluctuate accordingly. The state function for the NPT ensemble is the Gibbs free energy:

$$G\left(N,\, P,\, T\right) = -k_B T \, \ln Q\left(N,\, P,\, T\right) \tag{4.14}$$

The isothermal-isobaric partition function $Q\left(N,\, P,\, T\right)$ can be expressed in terms of the canonical partition functions as follows:

$$Q\left(N,\, P,\, T\right) = \sum_\nu e^{-\beta P V} Z\left(N,\, V,\, T\right) \tag{4.15}$$

Several MD methods have been developed in the past which ensure that simulations are carried out in a correct ensemble and some relevant methods for this work will be discussed later on.

4.1.3 Intermolecular interactions

Forces between unbonded atoms and molecules are referred to as physical forces, giving rise to physical bonds. During physical binding the electron charge distributions of the molecules do not change entirely so that molecules remain distinct which is unlike the forces of chemical binding (the chemical bonds within an individual molecule) where atoms merge completely, via sharing the electrons, and form a molecular unit [142]. Besides sharing the electrons, the chemical or covalent bonding characterizes as directional - defining the orientation of a molecule and short

ranged - holding atoms tightly together and the crystalline structures which are made up by the covalent bonds cannot melt without breaking them entirely.

Usually, such specificity is missing in the definition of physical bonds, the molecules can move and rotate, but still remain bonded. One of the strongest physical forces between charged particles is estimated by the Coulomb law.

Let us consider the electric field of a charge Q_1 at a distance r:

$$E_1 = \frac{Q_1}{4\,\pi\,\varepsilon_0 \varepsilon\,r^2} \tag{4.16}$$

where ε_0 is the permittivity of vacuum and ε the dielectric constant. Then the force by which Q_1 acts on another charge Q_2 is given by the Coulomb law:

$$F_{Coulomb}\,(r) = Q_2 E_1 = \frac{Q_1 Q_2}{4\,\pi\,\varepsilon_0 \varepsilon\,r^2} \tag{4.17}$$

The electrostatic or Coulomb interaction is a strong (depending on a particular situation the strength of the interaction can become comparable, or even stronger, to that of covalent binding), long-range interaction that is significantly weakened in media of high dielectric constant [142].

Another type of interaction that arises between molecules is the so-called van der Waals (VDW) interaction. The net van der Waals force between atoms and molecules consists of the forces between rotating permanent dipoles (Keesom force), a permanent dipole and corresponding induced dipole (Debye force), and between instantaneously induced dipoles (dispersion force) [142]. The Keesom, Debye, and dispersion interaction all have the same distance dependence, each varying with the sixth power of the distance.

Molecules with a nonuniform charge distribution posses an electric dipole, which can change substantially depending on their environment and the interaction between such permanent dipoles, averaged over different orientations due to the thermal motion of the molecules, is described by the Keesom interaction, also known as the orientation interaction. Such polar molecules can induce a dipole in a nonpolar molecule and their interaction is often referred to as the Debye or the induction interaction.

The physical process that leads to the interactions between nonpolar molecules is the occurrence of the instantaneous dipoles. These instantaneous dipoles occur from random, momentary shifts in charge given by the constant movement of electrons, in other words it is a temporary con-

dition of a charge separation in a molecule due to the environment. The dispersion term is the most important of the three contributions, as it is always present, regardless whether permanent dipoles take part in the interaction or not.

The most commonly used mathematical approximation that describes the energy of interaction between two nonbonding atoms or molecules is the Lennard-Jones potential:

$$U_{LJ} = 4\,\varepsilon \left[\left(\frac{\sigma}{r}\right)^{12} - \left(\frac{\sigma}{r}\right)^{6} \right] \tag{4.18}$$

where, ε is the depth of the potential well, σ is the distance at which the potential becomes zero and r is the distance between interacting molecules. While the term $1/r^6$ describes the attractive interaction, the term $1/r^{12}$ is due to the Pauli repulsion caused by overlapping electron orbitals at short distances [142].

Usually, non-bonded interactions are divided in short and long-range interactions based on the force/distance dependence. Simulations dealing with short-range interactions are performed by introducing a cut-off to the potential at which it decays to zero. However, long-range interactions are more problematic, since not only the simulation cell must be taken in to account but also the effect of its every periodic image must be considered. Later, some of the techniques developed specially for dealing with long-range forces will be discussed.

4.2 Mercedes-Benz model of water

A large number of potential models have been proposed for molecular dynamics simulations of water. The general purpose of these models is to provide a realistic description of intermolecular interactions to mimic the structure and behavior of a real water [143–148]. Development of a model simple enough so that it does not require heavy computational calculations and simultaneously gives physically sound results, which are in good agreement with experiments, is not so trivial.

One of the simplified potentials which reproduces the main structural and thermodynamic properties of water is the so-called 3D Mercedes-Benz model (3D MB) that represents water molecules as Lennard-Jones (LJ) spheres having four arms tetrahedrally oriented [149].

The interaction potential between the LJ spheres is composed of two Lennard-Jones and Hydrogen Bond (HB) terms. Thus the mathematical

description of the model is as follows:

$$U\left(\vec{X_i},\,\vec{X_j}\right) = U_{LJ}\left(r_{ij}\right) + U_{HB}\left(\vec{X_i},\,\vec{X_j}\right) \tag{4.19}$$

here $\vec{X_i}$ represents the coordinates and orientation of the ith particle and r_{ij} is the distance between centers of LJ spheres. The first term is the Lennard-Jones interaction potential, with ϵ_{LJ} depth and σ_{LJ} the contact distance, given by:

$$U_{LJ}\left(r_{ij}\right) = 4\,\epsilon_{LJ}\left[\left(\frac{\sigma_{LJ}}{r_{ij}}\right)^{12} - \left(\frac{\sigma_{LJ}}{r_{ij}}\right)^{6}\right] \tag{4.20}$$

and the second term is the HB term of the total interaction potential:

$$U_{HB}\left(\vec{X_i},\,\vec{X_j}\right) = \sum_{k,l=1}^{4} U_{HB}^{kl}\left(r_{ij},\,\vec{\Omega_i},\vec{\Omega_j}\right) \tag{4.21}$$

where the interaction of HB arms is defined as:

$$U_{HB}^{kl}\left(r_{ij},\,\vec{\Omega_i},\vec{\Omega_j}\right) = \epsilon_{HB}\,G\left(r_{ij} - r_{HB}\right)\,G\left(\vec{i_k}\vec{u_{ij}} - 1\right)\,G\left(\vec{j_k}\vec{u_{ij}} + 1\right) \tag{4.22}$$

$$G\left(x\right) = e^{-x^2/2\sigma^2} \tag{4.23}$$

where $\vec{u_{ij}}$ and $\vec{i_k}$ represent the unit vectors along the distance r_{ij} and along the kth arm of the ith particle, respectively.

Such a mathematical characterization of the model ensures that the strongest hydrogen bond is formed when the arms of two neighboring particles are aligned. However, it has been shown that the original 3D MB model does not reproduce the correct structure (the set of potential parameters used to reproduce the Ice-I_c structure resulted in a much too compact configuration) unless some improvements are made [150].

Later on, an additional parameter has been introduced in the HB term of the potential [151]:

$$U_{HB}^{c}\left(\vec{X_i},\,\vec{X_j}\right) = b\left(z_i\right)\,\sum_{k,l=1}^{4} U_{HB}^{kl}\left(r_{ij},\,\vec{\Omega_i},\vec{\Omega_j}\right) \tag{4.24}$$

where z_i is the coordination of the ith particle and $b\left(z_i\right)$ is an environment dependent parameter that penalizes the hydrogen bond when the interacting particles have more than four neighbors. So that $b\left(z_i\right) = 1$ if $z_i \leq 4$ and $b\left(z_i\right) = \left(\frac{4}{z_i}\right)^{\nu}$ when $z_i > 4$. The atom coordination is given by:

$$z_i = \sum_{k \neq i} f\left(r_{ik}\right) \tag{4.25}$$

$$f\left(r_{ij}\right) = \begin{cases} 1, & r < R - D \\ \frac{1}{2} - \frac{1}{2}\sin\left(\frac{\pi}{2}\left(r - R\right)/D\right), & R - D < r < R + D \\ 0, & r > R + D \end{cases} \tag{4.26}$$

Such a coarse-grained formalism of a potential model, that drops detailed description of water molecules and does not take into account the long-range Coulomb interactions, makes it less computationally demanding and therefore more attractive for long simulations.

4.3 Cashew

The Cashew (Coarse Approach Simulator for Hydrogen Bonding Effects in Water) program was developed for studying the dynamical properties of the Mercedes-Benz model of water through molecular dynamics simulations [151]. The forces and torques (since particles are able to rotate in space) acting on MB particles are computed by differentiating the total energy with respect to displacement and rotation of the particle.

In order to achieve the correct ensemble calculations, the Langevin thermostat and Berendsen barostat have been implemented in the program.

The Langevin thermostat replaces the Newton's equation of motion with the Langevin equation of motion which has an additional frictional and random forces [152, 153].

$$m\,a = f - \gamma\,m\,v + f_{random} \tag{4.27}$$

where m is a particle mass, a is an acceleration, f is a force acting on a particle, γ is a friction constant, v is a velocity of the particle and f_{random} is a random force. The velocity dependence of the friction term in eq. (4.27) is due to the strong time correlation effects that the particle motion exhibits. The random force, which is defined from a Gaussian distribution, ensures that even without an external force, the effect of the particles' Brownian motion is taken into account. The random force is balanced with the frictional force and maintains the system at the desired temperature.

In the framework of this program, the pressure control is performed through the Berendsen barostat which uses the volume as a dynamical

variable during calculations in order to accommodate the pressure change in the system [152, 154]. To maintain constant pressure throughout simulations, the system is coupled to a constant pressure reservoir and the pressure change is described by the following equation:

$$\frac{dP}{dt} = \frac{1}{\tau_P}\left(P_0 - P\right) \tag{4.28}$$

where τ_P is the time constant of the barostat, P_0 is the target pressure and P is the system pressure given by:

$$P = \frac{2}{3\,V}\left(E_k - \Xi\right) \tag{4.29}$$

here E_k is the total kinetic energy, V the system volume and Ξ the internal virial for pair-potentials:

$$\Xi = -\frac{1}{2}\sum_{i<j} r_{ij} \cdot f_{ij} \tag{4.30}$$

f_{ij} represents the force acting on the ith particle form the particle j with a separation distance between them being r_{ij}.

According to the Berendsen pressure coupling scheme, the equation $\frac{dx}{dt} = v$ is modified as:

$$\frac{dx}{dt} = v + \alpha x \tag{4.31}$$

so the volume changes as:

$$\frac{dV}{dt} = 3\alpha V \tag{4.32}$$

The isothermal compressibility β is related to the pressure change through:

$$\frac{dP}{dt} = -\frac{1}{\beta\,V}\frac{dV}{dt} \tag{4.33}$$

and now combining equations (4.32) and (4.33) and taking into account the equation (4.29) gives the modified equation of motion of the Berendsen method:

$$\frac{dx}{dt} = v - \frac{\beta\left(P_0 - P\right)}{3\,\tau_P}\,x \tag{4.34}$$

In order to accommodate the change in pressure, the volume of the simulation box is scaled along with the particle coordinates and the scaling factor μ is given by eq. (4.34):

$$\mu = 1 - \frac{\beta \triangle t}{3\tau_P}\left(P_0 - P\right) \tag{4.35}$$

As has been tested by the authors of this method, the variations of magnitude of the time constant significantly influences pressure/volume fluctuations in the system. The most typical choice for the time constant is 0.1 ps, that provides reliable thermodynamic properties of the system.

4.4 TIP4P model of water

From a computational standpoint, another very attractive potential function for water is the TIP4P (4-point-transferable-intermolecular-potential) function. It involves rigid water molecules (where the internal angles and distances are fixed so the interactions are considered only between points of different molecules) with four interaction sites contributing to the potential energy, proposed by Jorgensen [155–157].

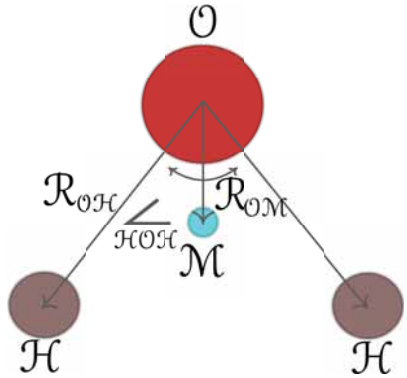

Figure 4.1. Schematic representation of the TIP4P water molecule.

In this model the oxygen site carries no charge but participates in the Lennard-Jones interactions, two positive charges are placed on hydrogen atoms while the negative charge is moved 0.15 nm away from the oxygen along with the bisector of the HOH angle. Bonds in the TIP4P molecule are formed at a rigid angle giving rise to a dipole. The pairwise potential function includes the Coulombic interactions between all intermolecular pairs of charges and the Lennard-Jones interactions between oxygen atoms. Since the model has four interacting sites ten distances are required for calculating the potential function, which increases the computational cost of the model over the preceding potentials, which are presented with fewer interaction sites. However, later analysis of the results obtained with six different potentials (ST2, Bernal-Fowler (BF), SPC, TIPS2, TIP3P, TIP4P [77, 158, 159]) and their comparisons with experimental data showed that the TIP4P yields better estimates for num-

ber of thermodynamic properties (eg. intermolecular energy, heat of vaporization, isothermal compressibility etc.) and provides relatively good structural description (eg. oxygen-oxygen radial distribution function) of the liquid water. However, TIP4P has a very low melting point (for studying solid phases of water), critical point and temperature of maximum density.

Later on, reparametrization of the original TIP4P model gave another set of water potentials (TIP4P-Ew, TIP4P/2005 and TIP4P/Ice [160]), providing the possibility to cover larger range of properties and conditions for simulations. The TIP4P-Ew [161, 162] has been obtained through modification of the total potential energy equation by introducing a long-range correction term in the Lennard-Jones potential using a mean-field approximation in order to account for neglected contributions in the LJ term. The model has been characterized to reproduce well the bulk-density and the enthalpy of vaporization along with other thermodynamic properties of the liquid water over the temperature range of 235.5 - 400 K.

Another specialized TIP4P-like potential that has been developed, by tuning the values of the original TIP4P potential parameters in order to fit the temperature of maximum density, is the so-called TIP4P/2005 [163]. The model gives better predictions for the density, isothermal compressibility, thermal expansion coefficient, heat capacity at constant pressure, heat of vaporization etc., over TIP4P-Ew model, results of which are also known to be in good agreement with the experimental data.

The development of another potential, with the ability to provide a reasonable description of solid phases of water, was a further improvement of the TIP4P-like models. The parameters of the new TIP4P/Ice potential has been chosen to reproduce the phase diagram of ice by analyzing their dependence on the properties of ice [164–166]. The new model reproduces not only the hexagonal ice form (the only stable form found on the earth) but also all the other stable phases included in the phase diagram. The main advantage of the model is its melting temperature which appears to be very close to its experimental value ($T_m = 272.2$ K - TIP4P/Ice, $T_m = 273.15$ K - Experimental). It also provides very good predictions for the melting enthalpy along with the volume phase change.

The difficulty of developing a water potential lies in simplifications (truncation of the long-range Coulomb interactions, constraining molecular geometry to a rigid one with constant angle and bond lengths, etc.) that have to be made in order to achieve better computational effectiveness.

On the other hand, increasing computational power allows one to decrease the number of restrictions and provide a better potential model for study. However, in spite of these restrictions, the TIP4P-like models give quite acceptable predictions for thermodynamic properties of water and ice.

4.5 Gromacs

Gromacs is a programming tool for performing simulations that uses classical mechanics to describe the motion of atoms [167]. Electronic motions are ignored under the assumption that they immediately adjust to atomic positions (once the position of atom changes) and remain in ground state throughout simulations. The general algorithm (the leap-frog integrator by default) takes interaction potential, positions and velocities of atoms as an input, calculates forces, updates the configuration and gives an output. The forces are calculated as a sum of non-bonded pair interactions with the cut-off that is not larger than half of the simulation box size (this method is called the 'minimum-image convention', according to which, only one image of each particle is taken into account in pair-interactions). The program uses the so-called pair list that contains information about pairs of particles for which the non-bonded forces are calculated. This pair list is generated by defining a cut-off radius, the range within force calculations are performed, and updated in every pre-defined step.

4.5.1 Temperature control in Gromacs

Gromacs has several techniques available (Berendsen [152, 168], velocity-rescaling [64] and Nose-Hoover [65, 66, 152, 168, 169] schemes) for temperature control in order to achieve the right ensemble simulations.

The velocity-rescaling scheme alters the system's temperature by scaling velocities. Relation between temperature and kinetic energy is given by:

$$\sum_{i=0}^{N} \frac{|\, p_i \,|^2}{2\, m_i} = \frac{k_B T}{2}\, (3N - N_c) \tag{4.36}$$

where N_c is the number of constraints, so then $3N - N_c$ gives the total number of degrees of freedom. Once the velocity changes (assuming by a factor λ), the corresponding temperature change can be calculated using eq. (4.36) as follows:

$$\triangle T = \frac{1}{2}\sum_{i=1} 2\,\frac{m_i\,(\lambda\,v_i)^2}{(3N - N_c)\,k_B} - \frac{1}{2}\sum_{i=1} 2\,\frac{m_i v_i^2}{(3N - N_c)\,k_B} \tag{4.37}$$

$$\triangle T = \left(\lambda^2 - 1\right) T\,(t) \tag{4.38}$$

$$\lambda = \sqrt{T_0/T\,(t)} \tag{4.39}$$

where, T_0 and $T\,(t)$ are the desired and current temperatures, respectively.

According to the velocity-rescaling scheme, temperature is controlled through simply multiplying velocities, at each time step, by the factor λ. This approach uses the kinetic energy per particle as a measure of the instantaneous temperature, however, does not include temperature fluctuations which are present in the canonical ensemble. This is an obvious disadvantage of the scheme, since the condition of constant temperature does not mean that the kinetic energy per particle remains constant.

Another method to perform isothermal molecular dynamics simulation was proposed by Nose (1984) and further developed by Hoover (1986), nowadays known as the Nose-Hoover thermostat.

The system is presented to be coupled with a thermal bath with its friction parameter ξ. So now the equation of motion is given by:

$$\frac{d^2 r_i}{dt^2} = \frac{f_i}{m_i} - \frac{p_\xi}{Q}\,\frac{dr_i}{dt} \tag{4.40}$$

where, p_ξ is the momentum of the heat bath parameter and characterizes with its own equation of motion:

$$\frac{dp_\xi}{dt} = (T - T_0) \tag{4.41}$$

again T and T_0 represent the desired and current temperatures of the system and Q is the so-called "mass parameter", the magnitude of which determines coupling between the system and the heat bath and it is directly related to the period τ_T of the oscillations of kinetic energy between them:

$$Q = \frac{\tau_T^2\,T_0}{4\,\pi^2} \tag{4.42}$$

The Nose-Hoover approach provides an oscillatory relaxation (heat can flow in and out of the system in an oscillatory fashion) resulting in nearly periodic temperature fluctuations.

4.5.2 Pressure control in Gromacs

Generally, systems at constant pressure are ones that can exchange volume with their surroundings. Due to the fact that its often desirable to perform simulations in the isothermal-isobaric ensemble, different barostat techniques have been implemented in Gromacs for keeping a desired pressure constant through adjusting the simulation volume. One of the techniques is the Berendsen barostat which was described already in section 4.2.1. In Gromacs, the inputs for the Berendsen barostat include the target pressure and the time constant of coupling to a constant pressure reservoir.

Another choice is the so-called Parrinello-Rahman pressure coupling [170], where the simulation box vectors are following the equations of motion and are represented by the matrix b. The equation of motion for the matrix is defined by:

$$\frac{db^2}{dt^2} = V\, W^{-1} b'^{-1} \left(P - P_{ref}\right) \tag{4.43}$$

where V the is the volume of the box, W is the matrix parameter and $P, \quad P_{ref}$ are the current and reference pressures, respectively. Then the modified equation of motion for particles is given by:

$$\frac{d^2 r_i}{dt^2} = \frac{f_i}{m_i} - M\,\frac{dr_i}{dt} \tag{4.44}$$

$$M = b^{-1}\left[b\,\frac{db'}{dt} + \frac{db}{dt}\,b'\right] b'^{-1} \tag{4.45}$$

As an input the program takes isothermal compressibility β_{ij} and the time constant τ_P, which are related to the matrix parameter with the following equation:

$$\left(W^{-1}\right)_{ij} = \frac{4\,\pi^2 \beta_{ij}}{3\,\tau_P^2\,L} \tag{4.46}$$

where L is the largest matrix element of the simulation box. Practically, the instantaneous pressure will oscillate around the target value with a frequency that strongly depends on the matrix parameter.

4.5.3 Non-bonded interactions

An empirical potential energy function that contains information about molecular interactions, such as bond stretching, bending, torsion and non-bonded interactions, is called a molecular mechanics force field. As was

mentioned before, the interactions between non-bonded atoms are usually described through van der Waals (commonly expressed by Lennard-Jones potential) and Coulomb potentials.

In Gromacs, the Lennard-Jones interaction between molecules i and j can be expressed by:

$$V_{LJ}\left(r_{ij}\right) = 4\,\varepsilon_{ij}\left(\left(\frac{\sigma_{ij}}{r_{ij}}\right)^{12} - \left(\frac{\sigma_{ij}}{r_{ij}}\right)^{6}\right) \tag{4.47}$$

Based on the combination rule applied, ε_{ij} and σ_{ij} parameters can be calculated via arithmetic and geometric averages as follows:

$$\sigma_{ij} = \frac{1}{2}\left(\sigma_{ii} + \sigma_{jj}\right) \tag{4.48}$$

$$\varepsilon_{ij} = \left(\varepsilon_{ii}\varepsilon_{jj}\right)^{1/2} \tag{4.49}$$

or using a geometric average for defining σ_{ij} as well:

$$\sigma_{ij} = \left(\sigma_{ii}\sigma_{jj}\right)^{1/2} \tag{4.50}$$

Calculation of non-bonded interactions for a system containing N particles is computationally one of the most demanding tasks, due to the fact that interactions must be calculated for each pair of particles in the system. This results in a problem scaling as N^2. In order to reduce the computational cost, the interaction potential is usually truncated (set to zero) at some cut-off distance [66, 132]. In general, introducing a cut-off distance creates a discontinuity in a potential function (may lead to an unphysical behavior of a system for which the contribution of far away particles is important). On the other hand, calculating the Lennard-Jones interactions beyond the distance where the potential itself becomes negligible (due to its rapid decrease when the separation distance between particles increases) has no scientific benefit. Another reason for using a cut-off is to avoid a particle interacting with itself due to the periodic boundary conditions, which are most commonly applied in simulations.

Further simplifications for short-range interactions are done through creating a neighbor list which contains only the group of particles that fall within some user defined radius that is typically less than or equal to the potential cut-off. The program updates the neighbor list typically after every 10 time steps, in order to account for the motion of particles during the simulation, and computes the interactions for the pairs that fall within its radius [167]. The aim of creating such a list is to avoid

calculations of the distances between every particle pair in order to determine whether they must be included in the potential calculations or not.

As we already mentioned before, the inverse 6th power attractive term $\sim 1/r_{ij}^6$ in the Lennard-Jones potential operates at far distances unlike the repulsion interaction. Therefore, if the cut-off for the potential is defined, part of the dispersion energy is neglected during simulations. In order to account for the long-range effect of the dispersion interaction, Gromacs applies corrections to the pressure and energy of the system [153].

If we consider a system of N particles with a density ρ and a radial distribution function $g\left(r\right)$, then the long-range contribution to the energy V_{lr} can be expressed as:

$$V_{lr} = \frac{1}{2} N \rho \int_0^\infty 4 \pi r^2 g\left(r\right) \left(V\left(r\right) - V_c\left(r\right)\right) dr \tag{4.51}$$

where, $V_c\left(r\right)$ and $V\left(r\right)$ are dispersion energies with and without cut-off, respectively.

By assuming that the radial distribution function is unity beyond the cut-off distance, the dispersion correction to the energy is given by integrating eq. 4.51:

$$V_{lr} = -\frac{2}{3} \pi N \rho C_6 r_c^{-3} \tag{4.52}$$

Similar corrections are performed for pressure. The pressure is expressed by a virial as follows:

$$P = \frac{2}{3V} \left(E_{kin} - \Xi\right) \tag{4.53}$$

where the virial is given by:

$$\Xi = -\frac{1}{2} r_{ij} \cdot f_{ij} = 3 C_6 r_{ij}^{-6} \tag{4.54}$$

and the long range correction to the virial is then:

$$\Xi_{lr} = \frac{1}{2} N \rho \int_0^\infty 4 \pi r^2 g\left(r\right) \left(\Xi - \Xi_c\right) dr \tag{4.55}$$

Again, integration of the eq. (4.55) under the assumption that $g\left(r\right) = 1$ beyond the cut-off defines the correction to pressure as:

$$P_{lr} = -\frac{4}{3} \pi C_6 \rho^2 r_c^{-3} \tag{4.56}$$

So the basic idea is to divide interactions to short and long range and treat them separately in order to increase computational efficiency in simulations. Significant effort has been also made in order to improve the efficiency of estimating long-range electrostatic potential. To state a problem that arises while dealing with long-range Coulomb interactions, let's consider a system with N particles in vacuum, placed at $\mathbf{r}_1, \ldots \mathbf{r}_N$ locations with point charges $q_1, \cdots q_N$. Then the total interaction energy of a system is written as:

$$E = \frac{1}{4\,\pi\,\varepsilon_0} \sum_{(i,j)} \frac{q_i\,q_j}{\mid \mathbf{r}_{ij} \mid} \tag{4.57}$$

where $\mathbf{r}_{ij}$ is the distance between particles, and ε_0 the vacuum permittivity.

Now applying the periodic boundary conditions means that each particle has a periodic image particle located at $\mathbf{r}_i + n_1\,\mathbf{c}_1 + n_2\,\mathbf{c}_2 + n_3\,\mathbf{c}_3$, with $\mathbf{c}_1$, $\mathbf{c}_2$, and $\mathbf{c}_3$ being simulation box vectors. Now the total interaction energy for such a periodic system includes the interactions between periodic images.

For simplification the vector $n_1\,\mathbf{c}_1 + n_2\,\mathbf{c}_2 + n_3\,\mathbf{c}_3$ can be replaced with $\mathbf{n}\,L$. Where L represents the characteristic length of the box. Considering a cubic supercell, the total Coulomb interaction energy can be written as:

$$E = \frac{1}{4\,\pi\,\varepsilon_0}\,\frac{1}{2} \sum_{\mathbf{n}} \sum_{i=1}^{N} \sum_{j=1}^{N} \frac{q_i\,q_j}{\mid \mathbf{r}_{ij} + \mathbf{n}\,L \mid} \tag{4.58}$$

The factor 1/2 appears to make sure that each interacting pair is counted only once. To overcome a slow convergence of the above sum, the Ewald Summation method has been developed [171]. It separates the part of the electrostatic interaction which decays fast (part that can be ignored beyond the cut-off distance) from the part which has larger decay distance. Such decomposition of the interaction potential allows summation of the short-range competent in real space and the long-range component in Fourier space.

The computational cost of the the summation can be further reduced by using the Particle-mesh Ewald method (PME) [172], which performs Ewald summation of the reciprocal term on an interpolating grid. Then the accuracy and speed of calculation depend on the determination of the maximum number of grid points (where the potential is calculated) and the interpolation scheme.

4.5.4 Constraint algorithm

Generally, constraint algorithms have been proposed because of the high frequency atomic bond oscillations presented in a molecule. So the explicit simulation of the intramolecular dynamics adds some limitations to the time step, which now must be shorter than the period of these oscillations, making simulations computationally very expensive. The time step in molecular simulations can be increased by treating atomic bonds as rigid and solving equations of motions under these constraints.

One of the most popular algorithms for constraint simulations available in Gromacs is the Linear Constraint Solver (LINCS) [173]. The Newton's equation of motion for a system containing N particles is given by:

$$\frac{d^2 r}{dt^2} = M^{-1} f \tag{4.59}$$

where $r\,(t)$ and f are a $3\,N$ coordinate and force vectors respectively and M is a $3\,N \times 3\,N$ mass matrix.

According to the LINCS algorithm the system is constrained by time-independent constraint equations:

$$g_i\,(r) = 0; \qquad i = 1, \ldots, K \tag{4.60}$$

Then the constraints multiplied by Lagrange multipliers $\lambda_i\,(t)$ are added to the potential as a zero term:

$$-M\,\frac{d^2 r}{dt^2} = \frac{\partial}{\partial r}\,(V - \lambda\, g) \tag{4.61}$$

$$B = \frac{\partial g}{\partial r_i}; \qquad -M\,\frac{d^2 r}{dt^2} + B^T\,\lambda + f = 0 \tag{4.62}$$

According to the eq. (4.60), the first and second derivatives of the constraints can be also set to zero:

$$\frac{dg}{dt} = B\,\frac{dr}{dt} = 0 \tag{4.63}$$

$$\frac{d^2 g}{dt^2} = B\,\frac{d^2 r}{dt^2} + \frac{dB}{dt}\,\frac{dr}{dt} = 0 \tag{4.64}$$

By introducing a new notation $T = M^{-1} B^T \left(B\,M^{-1} B^T\right)^{-1}$ we obtain the new constrained equation of motion as follows:

$$\frac{d^2 r}{dt^2} = (1 - T\,B)\;M^{-1} f - T\,\frac{dB}{dt}\,\frac{dr}{dt} \tag{4.65}$$

which is then implemented into the integration algorithm applied in simulations.

4.6 Setup

The system we studied consisted of two parallel slabs of ice Ih, each measuring approximately $3 \times 3 \times 3$ nm^3, stacked on top of each other along the z-coordinate of the rectangular simulation box. Both slabs had a similar orientation, exposing the (0001) surface perpendicular to the z-axis. In order to control the distance between the two slabs, and account for the missing macroscopic continuation of the system, the molecules in one of the outer layers in each slab were restrained in a harmonic potential acting in the z direction. Periodic boundary conditions were applied along x, y and z, and $\sim$10 nm of vacuum was added to the simulation box along z, to minimize spurious interactions with periodic images. In order to simulate friction measurements at constant sliding velocity, the centers of mass of the two slabs were pulled in opposite directions along the x direction, parallel to the surfaces. The harmonic potential in which the centers of mass were pulled had a force constant of 10^4 kJ/mol/nm^2. The harmonic potential used to control the inter-layer distance, as well as the applied load in the friction simulations, was applied to a single layer of water molecules in each slab and had a force constant of $15\ 10^3$ kJ/mol/nm^2. All quantities of interest were computed from system configurations saved every 5 ps from 5 ns MD trajectories, after performing a single slab simulations for 5 ns to study the surface structural properties of ice. The system is depicted in Figure 4.2.

The two ice slabs were initially well separated in the simulation box and slowly brought in contact by a constant pulling velocity in the z direction ($v = 0.001$ nm/ps). Once at a predefined distance, measured by the constrained layers, the z coordinates of these layers were fixed and pulling in the x-direction could start. The effective load during sliding was then represented in terms of an average harmonic force acting on the constrained layer perpendicular to the sliding direction and controlled by varying the separation.

The TIP4P potential series [155, 160, 163, 164] were used to describe atomistic interactions, and molecular dynamics simulations and data analysis were carried out using the Gromacs (version 4.5.3) simulation package [167]. The Lennard-Jones and short-range electrostatic interactions

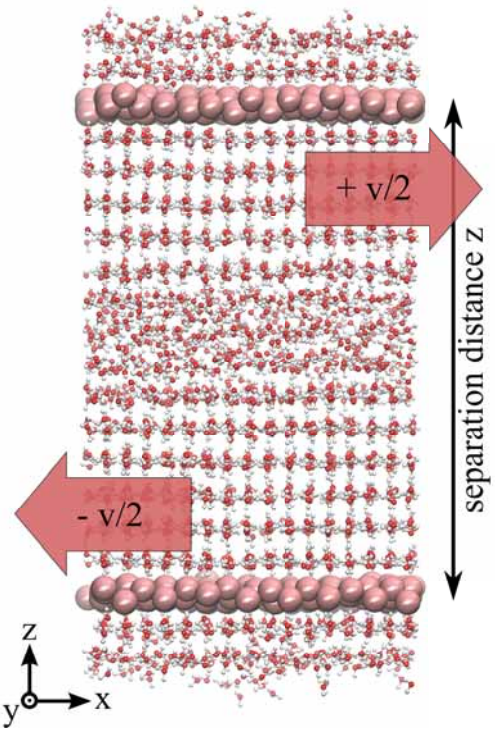

Figure 4.2. System of two ice slabs separated by a liquid region (sliding interface) used for friction studies. Harmonically restrained water molecules are represented by pink beads. Applied load is controlled through their separation distance in z. Red arrows indicate the pulling direction along x. Published in ref. [174]

.

were truncated at 0.9 nm, and an analytic correction to the dispersion term was applied. The Particle-mesh Ewald (PME) scheme was used to treat the long-range electrostatics. The equations of motion were integrated with the Leapfrog algorithm using a 1 fs timestep. A Nosé-Hoover thermostat with a 0.1 ps time constant was applied to the system.

The orientational order parameter proposed by Errington and Debenedetti [175] was used to study the effect of premelting and friction on the ice surfaces. It is a measure of the local tetrahedrality around molecule i, defined as:

$$q_i = 1 - \frac{3}{8}\sum_{j=1}^{3}\sum_{k=j+1}^{4}\left(\cos\phi_{ijk} + \frac{1}{3}\right)^2, \tag{4.66}$$

where ϕ_{ijk} is the angle between the oxygen atom of molecule i, and the oxygen atoms on two of its neighbors, j and k. q_i takes the value of 1 for a perfect tetrahedral structure, and 0 for complete disorder. In practice, the order parameter is about 0.95 in bulk ice and of the order $0.5 - 0.85$ in

liquid water.

5. Atomic level simulations of friction at an ice-ice interface

Molecular dynamics simulations have long been applied to study non-equilibrium atomistic processes such as friction. Atomistic mechanisms of the frictional stick-slip behavior have been studied by several authors, using various materials [176]. The behavior was observed while sliding a Si tip on a Si(111) surface, a Cu tip on a Cu(100) surface as well as between two hydrogen-terminated diamond surfaces [176–179]. The study of an adhesive contact formation during sliding and wear phenomena (reconstruction, material transfer) has been a matter of great interest and various results have been reported in this area [177, 180].

The simulations have been performed to demonstrate the energy dissipation during sliding caused by the plastic deformation in the near-surface regions. A typical 'plowing' process was observed due to the differences in the intermolecular forces of the sliding materials, which were used in simulations [181]. Furthermore, the nanoscale roughness and its role in calculated friction has also been addressed through the molecular dynamics investigations [182].

The above discussion focuses on the studies of the frictional behavior on dry surfaces. In this work, we present the MD simulations of friction of a smooth ice-ice interface, which is determined by the lubricating effect of a liquid-like premelt layer (completely separating the surfaces) between the sliding ice sheets. So far, studies of lubricated sliding have been mainly concentrated on the properties of the lubricant itself [183–185]. We study the effect of the liquid-like premelt layer thickness on the resultant frictional force. In general, increasing temperature or load leads to a thicker lubricating layer and lower friction, while increasing the sliding velocity increases friction due to viscous shear.

5.1 Ice surface

Firstly, the nature of a free surface of ice, using the three dimensional Mercedes-Benz (MB) model, was examined in order to establish the surface premelting. The main advantage of the MB model, over other atomistically more accurate models, such as transferable intermolecular potential (TIP), simple point charge (SPC) and others, lies in its simplicity of describing water molecules. While the model follows the nature of freezing and melting of water quite accurately (e.g. freezing into an open-packed configuration at ambient temperature, increasing density upon melting until the temperature of maximum density is reached) it does not follow the dynamics of the surface structure in response to temperature change.

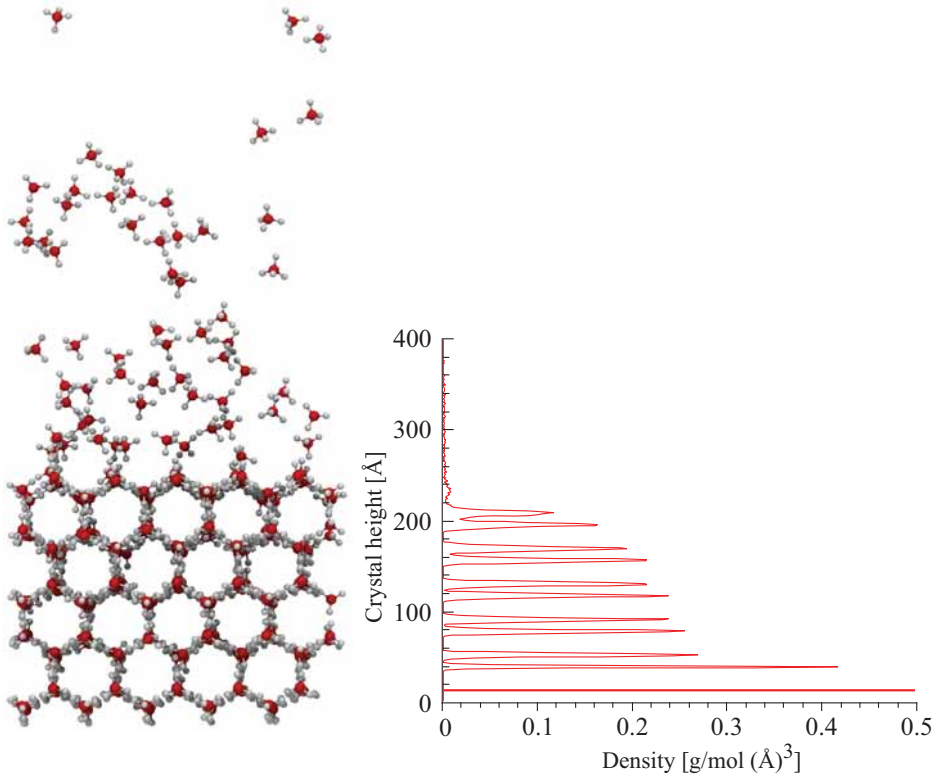

Figure 5.1. Simulations of the ice surface with MB model of water at 270 K. Water molecules in the last couple of layers were fixed during simulations. Calculated density as a function of a crystal height.

Simulations showed that below the melting point, the crystal structure remains perfectly ordered, however, as the temperature increases close to the melting point evaporation of the surface molecules is observed (see Fig. 5.1). The set of potential parameters were tuned with the purpose of

weakening the interaction between molecules but this led to similar results and we concluded the MB model was unsuitable for surface studies.

The investigation to establish a good model of ice was continued by examining other, most popular, potentials for water. For comparison, we used the SPC, TIP4P, TIP4P/2005 and TIP4P/Ice with melting temperatures of 190 K, 232.0 K, 252.1 K and 272.2 K, respectively [8].

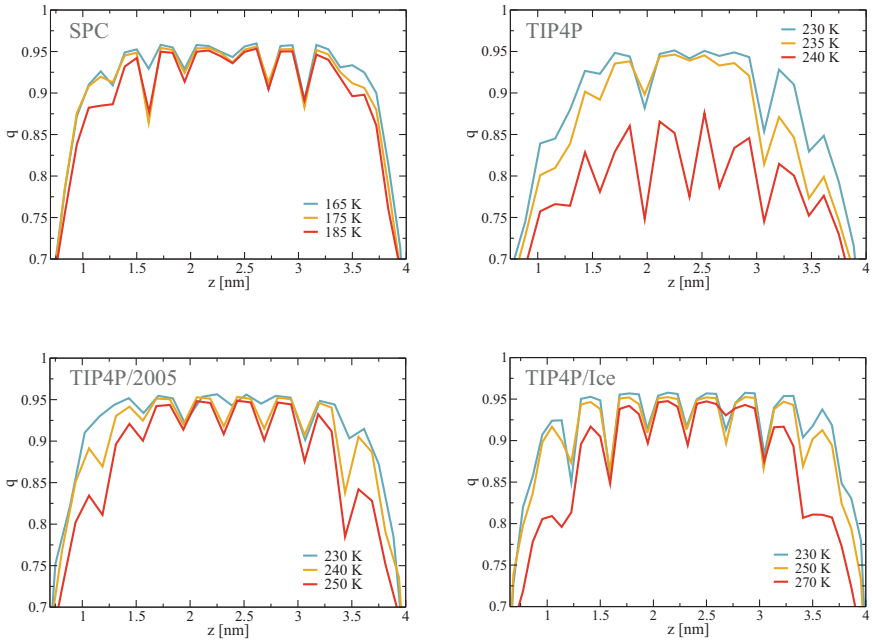

Figure 5.2. Calculated order parameter for TIP4P, TIP4P/2005, TIP4P/Ice and SPC models of water below their melting temperatures.

Due to the differences in melting points, also the premelting temperatures (temperature at which the disordered layer thickness reaches 1 Å [8]) were seen to depend on the potential, but in all cases the thickness of the premelted layer increases with temperature and typically stays in a range of a few molecular layers in the simulations. The thickness of the premelted layer observed in different experiments shows a wide variability, depending on measurement techniques used. However, values obtained in our simulations, within the temperature range of 240 - 270 K, for the basal plane of ice, are in a good agreement with the results reported by Bluhm (photoelectron spectroscopy studies) and Conde (molecular dynamics studies) [8, 99]. Figure 5.2 shows the order parameter, calculated as a function of surface depth, for the SPC, TIP4P, TIP4P/2005 and TIP4P/Ice

water potentials at temperatures below their melting points illustrating the similarity in premelting behavior. The number density profiles calculated for the TIP4P/Ice system at minimum (230 K) and maximum (270 K) temperatures indicate a layered structure of the premelt (see Fig. 5.3).

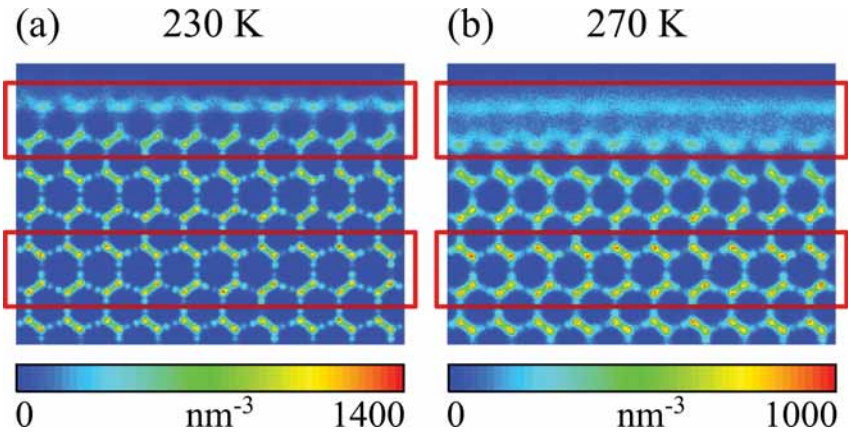

Figure 5.3. Time-averaged number density map perpendicular to the ice-vacuum interface, at a temperature of 230 K (a) and 270 K (b), illustrating the structural difference between bulk ice and premelt layer at the surface. Lateral density maps within the surface and bulk regions indicated in red are shown in Fig. 5.4. Published in ref. [174]

In addition, density profiles calculated separately for the bulk and the surface layers, at 230 K and 270 K temperatures, show the difference between the crystalline order and the surface disorder (see Fig. 5.4), more pronounced close to the melting point (see Fig. 5.4 (b) and (d)).

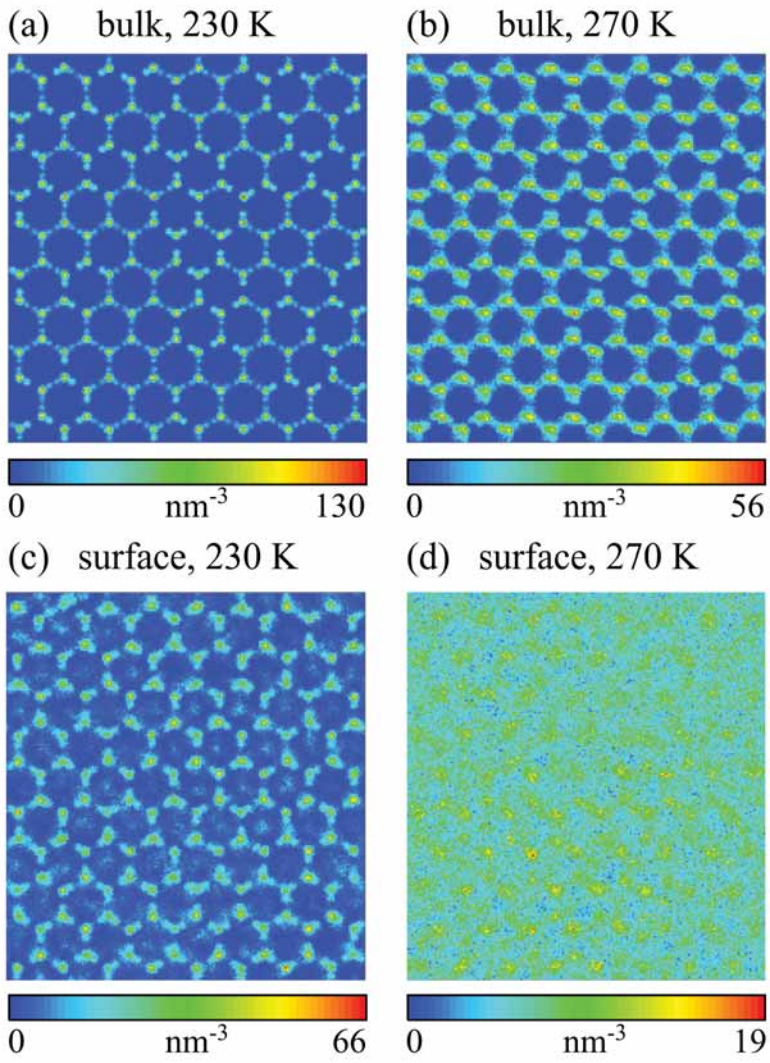

Figure 5.4. Time-averaged lateral number density maps within slabs of bulk ice at 230 K (a) and at 270 K (b), and within the surface premelt layer at 230 K (c) and at 270 K (d). At 230 K, the surface (c) still exhibits lateral order similar to that in bulk (a), whereas close to the melting point, the premelt layer is quasi-liquid like (d), while the bulk is still solid ice (b). Published in ref. [174]

We chose TIP4P/Ice, which matches the experimental melting temperature [164], for further studies of friction and do not expect the results to depend significantly on the flavor of the TIP4P model beyond the temperature scale.

Since the premelting varies with the facet orientation of a crystal, due to differences in packing densities, we compared the surface dynamics of basal and prismatic faces. The surface simulations were performed for each facet orientation separately at 270 K during the 10 ns simulation

time. The calculated order parameter shows a clear difference between progression of the surface disorder (see Fig. 5.5). The premelting establishes (liquid-like layer reaches its equilibrium thickness) faster when the basal face is exposed to vacuum.

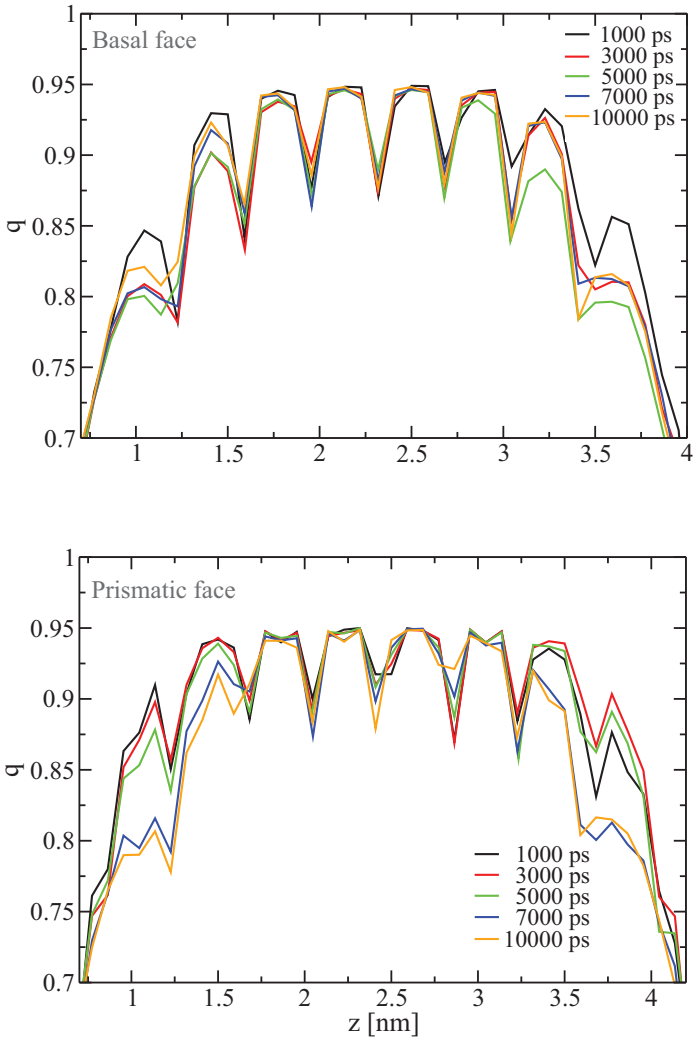

Figure 5.5. Variation of the average local order parameter q along the cross-section of a thin slab of TIP4P/Ice model for basal (top figure) and prismatic (bottom figure) faces exposed to vacuum.

5.2 Ice-ice surface

When the formation and growth of the liquid layer at the surface of ice is greatly influenced by the temperature, then its frictional behavior is also expected to be temperature dependent.

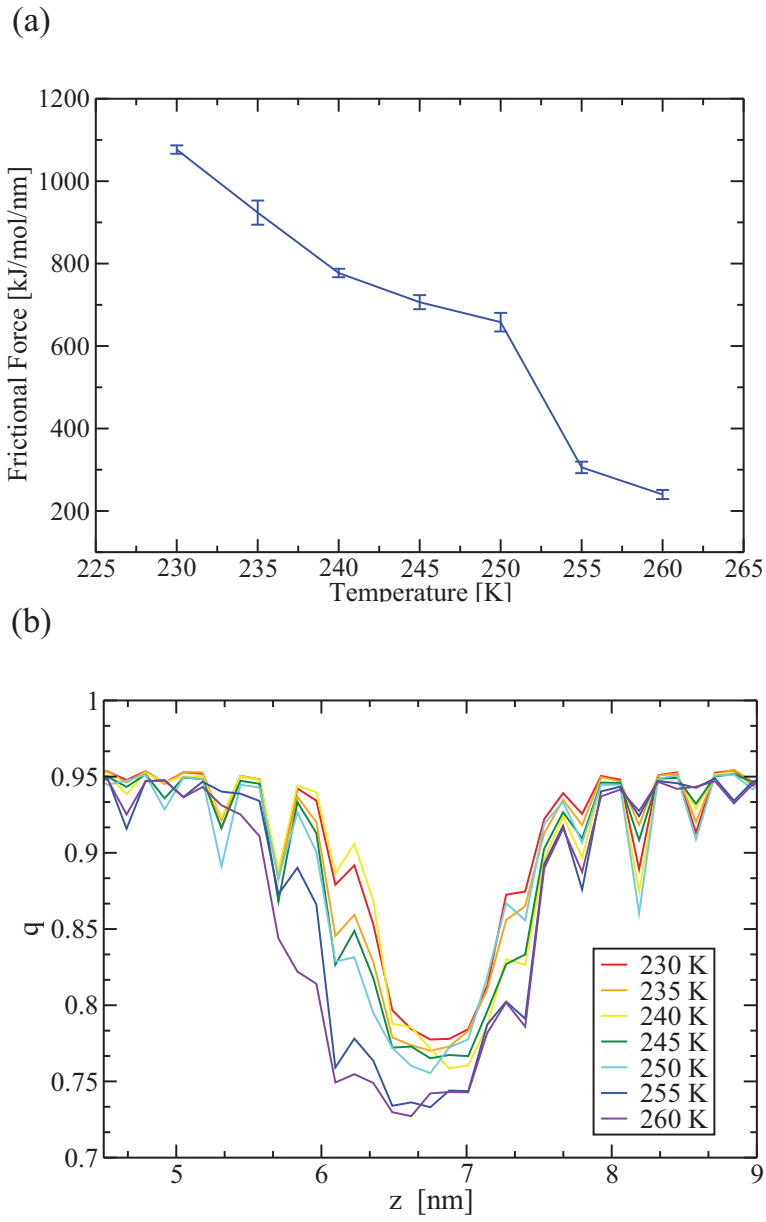

Figure 5.6. Temperature dependence of frictional force, at constant sliding velocity v=4 nm/ns, in the repulsive load regime (separation distance 5.4 nm) (a). Calculated order parameter for each temperature, along the z-coordinate perpendicular to the sliding direction (b). Published in ref. [174]

Figure 5.6 (a) shows the temperature dependence of friction for a ”moderate load” case. The lowering of friction as temperature rises can be understood in terms of increased lubrication. Generally, the molecules at the interface will form hydrogen bonds between each other resisting sliding, but in the premelt the molecules are less coordinated (q is lower, see Fig. 5.6 (b)) and so are also more weakly bound. The thickness of the premelt layer increases with temperature resulting in better lubrication at the ice - ice interface. Also, due to the increased thermal motion of the molecules at higher temperatures, the average hydrogen bond strength effectively weakens [72].

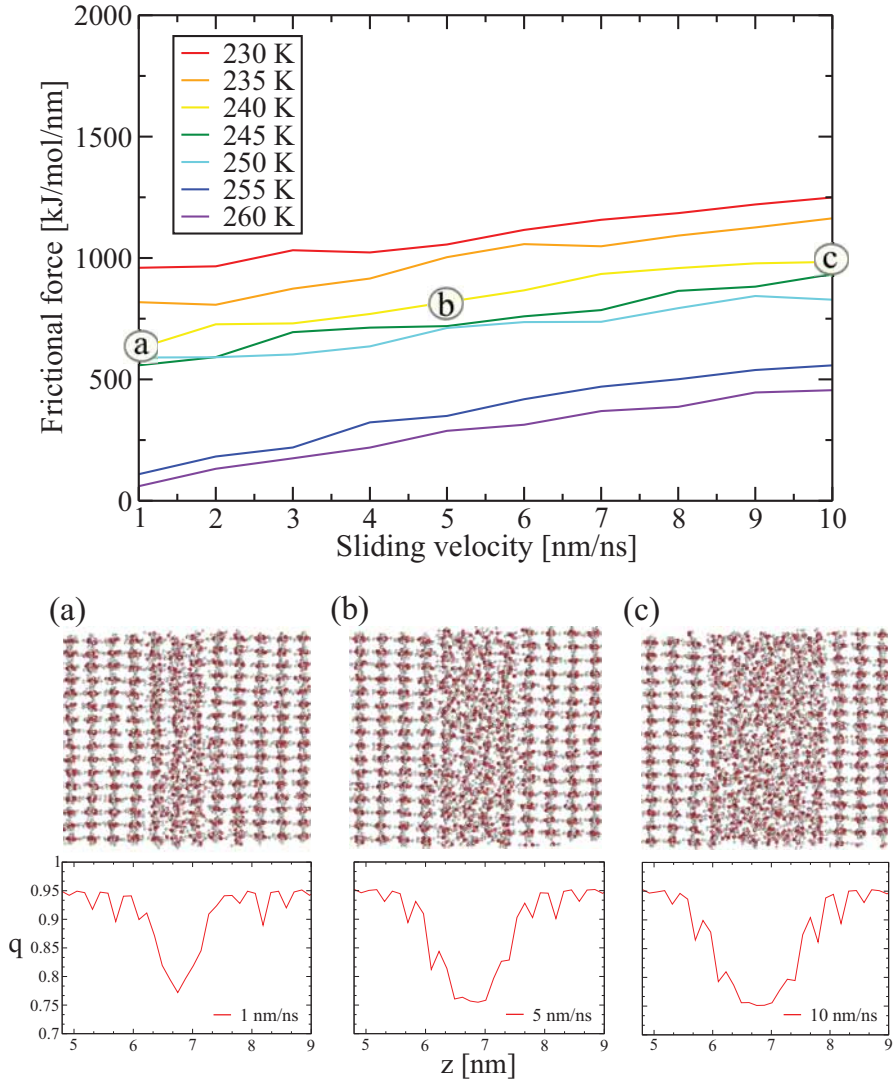

Figure 5.7. Frictional force as a function of sliding velocity for different temperatures with the distance between harmonic layers of ~ 5.4 nm. Existing larger gap between frictional forces from 250 to 255 K is due to the rapid increase of the interfacial liquid layer thickness at that temperature interval. Snapshots of the sliding interface and calculated order parameters for (a) $v = 1$ nm/ns, (b) $v = 5$ nm/ns and (c) $v = 10$ nm/ns at 240 K. Published in ref. [174]

Similarly also the sliding velocity influences friction, since it is directly related to the frictional heating and therefore plays significant role in the resulting lubrication. At higher sliding velocities, more frictional heat is generated, increasing the thickness of the interfacial water layer. During sliding, frictional heating will locally raise the temperature at the contact

layer. However, in order to separate the effects of heat and sliding velocity, the temperature of the liquid layer was also kept approximately constant with the thermostat during simulations. Friction is seen to increase linearly with increasing sliding velocity, which can be interpreted to be due to viscous shear in the liquid layer between sliding surfaces.

Next, we examine the effect of load on friction. As the two ice slabs are brought together, the thickness of the liquid layer between them decreases initially. This happens because when the ice sheets are far apart, in the negative load regime, water molecules fill the small void between the surfaces. As the slabs are pressed together, the liquid layer is at first confined in a smaller space, increasing the density, until at a high load the amount of liquid starts to increase due to pressure melting. At this point the thickness of the liquid layer starts to increase again. Furthermore, the diffusion coefficient (computed using the Einstein relation) of water molecules confined at the interface decreases with the slab separation (see Fig. 5.8)

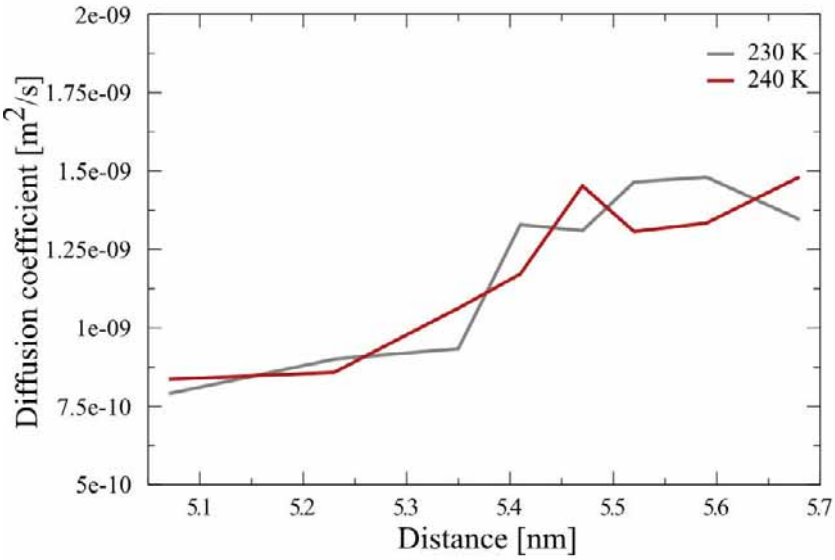

Figure 5.8. Diffusion coefficient of water molecules confined between ice slabs, as a function of separation distance between harmonically restrained layers, with the sliding velocity of 4 nm/ns, at temperatures of 230 K and 240 K. Published in ref. [174]

The correspondence between effective load and slab separation is shown in Figure 5.9. Also here, it is apparent that we cross from attractive

regime (negative load) to repulsive regime (positive load) when the constraining force changes sign.

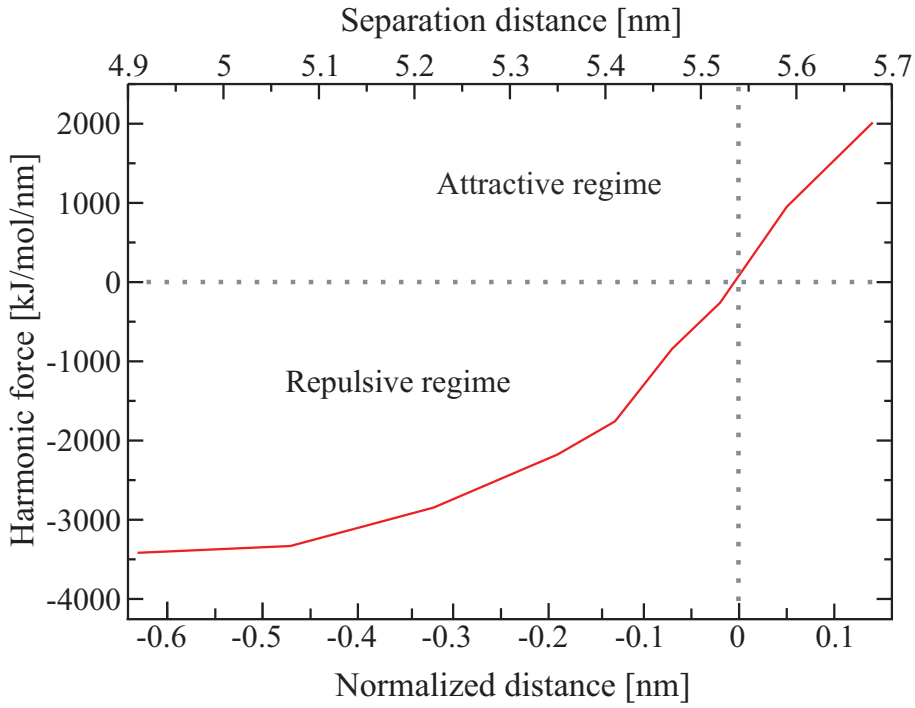

Figure 5.9. Separation distance between harmonically restrained layers represented as an effective normal force. Dashed lines separate positive (repulsion) and negative (attraction) load regimes. Published in ref. [174]

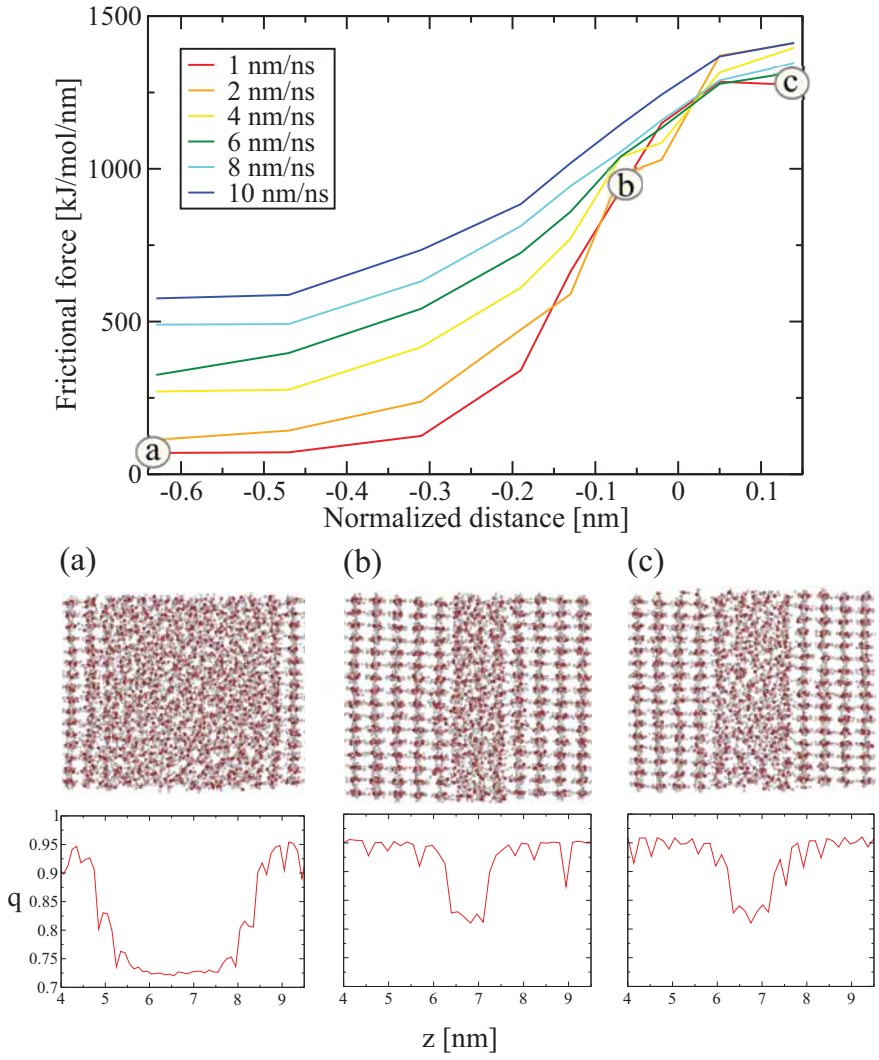

Figure 5.10. Frictional force as a function of normalized separation distance between harmonically restrained layers for different sliding velocities at 240 K. Snapshots of the sliding interface and calculated order parameters for (a) -0.63, (b) -0.14, and (c) 0.16 separation distances with sliding velocity of $v = 1$ nm/ns. Published in ref. [174]

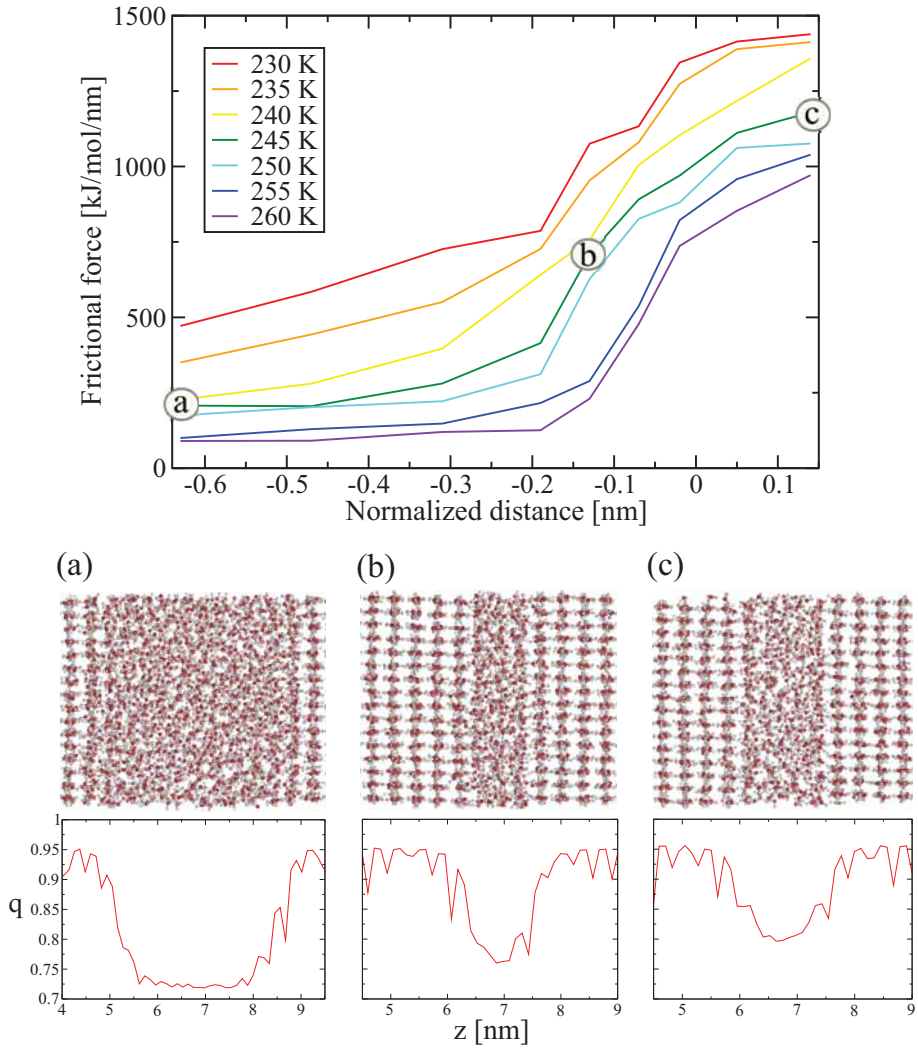

Figure 5.11. Frictional force as a function of normalized separation distance between harmonically restrained layers for different temperatures with sliding velocity of $v = 4$ nm/ns. Snapshots of the sliding interface and calculated order parameters for (a) -0.63, (b) -0.24, and (c) 0.16 separation distances at 245 K. Published in ref. [174]

The effect of load on friction is shown in Figures 5.10 and 5.11 in tandem with both the sliding velocity (see Fig. 5.10) and temperature (see Fig. 5.11). In all cases, in the attractive regime, friction decreases weakly as the slabs are brought closer. Near the crossover to the repulsive regime, we see a rapid drop of friction followed again by fairly weak load dependence in the repulsive regime. Finally, by transforming from separation to load using the dependence of Fig. 5.9, we can calculate the coefficient of friction. This is shown in Fig. 5.12 where the friction coefficient is seen to decrease linearly with temperature and increase with velocity. The co-

efficient is also found to decrease as the applied load increases (see Fig. 5.13), whereas the effect of adhesion is seen at lighter loads.

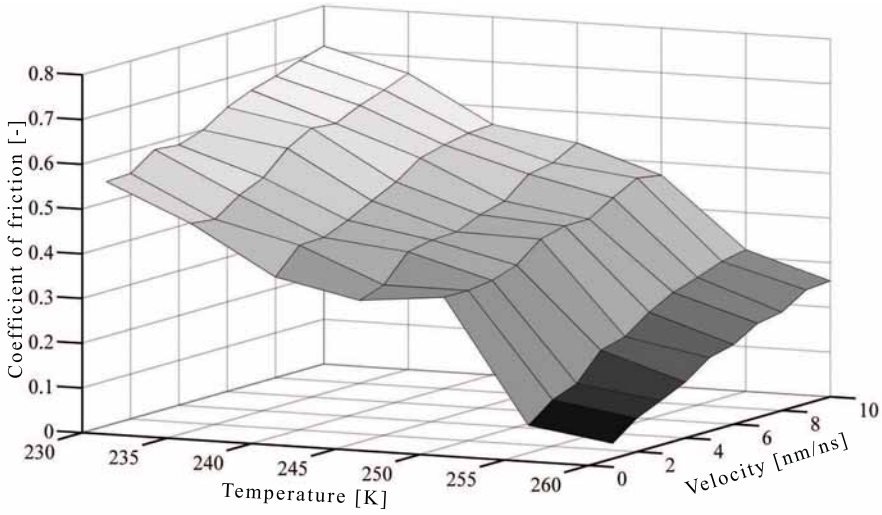

Figure 5.12. Coefficient of friction as a function of temperature and sliding velocity. Published in ref. [174]

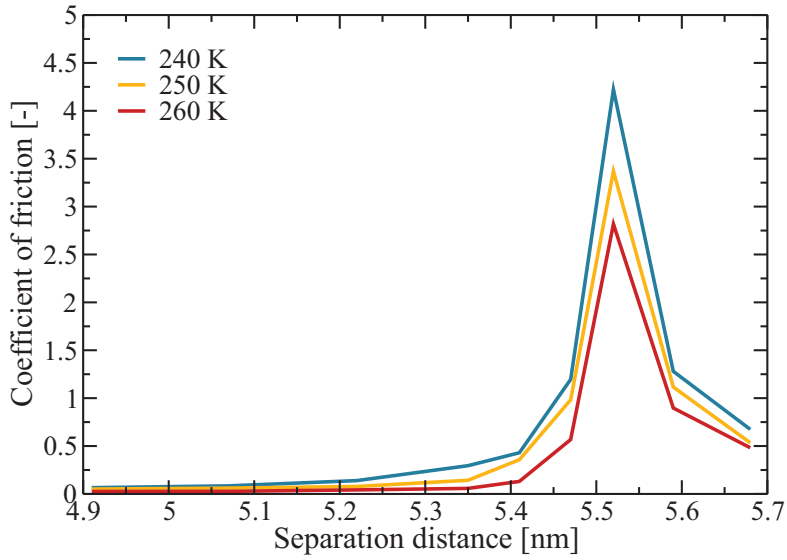

Figure 5.13. Coefficient of friction as a function of separation distance between harmonically restrained layers (applied load) at 240 K, 250 K, and 260 K temperatures. The coefficient increases rapidly around 5.6 - 5.5 nm separation where the load goes from attractive to repulsive regime as the slabs are pressed together. This can be explained by the attraction between interface water molecules at smaller loads resisting sliding. Published in ref. [174]

5.3 Frictional heating

The mechanism of easy sliding on ice and snow has often been understood in terms of a layer of water formed by pressure melting. This was supported by the fact that generally the real area of contact between two surfaces is only a small fraction of the apparent area, so the entire load is carried by these minute contacts at the interface, greatly increasing the pressure locally that can easily reach a value of the flow pressure of a material [11, 27]. This situation is mostly seen in metals while with a powder such as snow, which can pack down under applied load and shape around the slider, the area of real contact is expected to be greater. Later, experience showed that the pressure melting during sliding on ice and snow (skating or skiing) is considerable only at temperatures close to the melting point.

The development of heat at the sliding interface by friction is another

phenomenon that can produce appreciable surface melting of ice. Sliding friction is usually regarded to be the force acting in the opposite direction of motion involving very complicated mechanisms of energy dissipation. A simple assumption that friction arises from interlocking surface asperities or interacting surface molecules does not provide a satisfactory description of how exactly do these interactions lead to energy dissipation which is manifested as heat in the system. The mechanism is easy to explain in terms of plastic deformation and material damage, however in cases where no plastic deformation and wear occurs the nature of energy dissipation becomes obscure [186].

According to David Tabor [186], who summarized the fundamental concepts of frictional heating for elastic and near elastic sliding, atoms at the sliding interface are moved from their equilibrium position and therefore reach an unstable arrangement. When they adapt a new equilibrium configuration the strain energy releases in the form of atomic vibrations that devolve to heat.

Simple calculations of the heat released at the interface when sliding on ice, performed by Bowden and Hughes, showed surface temperature increase from -20 to $0°\mathrm{C}$. These calculations were carried out for real macroscopic systems, but very often interfacial friction is modeled at the atomic scale in order to find microscopic origins of this complex phenomena [11]. Through such atomistic models friction is defined as the energy 'lost' or in other words converted to heat while surfaces move across some distance of atomic dimensions.

In our system, the heat that is possibly generated at the interface is taken away from the system by the thermostat that is applied to all atoms in order to simulate frictional steady state. The thermostat guarantees oscillatory relaxation of the system to the target temperature while the strength of coupling is controlled by the period of these oscillations. As a first test different coupling times (periods) were applied.

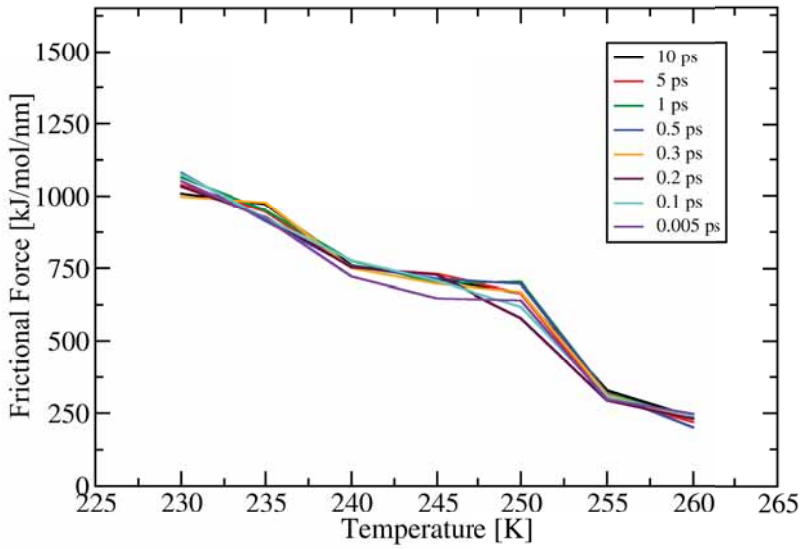

Figure 5.14. Frictional force as a function of temperature for different coupling times of the Nose-Hoover.

Figure 5.14 shows almost no difference in calculated frictional force as a function of temperature for different coupling times, therefore we used 0.1 ps in all cases.

Now, it is important to mention that such an artificial equilibration of the system could lead to incorrect atomic trajectories and therefore description of the process. In order to check the validity of our results a different approach of thermostatting the system was applied in the simulations. In particular, as a test, the thermostat was applied only to a couple of layers, far away from the interface, in each slab. Calculated dependences of the frictional force on temperature, sliding velocity and applied load for both coupling schemes are illustrated in Fig. 5.15.

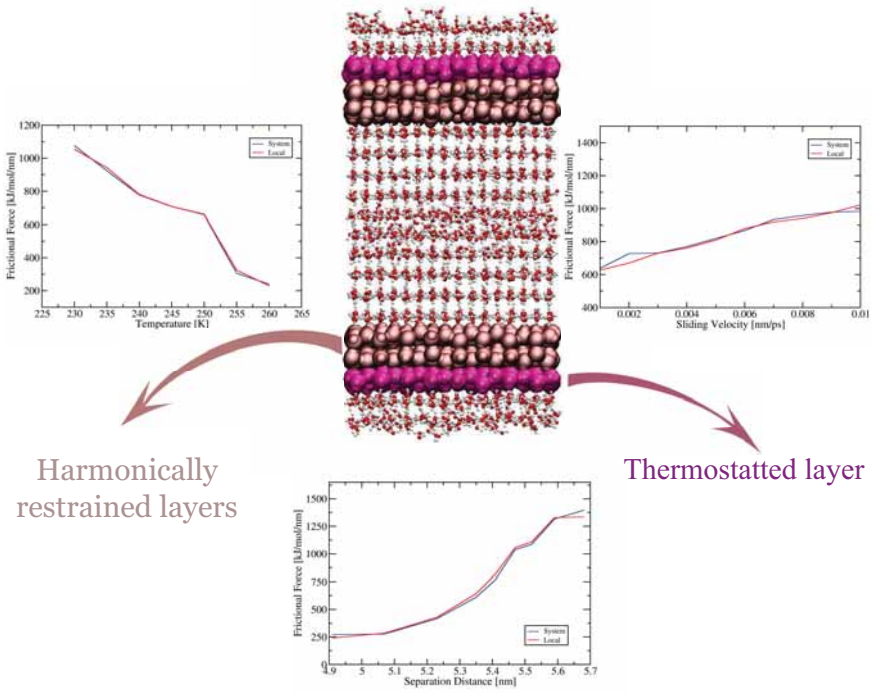

Figure 5.15. Schematic presentation of the locally thermostatted system of two slabs of ice in sliding contact. Comparison between frictional forces as a function of temperature (left), sliding velocity (right) and applied load (middle) when the system is locally and fully coupled to the thermostat.

No significant differences between results is either due to no frictional heating in our system or can be also related to the size of our system being small relative to the coupling strength of the thermostat. This means that if the frictional heat is generated during sliding, heat transfer through the system (from the interface to the thermostatted layer) establishes faster than interfacial melting.

According to B. Persson [28], the temperature rise at the sliding interface due to frictional heating is defined through the heat diffusion law as follows:

$$\triangle T = \frac{2\,J}{\lambda}\left(\frac{\kappa\,t}{\pi}\right)^{1/2} \tag{5.1}$$

where $\triangle T$ is the temperature increase at time t and J is the heat current that flows into the contacting solids. The thermal diffusion coefficient κ is defined as:

$$\kappa = \frac{\lambda}{\rho\,C_v} \tag{5.2}$$

here λ is the thermal conductivity of a material, ρ the mass density, and

C_v the heat capacitance.

In order to achieve steady sliding of surfaces with the shear stress of σ_k required for sliding with the relative velocity of v, energy of $v\,\sigma_k$ is necessary. Now assuming that entire energy is converted into heat, and the system of interest consists of two identical materials then by symmetry:

$$J_1 = J_2 = \frac{v\,\sigma_k}{2} \tag{5.3}$$

Calculations performed for ice sliding against ice system for two different values of the kinetic friction coefficient ($\mu_k = 0.02$ corresponding to sliding with a water film and $\mu_k = 0.3$ sliding without a water film) which is used to define the shear stress as:

$$\sigma_k = \mu_k\,\sigma_0 \tag{5.4}$$

with a yield stress of $\sigma_0 = 0.4 \times 10^8$ N/m^2, $\rho = 1000$ kg/m^3, $C_v = 2100$ J/kg K, and $\lambda = 2.3$ W/m K, showed that the temperature raise at the junction of 100 μm diameter for 1 m/s speed is 2 K for lubricated sliding and 30 K in the absence of the liquid film.

Based on these calculations no significant temperature rise should be expected in our system due to its nanoscale dimensions and the friction regime that is always hydrodynamic. Calculation results of the average velocity for each atomic layer in the system is shown in Fig. 5.16.

(a)

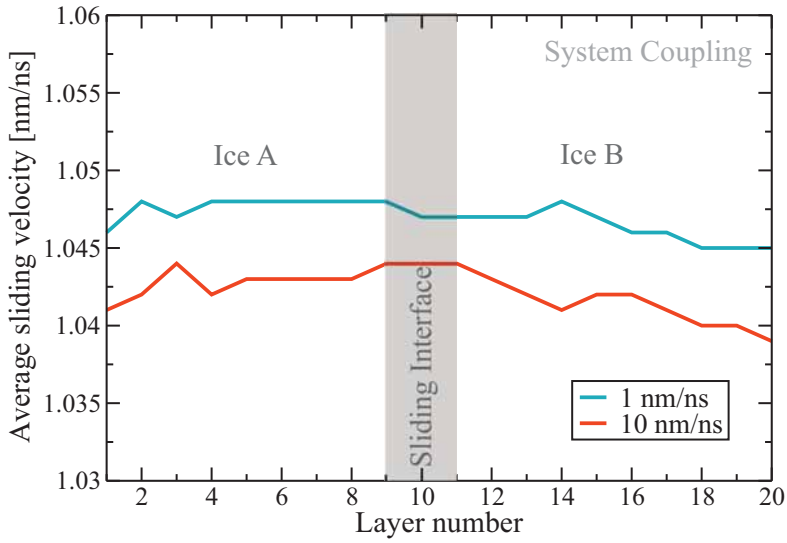

(b)

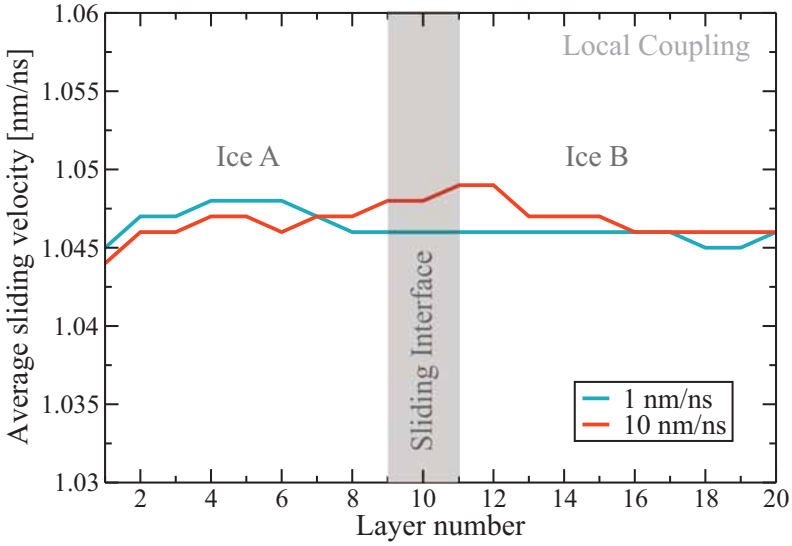

Figure 5.16. Calculated average sliding velocity (averaged over 5000 ps simulation time) of each atomic layer in the system while the thermostat is applied to the entire system (a) and locally to couple of layers far away from the sliding interface (b). Simulations were performed at 230 K temperature and for maximum (v=10 nm/ns) and minimum (v=1 nm/ns) sliding velocities.

Firstly, coordinates of each atom were obtained and corresponding velocities calculated in every 1 ps. This was followed by calculating the average

velocity of each monolayer in our system and then averaged over simulation time. Analyses were performed for minimum and maximum sliding velocities at 230 K and for both approaches of the temperature control. Calculations showed no increase of the velocity and therefore temperature at the sliding interface.

6. Friction of contaminated ice-ice system

The coefficient of friction of ice during sliding is about one order of magnitude lower than that of other solids, nevertheless it is not constant and can be affected by many factors such as temperature, sliding velocity, and applied load. Significance of ice surface premelting in friction was pointed out in the previous chapters. Furthermore, a theoretical analysis by J. Wettlaufer suggests that the premelted layer thickness can be extremely sensitive to small impurity concentrations [187]. A number of recent experiments clearly demonstrate the important role of surface contamination in enhancing the extent of premelting. A recent molecular dynamics study further demonstrates how impurity ions at the ice surface can reduce the inhibition of molecular vibrations at the surface and consequently increase the thickness of the premelted layer [188]. Therefore, in this chapter the effect of Na^+ and Cl^- ions on the surface premelting as well as sliding friction will be discussed.

6.1 Setup

The method of simulating contaminated ice friction is very similar to that used in case of pure ice (see section 4.4). The MD simulations were performed using the TIP4P/Ice potential with the Gromacs 4.5.3 software package. The Lennard-Jones and electrostatic interactions were treated similarly. The only difference is the introduction of an ion-ion and ion-water interactions to the potential.

The potential parameters for water molecules, previously used for all friction calculations, were adopted from the OPLS-AA force field included in the software ($\sigma_{oxygen} = 0.31668$ nm and $\epsilon_{oxygen} = 0.8822$ k J/mol). Parameterization of the Lennard-Jones interactions for sodium and chloride in combination with the force field has been developed by M. Patra and M. Karttunen and applied in our simulations ($\sigma_{Cl} = 0.4417$ nm, $\epsilon_{Cl} = 0.4929$ k J/mol and $\sigma_{Na} = 0.333$ nm and $\epsilon_{Na} = 0.0117$ k J/mol). Furthermore, the mean values of σ and ϵ were taken for ion-water interactions ($\sigma_{O-Na} = 0.3242$ nm, and $\epsilon_{O-Na} = 0.0.0866$ k J/mol, $\sigma_{O-Cl} = 0.3785$ nm and $\epsilon_{O-Cl} = 0.5653$ k J/mol, $\sigma_{Na-Cl} = 0.3874$ nm and $\epsilon_{Na-Cl} = 0.0757$ k J/mol).

6.2 Friction simulations

Firstly, the surface premelting of an ice-NaCl system was studied and compared with previously simulated pure ice premelting Fig. 6.1.

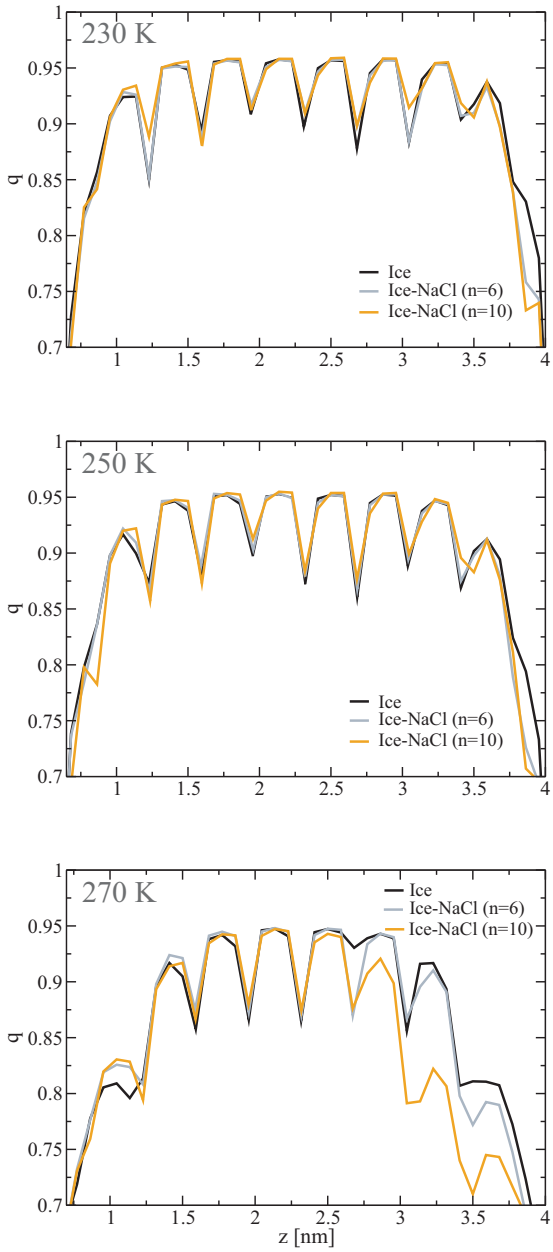

Figure 6.1. Comparison between the order parameters calculated for pure ice and with different ion concentrations (n) at temperatures 230 K, 250 K and 270 K.

Analyses were carried out within the same temperature range of 230 - 270 K as previously and two different concentrations of Na^+ and Cl^- ions placed at the same surface. As illustrated in Fig. 6.1 a noticeable difference in the surface ordering is seen only at higher impurity concentrations and at around the melting temperature. This explains similarities in calculated frictional forces for each system Fig. 6.2.

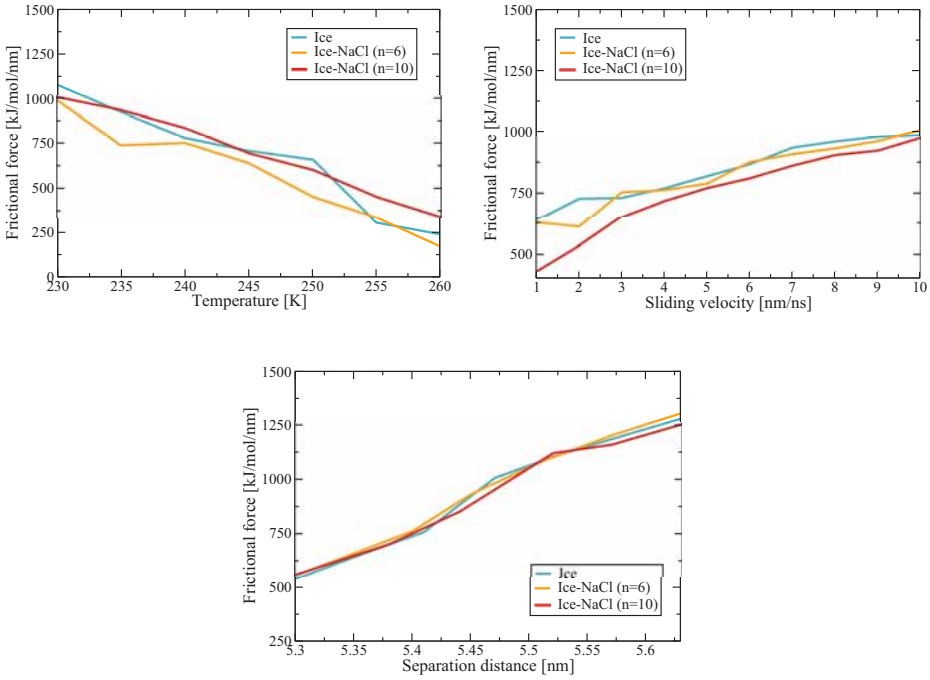

Figure 6.2. Frictional force as a function of temperature, sliding velocity and load (separation distance) for pure ice and ice with different impurity ion concentrations.

Next we studied the effect of ion distribution on the surface premelting, namely Na^+ and Cl^- ions were placed at the opposite surfaces of an ice crystal (see Fig. 6.3 (b)). A phase transition between liquid and solid states of water under applied electric field has been seen in a number of computational and experimental studies. Mainly, crystallization of water confined between two parallel plates due to electric field induced realignment of the dipoles of water molecules has been reported [186, 189–191], however recent studies showed that an electric field can be responsible for the reversed process (ice melting) as well [192].

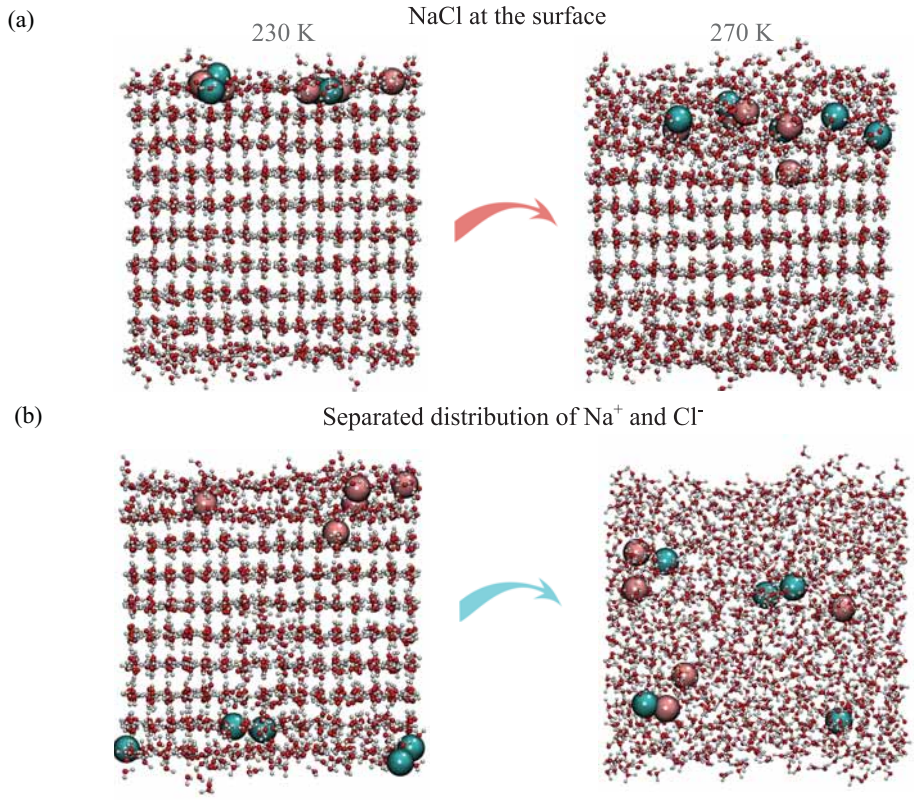

Figure 6.3. Surface premelting for different ion distributions for simulation time of 9 ns. (a) Ions distributed at the upper surface of ice and (b) Cl^- distributed at the upper surface and Na^+ at the lower surface of ice. Number of sodium and chloride is the same in both cases.

Comparisons made between the order parameters calculated for each system and at different temperatures demonstrate that such a separated distribution of the ions indeed lowers the melting temperature of ice (see Fig. 6.4).

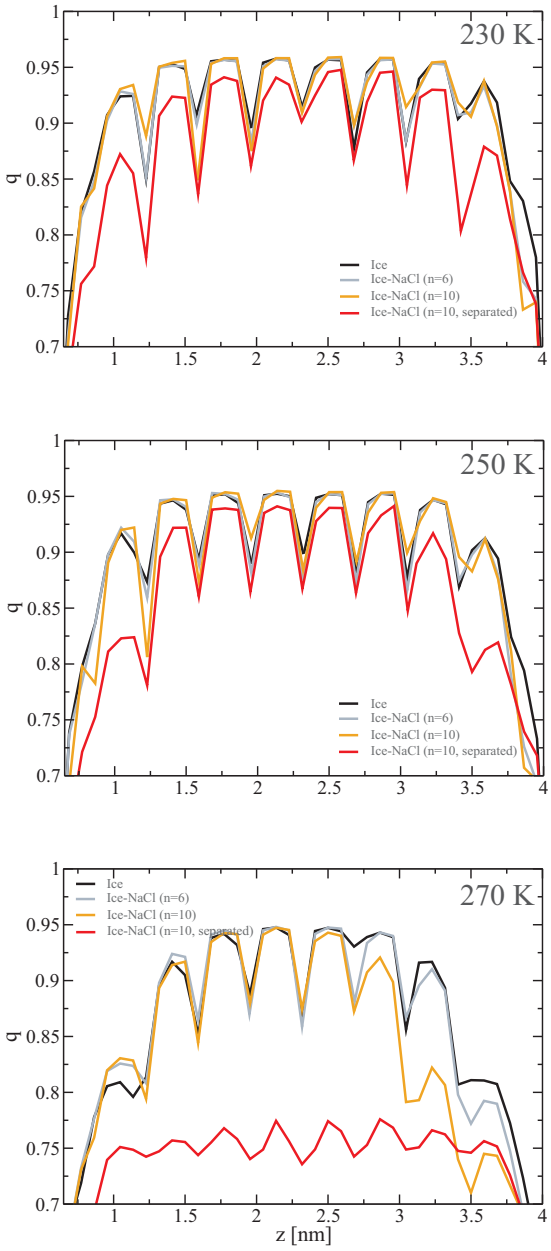

Figure 6.4. Order parameter for pure ice, ice with different ion concentrations and distributions at temperatures 230 K, 250 K and 270 K.

In order to check how fast the system undergoes a phase transition from solid to liquid state the order parameter after each nanosecond of the simulation was calculated. As can be seen in Fig. 6.5 the system reaches its final liquid phase quite fast, after 1 ns.

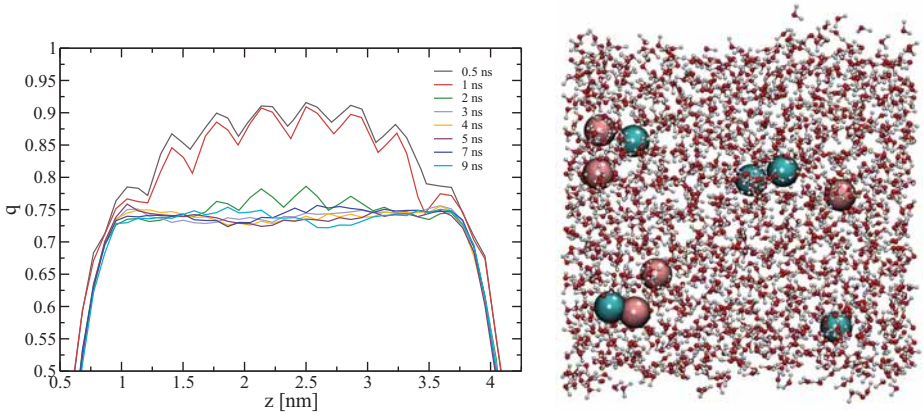

Figure 6.5. Progression of the surface premelting over simulation time of 9 ns for a system with separated ion distribution at 270 K.

The concept of electromelting (an electric field induced melting) was further examined by placing NaCl on both surfaces of ice to exclude the supposition that impurity concentration on both surfaces promotes melting rather than an electric field.

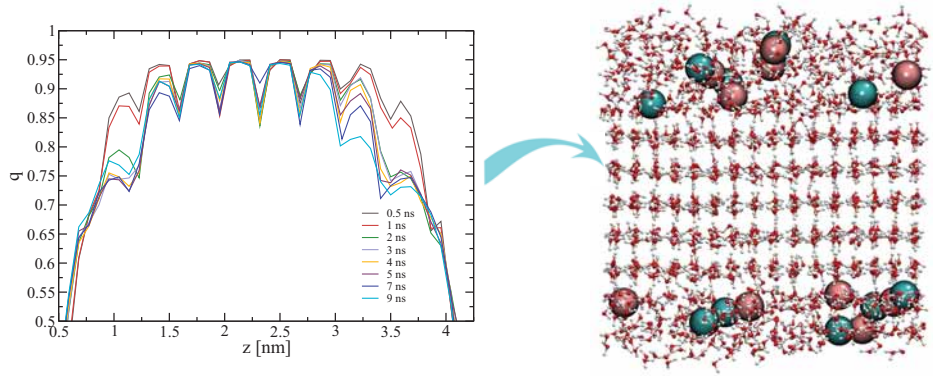

Figure 6.6. Progression of the surface premelting over simulation time of 9 ns for a system with equal concentration of Na^+ and Cl^- ion on both surfaces.

Similarly to the pure ice simulations, dynamics of the surface melting for contaminated ice remains stable after the first nanosecond of the simulation and no melting is seen at 270 K as illustrated in Fig. 6.6.

The long range interactions between positive and negative ions located at the opposite surfaces could also be responsible for melting of ice due to the interruption of the ordered hydrogen-bond network between water molecules. Therefore, at the same time the system with harmonically restrained surface ions was studied and compared with the behavior of the system without any restraints (Fig. 6.7).

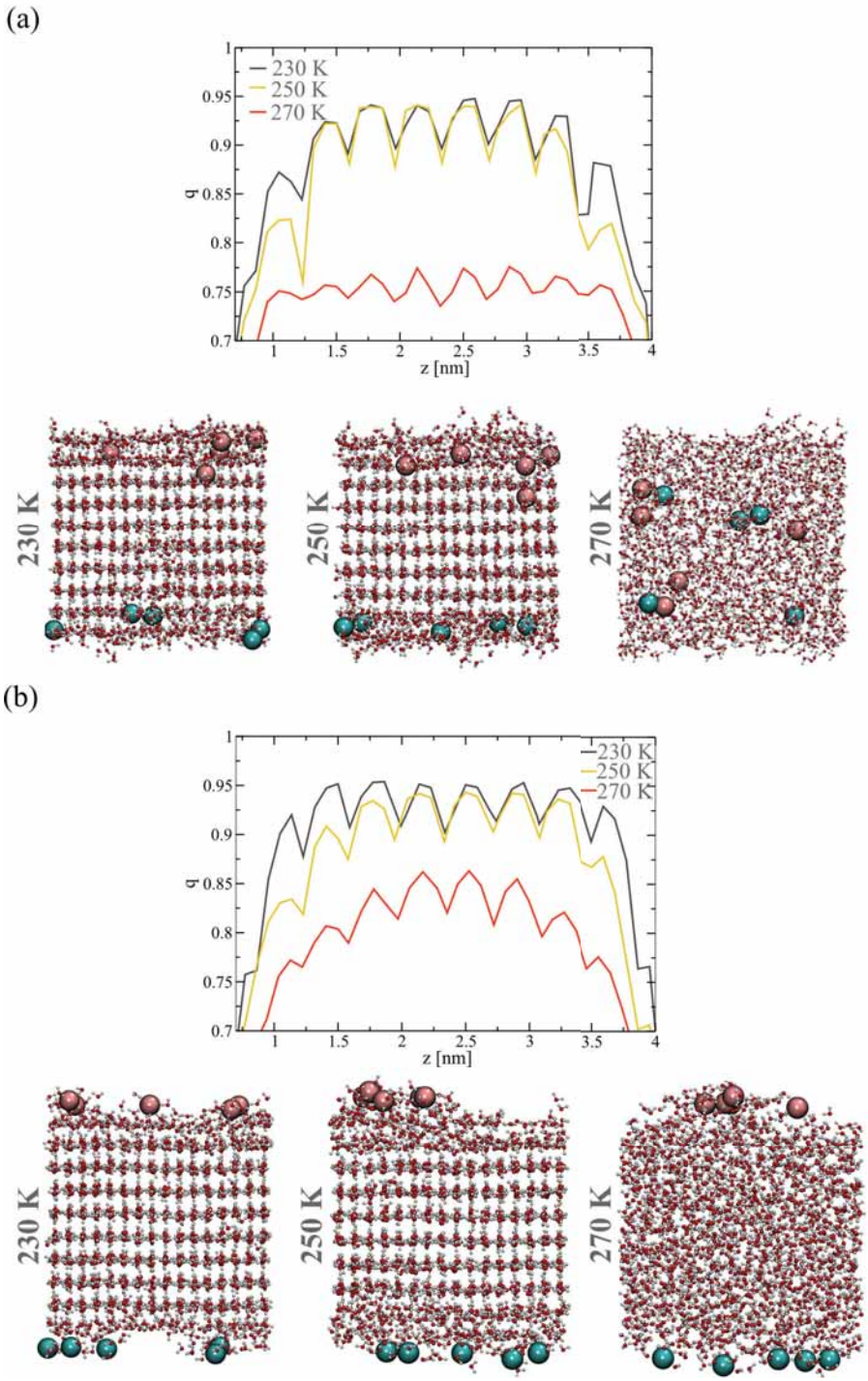

Figure 6.7. Surface premelting of contaminated ice system with free (a) and harmonically restrained ions (b).

Since the results are similar for free and restrained ions, melting due

to ion displacement throughout the system and resultant disruption of hydrogen-bond network can be eliminated. Furthermore, the ion concentration dependence on ice melting was studied (Fig. 6.6). As expected, the melting temperature decreases as the concentration of impurity increases. We chose the system of lowest concentration (n=10) of ions for further studies of friction to be able to use wide range of other affecting parameters such as temperature, sliding velocity and load.

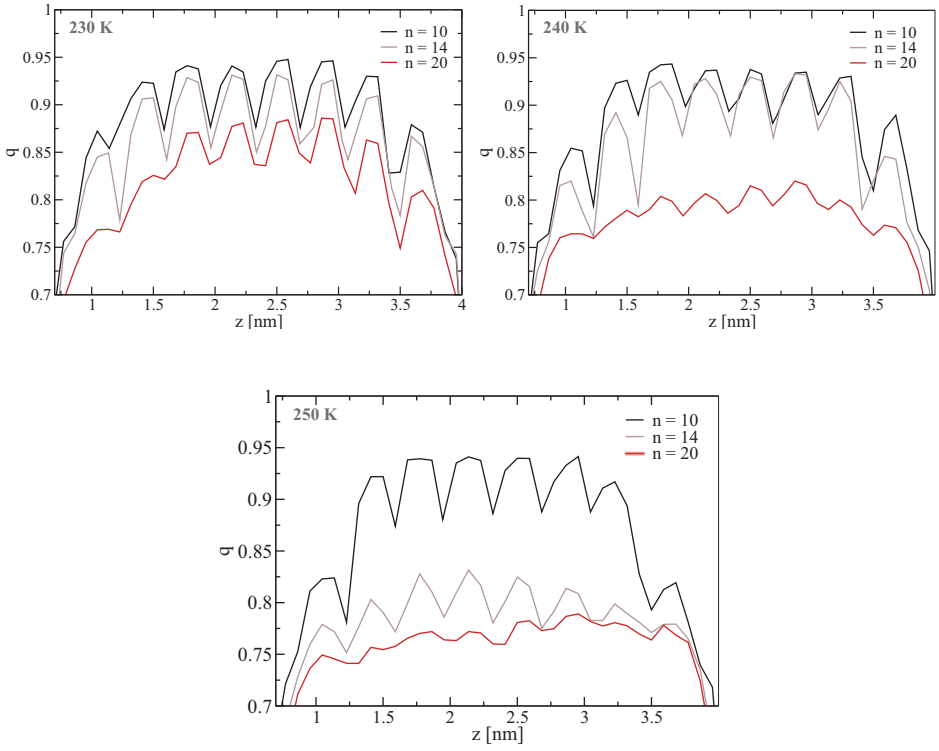

Figure 6.8. NaCl concentration dependence on the surface premelting of ice shown for 230K, 240K and 250K temperatures.

The frictional force for ice-NaCl system was calculated the same way as for the pure ice (see chapter 4.4). Figures 6.9, 6.10, and 6.11 show the frictional force as a function of temperature, sliding velocity and separation distance between harmonically restrained layers or in other words applied load for the pure and contaminated ice systems.

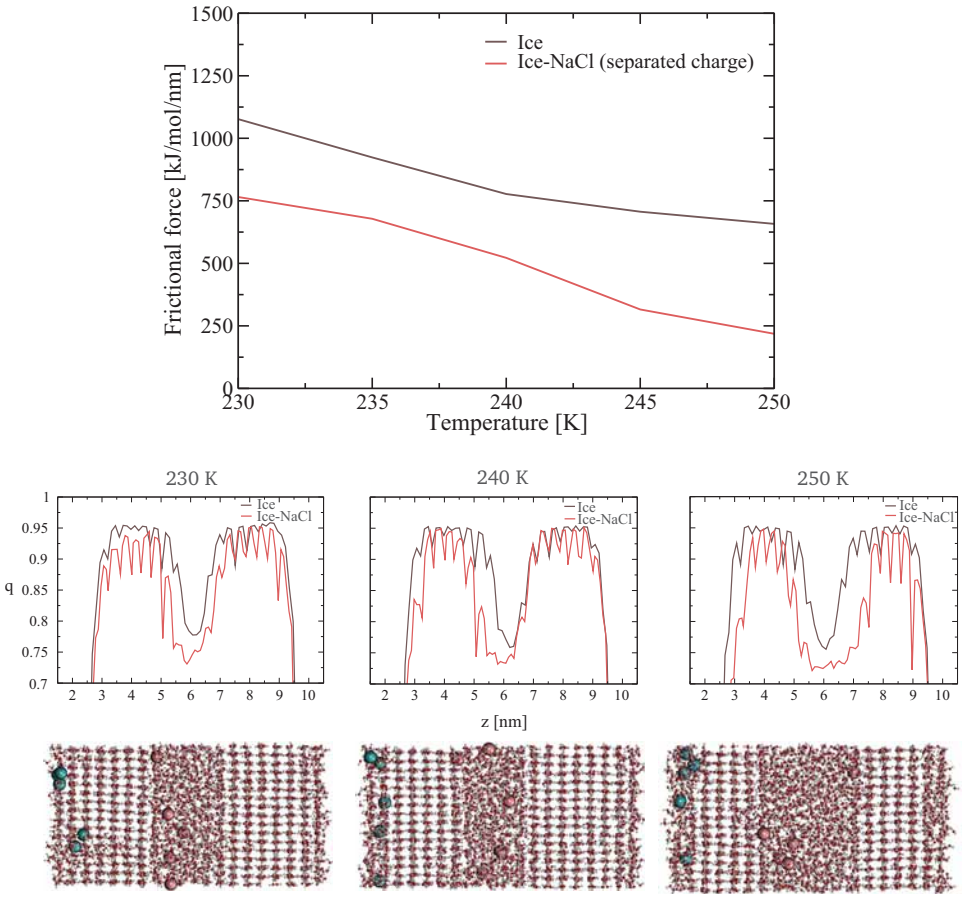

Figure 6.9. Frictional force as a function of temperature, at constant sliding velocity v=4 nm/ns, in repulsive load regime (separation distance 5.4 nm) for pure and contaminated (separated ion distribution) ices. Calculated order parameter perpendicular to the sliding direction at 230 K, 240 K, and 250 K for both systems. Snapshots are taken at the end of each simulation for the contaminated ice system.

Figure 6.9 shows the lower sliding friction for ice-NaCl system at all temperatures. This is due to the increased lubrication (indicated by the calculated order parameters at 230K, 240K, and 250K temperatures) of the interface when the ions are introduced in the system. Similar behavior is seen in calculated frictional force for different sliding velocities and separation distances (see Fig. 6.10 and Fig. 6.11).

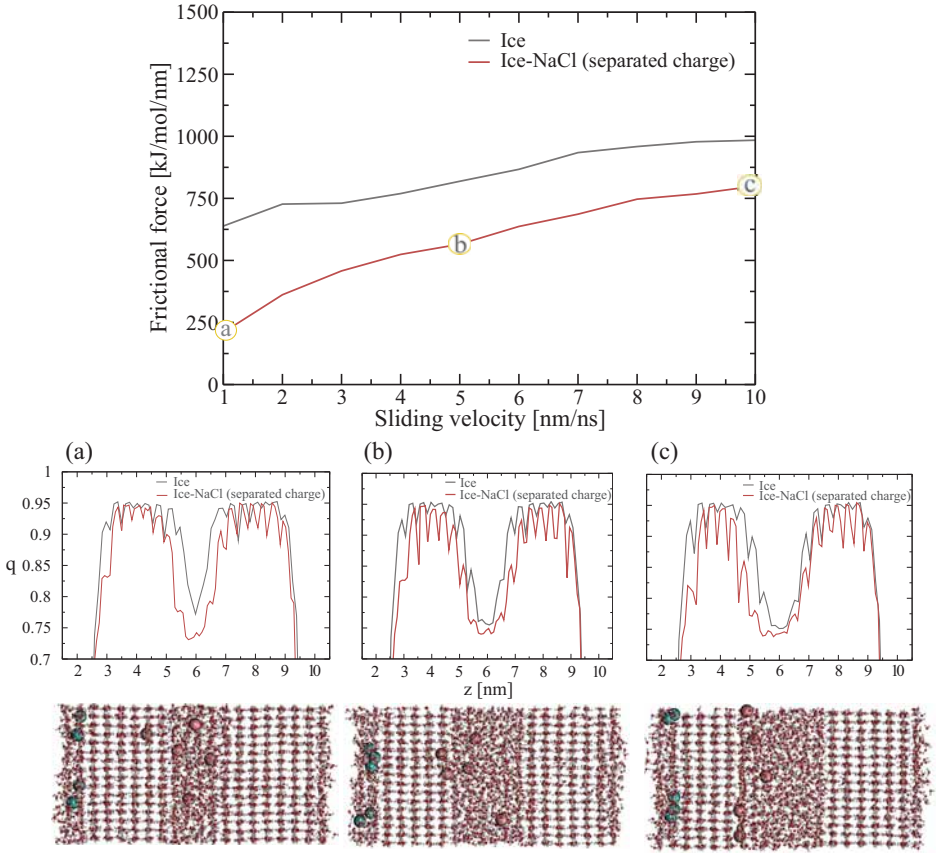

Figure 6.10. Velocity dependence of frictional force at 240 K, in repulsive load regime (separation distance 5.4 nm) for pure and contaminated (separated ion distribution) ices. Calculated order parameter perpendicular to the sliding direction for (a) v = 1 nm/ns, (b) v = 5 nm/ns, and (c) v = 10 nm/ns sliding velocities. Snapshots are taken at the end of each simulation for the contaminated ice system.

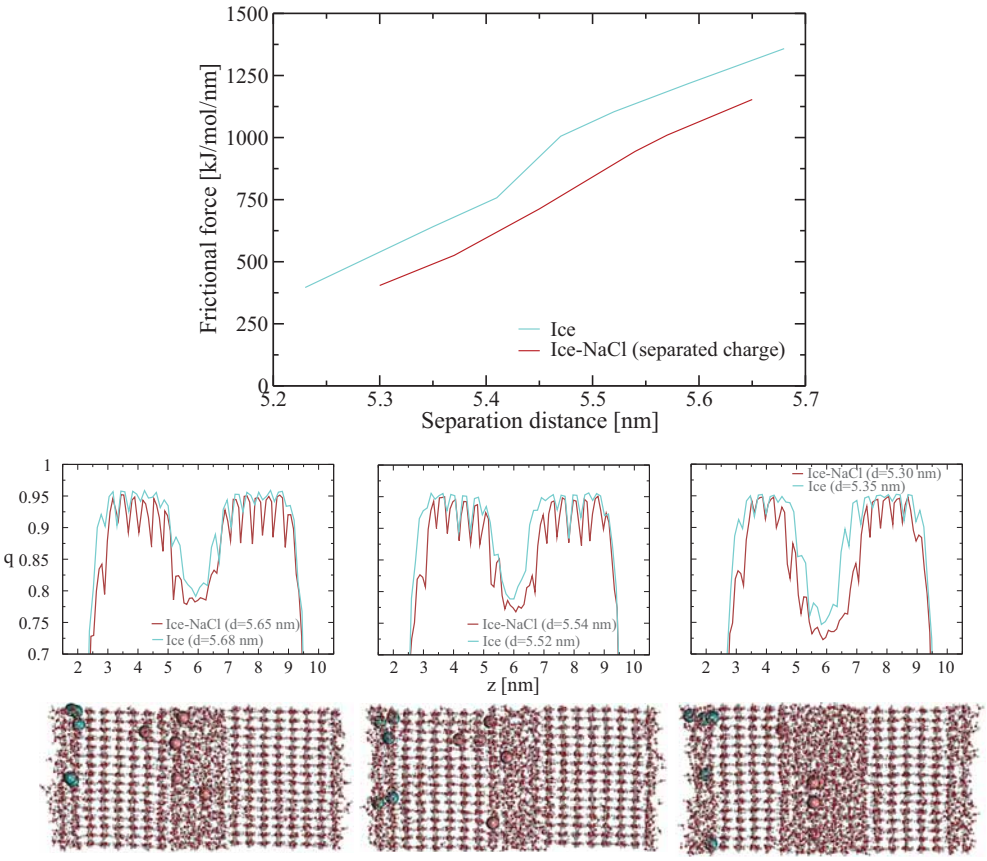

Figure 6.11. Frictional force dependence on separation between harmonically restrained layers at constant temperature of 240 K and 4 nm/ns sliding velocity for pure and contaminated (separated ion distribution) ices. Comparison between the order parameters for both systems calculated perpendicular to the sliding direction at different d separations. Snapshots are taken at the end of each simulation for the contaminated ice system.

Similar trends are shown in all cases, however the frictional force is always lower for contaminated ice than that for the pure system which can be explained by the strong influence of separated ion distribution on surface melting of ice.

7. Conclusions

Experimental studies have shown that generally friction on ice surfaces is influenced by temperature, sliding velocity and applied load [11, 14, 17, 18, 128]. However, when comparing the presented simulations to experiments, it should be noted that the simulated interfaces are atomistically smooth and always separated by the liquid premelt layer. This suggests we are simulating a hydrodynamic friction regime, where friction is due to viscous shear of the liquid film, corresponding to experiments done close to the melting point where thick premelt layers are expected.

Pure viscous shearing would imply a frictional force proportional to the sliding velocity. However, the simulations show there is also a temperature dependent static friction component - a minimum force needed to move the ice sheets at low velocities, making the premelt act more like a Bingham plastic [193] rather than a Newtonian liquid. Simulations were also carried out with a constant sliding force, chosen to be lower than the minimum force calculated from constant velocity simulations, verifying that a finite force is necessary to initiate sliding. This is explained by the tendency of the interface liquid layer to solidify between the ice sheets. The lower the temperature, the stronger the pulling force needs to be to prevent the system from freezing to a single piece of solid ice.

Experimentally, friction between ice surfaces decreases with increasing sliding velocity due to increased frictional heating and thicker liquid layer at the interface. However, close to the melting point, the coefficient of friction becomes proportional to $v^{\frac{1}{2}}$ [18] once the interface is completely covered in liquid and viscous shear becomes dominant. For temperatures close to the melting point our simulations show a similar dependence (the relative root mean square error and the correlation coefficient is 0.07 and 0.1, respectively) of the frictional force on sliding velocity. At low temperatures the difference between experimental and simulation results can be

understood to be due to the surface roughness present in experimental systems, missing from the simulations.

Ice friction experiments performed at the macroscopic scale show a decrease in the friction coefficient with increasing normal load, with a considerable difference between results depending on the material sliding over ice surface as well as temperature and velocity [11, 14, 15, 17, 18]. Similar trends are also seen in the simulations which also show a decrease in the frictional force with increasing load, although in all cases (regardless of temperature or sliding velocity) the dependence becomes less pronounced as the load increases.

The molecular dynamics simulations have been usually applied to studies of the properties of ice, such as cutting ice with a nanowire using the Mercedes-Benz model of water [194] or investigations of the surface premelting of ice using TIP-like models [3, 6, 8, 103]. However, its frictional properties have been mostly addressed experimentally. This work presents the study of the ice friction from a molecular dynamics approach. The ice friction model discussed in this research, as well as the findings, can be applied to many other tribology systems (e.g. ice-polymer, ice-metal). Furthermore, the effect of material properties like roughness, can be introduced in the system for investigating different friction regimes.

Bibliography

[1] M. Faraday. Experimental researches in chemistry and physics. *R. Taylor and W. Francis*, 1859.

[2] C. Gurney. Surface forces in liquids and solids. *Proceedings of the Physical Society. Section A*, 62(10):639, 1949.

[3] J. G. Dash, F. Haiying, and J. S. Wettlaufer. The premelting of ice and its environmental consequences. *Reports on Progress in Physics*, 58:115, 1995.

[4] R. Rosenberg. Why is ice slippery? *Physics Today*, 58(12):50, 2005.

[5] J. G. Dash, A. W. Rempel, and J. S. Wettleufer. The physics of premelted ice and its geophysical consequences. *Reviews of Modern Physics*, 78(3):695–741, 2006.

[6] T. Ikeda-Fukazawa and K. Kawamura. Molecular-dynamics studies of surface of ice ih. *Journal of Chemical Physics*, 120:1395, 2004.

[7] Y. Li and G. A. Somorjai. Surface premelting of ice. *The Journal of Physical Chemistry C*, 111:9631–9637, 2007.

[8] M. M. Conde, C. Vega, and A. Patrykiejew. The thickness of a liquid layer on the free surface of ice as obtained from computer simulation. *Journal of Chemical Physics*, 129:014702, 2008.

[9] C. L. Bishop, D. Pan, L. M. Liu, G. A. Tribello, A. Michaelides, E. G. Wang, and B. Slater. On thin ice: surface order and disorder during pre-melting. *Faraday Discussions*, 141:277–292, 2009.

[10] R. W. Carpick. Controlling friction. *Science*, 313(5784):184–185, Jul 2006.

[11] F. P. Bowden and T. P. Hughes. The mechanism of sliding on ice and snow. *Proceedings of the Royal Society A*, 172(280):280, 1939.

[12] H. Liang, J.M. Martin, and T.L. Mogne. Experimental investigation of friction on low-temperature ice. *Acta Materialia*, 51(9):2639 – 2646, 2003.

[13] H. Liang, J. M. Martin, and Th. Le Mogne. Friction-induced nonequilibrium phase transformation of low-temperature ice. *Journal of Applied Physics*, 97, Jan 2005.

[14] M. Akkok and S. J. Calabrese. Parameters affecting the kinetic friction of ice. *Journal of Tribology*, 109:552–561, 1987.

[15] L. Bäurle, U. Kaempfer, D. Szabo, and N. D. Spencer. Sliding friction of polyethylene on snow and ice: Contact area and modeling. *Cold Regions Science and Technology*, 47:276–289, 2007.

[16] L. Bäurle, D. Szabó, M. Fauve, H. Rhyner, and N.D. Spencer. Sliding friction of polyethylene on ice: tribometer measurements. *Tribology Letters*, 24:77–84, 2006.

[17] B. V. Derjaguin. Mechanical properties of the boundary lubrication layer. *Wear*, 128:19–27, 1988.

[18] P. Oksanen and J. Keinonen. The mechanism of friction of ice. *Wear*, 78:315–324, 1982.

[19] N. Maeno, M. Arakawa, A. Yasutome, N. Mizukami, and S. Kanazawa. Ice-ice friction measurements, and water lubrication and adhesion-shear mechanisms. *Canadian Journal of Physics*, 81(1-2):241–249, 2003.

[20] A.L. Fortt and E.M. Schulson. The resistance to sliding along coulombic shear faults in ice. *Acta Materialia*, 55(7):2253 – 2264, 2007.

[21] A. L. Fortt and E. M. Schulson. Frictional sliding across coulombic faults in first-year sea ice: A comparison with freshwater ice. *Journal of Geophysical Research: Oceans*, 116(C11), 2011.

[22] E. M. Schulson and A. L. Fortt. Friction of ice on ice. *Journal of Geophysical Research*, 117(B12):B12204, 2012.

[23] B. Lishman, P. Sammonds, and D. Feltham. A rate and state friction law for saline ice. *Journal of Geophysical Research: Oceans*, 116(C5), 2011.

[24] F. E. Kennedy, E. M. Schulson, and D. E. Jones. The friction of ice on ice at low sliding velocities. *Philosophical Magazine A*, 80(5):1093–1110, 2000.

[25] M. Beeman, W. B. Durham, and S. H. Kirby. Friction of ice. *Journal of Geophysical Research*, 93:7625–7633, Jul 1988.

[26] D. Dawson. History of tribology. *Professional Engeneering Publishing*, 2nd ed., 1998.

[27] F. P. Bowden and D. Tabor. The friction and lubrication of solids. *Oxford University Press Inc.*, 3rd ed., 2001.

[28] B. N. J. Persson. Sliding friction: Physical principles and applications. *Springer-Verlag*, 2nd ed., 2000.

[29] B. N. J. Persson. Sliding friction. *Surface Science*, 33:83–119, 1999.

[30] M. O. Robbins and M. H. Müser. Computer simulation of friction, lubrication and wear. *CRC Press, Boca Raton*, 2000.

[31] M. H. Müser, M. Urbakh, and M. O. Robbins. Statistical mechanics of static and low-velocity kinetic friction. *Advances in Chemical Physics*, 126:187–272, 2003.

[32] B. Bhushan, J. N. Israelachvili, and U. Landman. Nanotribology: friction, wear and lubrication at the atomic scale. *Nature*, 374:607–613, 1995.

[33] C. Zhang. Research on thin film lubrication: state of the art. *Tribology International*, 38(4):443 – 448, 2005.

[34] J. Krim. Friction at the nano-scale. *Physics World*, 18(2):31–34, 2005.

[35] J.N. Israelachvili and D. Tabor. The shear properties of molecular films. *Wear*, 24(3):386 – 390, 1973.

[36] J. N. Israelachvili, P. M. Mcguiggan, and A. M. Homola. Dynamic properties of molecularly thin liquid-films. *Science*, 240:189–191, 1988.

[37] J. Van Alsten and S. Granick. Molecular tribometry of ultrathin liquid films. *Physical Review Letters*, 61:2570–2573, 1988.

[38] J. Peachey, J. Van Alsten, and S. Granick. Design of an apparatus to measure the shear response of ultrathin liquid films. *Review of Scientific Instruments*, 62:463, 1991.

[39] S. Granick. Motions and relaxations of confined liquids. *Science*, 253:1374–1379, 1991.

[40] J. Krim and A. Widom. Damping of a crystal oscillator by an adsorbed monolayer and its relation to interfacial viscosity. *Physical Review B*, 38:12184–12189, 1988.

[41] E. Rabinowicz. Friction and wear of materials. *Wiley, New York*, 2nd ed., 1965.

[42] F. Heslot, T. Baumberger, B. Perrin, B. Caroli, and C. Caroli. Creep, stick-slip, and dry-friction dynamics: Experiments and a heuristic model. *Physical Review E*, 49:4973–4988, 1994.

[43] B. Bhushan. Introduction to tribology. *Wiley and Sons, New York*, 2002.

[44] C. M. Mate. Tribology on the small scale, a bottom up approach to friction, lubrication and wear. *Oxford University Press*, 2008.

[45] O.K. Dudko, A.E. Filippov, J. Klafter, and M. Urbakh. Dynamic force spectroscopy: a fokker–planck approach. *Chemical Physics Letters*, 352(5–6):499 – 504, 2002.

[46] O. M. Braun and A. G. Naumovets. Nanotribology: Microscopic mechanisms of friction. *Surface Science Reports*, 60:79–158, 2006.

[47] Y. Sang, M. Dubé, and M. Grant. Dependence of friction on roughness, velocity, and temperature. *Physical Review E*, 77:036123, 2008.

[48] J. Krim. Surface science and the atomic-scale origins of friction: what once was old is new again. *Surface Science*, 500:741–758, 2002.

[49] A. Vanossi and O. M. Braun. Driven dynamics of simplified tribological models. *Journal of Physics: Condensed Matter*, 19(30):305017, 2007.

[50] O. M. Braun and Y. S. Kivshar. Nonlinear dynamics of the frenkel–kontorova model. *Physics Reports*, 306(1–2):1 – 108, 1998.

[51] O. M. Braun and Y. S. Kivshar. The frenkel-kontorova model: Concepts, methods, and applications. *Springer-Verlag, Berlin*, 2004.

[52] G. A. Tomlinson. A molecular theory of friction. *Philosophical Magazine*, 7:905–939, 1929.

[53] A. Vanossi, N. Manini, M. Urbakh, S. Zapperi, and E. Tosatti. Colloquium: Modeling friction: From nanoscale to mesoscale. *Reviews of Modern Physics*, 85:529–552, 2013.

[54] T. Ala-Nissila, R. Ferrando, and S. C. Ying. Collective and single particle diffusion on surfaces. *Advances in Physics*, 51:949–1078, 2002.

[55] J. A. Greenwood. Adhesion of elastic spheres. *Proceedings of the Royal Society London A*, 453:1277, 1997.

[56] I. Szlufarska, M. Chandross, and R. W. Carpick. Recent advances in single-asperity nanotribology. *Journal of Physics D: Applied Physics*, 41:123001, 2008.

[57] L. Wenning and M. H. Müser. Friction laws for elastic nanoscale contacts. *Europhysics Letters*, 54:693–699, 2001.

[58] G. Gao, R. J. Cannara, R. W. Carpick, and J. A. Harrison. Atomic-scale friction on diamond: A comparison of different sliding directions on (001) and (111) surfaces using md and afm. *Langmuir*, 23:5394–5404, 2007.

[59] Y. Mo, K. T. Turner, and I. Szlufarska. Friction laws at the nanoscale. *Nature*, 457:1116–1119, 2009.

[60] N. S. Tambe and B. Bhushan. Nanoscale friction and wear maps. *Philosophical Transactions of the Royal Society A*, 366:1405–1424, 2008.

[61] J. A. Nieminen, A. P. Sutton, and J. B. Pethica. Static junction growth during frictional sliding on metals. *Acta Metallurgica et Materialia*, 40:2503–2509, 1992.

[62] M. R. Sorensen, K. W. Jacobsen, and P. Stoltze. Simulations of atomic-scale sliding friction. *Physical Review B*, 53:2101–2113, 1996.

[63] E. Gnecco, R. Bennewitz, and E. Meyer. Abrasive wear on the atomic scale. *Physical Review Letters*, 88:215501, 2002.

[64] G. Bussi, D. Donadio, and M. Parrinello. Canonical sampling through velocity-rescaling. *Journal of Chemical Physics*, 126:014101, 2007.

[65] S. Nose. A molecular dynamics method for simulations in the canonical ensemble. *Molecular Physics*, 52:255–268, 1984.

[66] D. Frenkel and B. Smit. Understanding molecular simulation, from algorithms to applications. *Academic Press, USA*, 1996.

[67] A. Benassi, A. Vanossi, G. E. Santoro, and E. Tosatti. Parameter-free dissipation in simulated sliding friction. *Physical Review B*, 82:081401, 2010.

[68] R. Guerra, U. Tartaglino, A. Vanossi, and E. Tosatti. Ballistic nanofriction. *Nature Materials*, 9:634–637, 2010.

[69] D. Eisenberg and W. Kauzmann. The structure and properties of water. *Oxford University Press*, 1969.

[70] J. L. Finney. The water molecules and its interactions: the interaction between theory, modeling and experiment. *Journal of Molecular Liquids*, 90:303–312, 2001.

[71] J. L. Finney. Water? what's so special about it? *Philosophical Transactions of the Royal Society B*, 359:1145, 2004.

[72] R. C. Dougherty. Temperature and pressure dependence of hydrogen bond strength: A perturbation molecular orbital approach. *Journal of Chemical Physics*, 109:7372, 1998.

[73] G. Malenkov. Liquid water and ices: understanding the structure and physical properties. *Journal of Physics: Condensed Matter*, 21:283101, 2009.

[74] P. V. Hobbs. Ice physics. *Oxford: Clarendon*, 1974.

[75] V. F. Petrenko and R. W. Whitworth. Physics of ice. *Oxford University Press*, 2002.

[76] T. Rausch, V. Bergeron, J. H. E. Cartwright, R. Escribano, J. L. Finney, H. Grothe, P. J. Gutierrez, J. Haapala, W. F. Kuhs, J. B. C. Pettersson, S. D. Price, C. I. Diaz, D. J. Stokes, G. Strazzulla, E. S. Thomson, H. Trinks, and N. Aytemiz. Ice structures, patterns, and processes: A view across the ice fields. *Reviews of Modern Physics*, 84:885–944, 2012.

[77] J. D. Bernal and R. H. Fowler. A theory of water and ionic solution, with particular reference to hydrogen and hydroxyl ions. *Journal of Chemical Physics*, 1:515, 1933.

[78] L. Pauling. The structure and entropy of ice and of other crystals with some randomness of atomic arrangement. *Journal of the American Chemical Society*, 57(12):2680–2684, 1935.

[79] N. Bjerrum. Structure and properties of ice. *Science*, 115(2989):385–390, 1952.

[80] R. Podeszwa and V. Buch. Structure and dynamics of orientational defects in ice. *Physical Review Letters*, 83:4570–4573, 1999.

[81] C. Lobban, J. L. Finney, and W. F. Kuhs. The structure and ordering of ices iii and v. *Journal of Chemical Physics*, 112:7169, 2000.

[82] J. W. M. Frenken and J. F. van der Veen. Observation of surface melting. *Physical Review Letters*, 54:134–137, 1985.

[83] D. J. Shu, D. Y. Sun, X. G. Gong, and W. M. Lau. A molecular-dynamics study of the anisotropic surface-melting properties of al(110). *Surface Science*, 441(1):206–212, 1999.

[84] B. Pluis, van der Gon, A. W. Denier, J. W. M. Frenken, and J. F. van der Veen. Crystal-face dependence of surface melting. *Physical Review Letters*, 59:2678–2681, 1987.

[85] H. Häkkinen and M. Manninen. Computer simulation of disordering and premelting of low-index faces of copper. *Physical Review B*, 46:1725–1742, 1992.

[86] P. H. Fuoss, L. J. Norton, and S. Brennan. X-ray scattering studies of the melting of lead surfaces. *Physical Review Letters*, 60:2046–2049, 1988.

[87] K. C. Prince, U. Breuer, and H. P. Bonzel. Anisotropy of the order-disorder phase transition on the pb(110) surface. *Physical Review Letters*, 60:1146–1149, 1988.

[88] J. Krim, J. P. Coulomb, and J. Bouzidi. Triple-point wetting and surface melting of oxygen films adsorbed on graphite. *Physical Review Letters*, 58:583–586, 1987.

[89] J. W. M. Frenken, J. P. Toennies, and Ch. Wöll. Self-diffusion at a melting surface observed by he scattering. *Physical Review Letters*, 60:1727–1730, 1988.

[90] H. Hakkinen and U. Landman. Superheating, melting, and annealing of copper surfaces. *Physical Review Letters*, 71:1023–1026, 1993.

[91] S.Valkealahti and R. M. Nieminen. Molecular dynamics investigation of the premelting effects of lennard-jones (111) surfaces. *Physica Scripta*, 36:646, 1987.

[92] P. Carnevali, F. Ercolessi, and E. Tosatti. Melting and nonmelting behavior of the au(111) surface. *Physical Review B*, 36:6701–6704, 1987.

[93] S. Nie, N. C. Bartelt, and K. Thürmer. Observation of surface self-diffusion on ice. *Physical Review Letters*, 102:136101, 2009.

[94] B. Pittenger, S. C. Fain, M. J. Cochran, J. M. K. Donev, B. E. Robertson, A. Szuchmacher, and R. M. Overney. Premelting at ice-solid interfaces studied via velocity-dependent indentation with force microscope tips. *Physical Review B*, 63:134102, 2001.

[95] A. Döppenschmidt and H. Butt. Measuring the thickness of the liquid-like layer on ice surfaces with atomic force microscopy. *Langmuir*, 16(16):6709, 2000.

[96] A. Döppenschmidt, M. Kappl, and H. Butt. Surface properties of ice studied by atomic force microscopy. *Journal of Physical Chemistry B*, 102:7813, 1998.

[97] V. I. Kvlividze, V. F. Kiselec, A. B. Kurzaev, and L. A. Ushakova. The mobile water phase on ice surfaces. *Surface Science*, 44:60–68, 1974.

[98] H. Dosch, A. Lied, and J. H. Bilgram. Disruption of the hydrogen-bonding network at the surface of ih ice near surface premelting. *Surface Science*, 366:43–50, 1996.

[99] H. Bluhm, D. F. Ogletree, C. S. Fadley, Z. Hussain, and M. Salmeron. The premelting of ice studied with photoelectron spectroscopy. *Journal of Physics: Condensed Matter*, 14:L227, 2002.

[100] L. Makkonen. Surface melting of ice. *Journal of Chemical Physics B*, 101:6196–6200, 1997.

[101] X. Wei, P. B. Miranda, and Y. R. Shen. Surface vibrational spectroscopic study of surface melting of ice. *Physical Review Letters*, 86:1554–1557, 2001.

[102] X. Wei, P. B. Miranda, C. Zhang, and Y. R. Shen. Sum-frequency spectroscopic studies of ice interfaces. *Physical Review B*, 66:085401, 2002.

[103] R. G. Pereyra and M. A. Carignano. Ice nanocolumns: A molecular dynamics study. *The Journal of Physical Chemistry C*, 113:12699–12705, 2009.

[104] J. R. Marko and R. E. Thomson. Rectilinear leads and internal motions in the ice pack of the western arctic ocean. *Journal of Geophysical Research*, 82(6):979–987, January 1977.

[105] W. D. Hibler III and E. M. Schulson. On modeling the anisotropic failure and flow of flawed sea ice. *Journal of Geophysical Research*, 105(C7):17105–17120, 2000.

[106] M. A. Hopkins, S. Frankenstein, and A. S. Thorndike. Formation of an aggregate scale in arctic sea ice. *Journal of Geophysical Research*, 109(C1):C01032, 2004.

[107] E. M. Schulson. Compressive shear faults within arctic sea ice: Fracture on scales large and small. *Journal of Geophysical Research*, 109(C7):C07016, 2004.

[108] M. A. Hopkins and A. S. Thorndike. Floe formation in arctic sea ice. *Journal of Geophysical Research*, 111(C11):C11S23, 2006.

[109] D. L. Sulsky L. B. Munday M. D. Coon Schreyer, H. L. and R. Kwok. Elastic-decohesive constitutive model for sea ice. *Journal of Geophysical Research*, 111(C11):C11S26, 2006.

[110] J. Weiss, E. M. Schulson, and H. L. Sternc. Sea ice rheology from in-situ, satellite and laboratory observations: Fracture and friction. *Earth and Planetary Science Letters*, 255(1-2):1–8, 2007.

[111] D. L. Feltham. Sea ice rheology. *Annual Review of Fluid Mechanics*, 40:91–112, 2008.

[112] J. Weiss and E. M Schulson. Coulombic faulting from the grain scale to the geophysical scale: lessons from ice. *Journal of Applied Physics D*, 42(21), 2009.

[113] A. V. Wilchinsky, D. L. Feltham, and M. A. Hopkins. Effect of shear rupture on aggregate scale formation in sea ice. *Journal of Geophysical Research*, 115(C10), 2010.

[114] A. V. Wilchinsky and D. L. Feltham. Modeling coulombic failure of sea ice with leads. *Journal of Geophysical Research*, 116(C8), 2011.

[115] E. M Schulson. The brittle compressive fracture of ice. *Acta Metallurgica et Materialia*, 38(10):1963 – 1976, 1990.

[116] E. M. Schulson. Brittle failure of ice. *Engineering Fracture Mechanics*, 68(17–18):1839 – 1887, 2001.

[117] B.R. Tufts, R. Greenberg, G. Hoppa, and P. Geissler. Astypalaea linea: A large-scale strike-slip fault on europa. *Icarus*, 141(1):53 – 64, 1999.

[118] A. J. Dombard and W. B. McKinnon. Formation of grooved terrain on ganymede: Extensional instability mediated by cold, superplastic creep. *Icarus*, 154(2):321 – 336, 2001.

[119] F. Nimmo and E. Gaidos. Strike-slip motion and double ridge formation on europa. *Journal of Geophysical Research: Planets*, 107(E4):5–1–5–8, 2002.

[120] S. A. Kattenhorn. Strike-slip fault evolution on europa: evidence from tailcrack geometries. *Icarus*, 172(2):582 – 602, 2004.

[121] L. M. Prockter, F. Nimmo, and R. T. Pappalardo. A shear heating origin for ridges on triton. *Geophysical Research Letters*, 32(L14202), 2005.

[122] A. J. Dombard and W. B. McKinnon. Folding of europa's icy lithosphere: an analysis of viscous-plastic buckling and subsequent topographic relaxation. *Journal of Structural Geology*, 28(12):2259 – 2269, 2006.

[123] F. Nimmo, J. R. Spencer, R. T. Pappalardo, and M. E. Mullen. Shear heating as the origin of the plumes and heat flux on enceladus. *Nature*, 447:289–291, 2007.

[124] B. Smith-Konter and R. T. Pappalardo. Tidally driven stress accumulation and shear failure of enceladus's tiger stripes. *Icarus*, 198(2):435 – 451, 2008.

[125] J. G. Olgin, B. R. Smith-Konter, and R. T. Pappalardo. Limits of enceladus's ice shell thickness from tidally driven tiger stripe shear failure. *Geophysical Research Letters*, 38(2), 2011.

[126] A. M. Kietzig, S. G. Hatzikiriakos, and P. Englezos. Physics of ice friction. *Journal of Applied Physics*, 107:081101, 2010.

[127] S. J. Calabrese. Frictional characteristics of materials sliding against ice. *Lubrication Engineering*, 36:283–289, 1980.

[128] D. C. B. Evans, J. F. Nye, and K. J. Cheeseman. The kinetic friction of ice. *Proceedings of the Royal Society A*, 347:493–512, 1976.

[129] D. D. Higgins, B. A. Marmo, C. E. Jeffree, V. Koutsos, and J. R. Blackford. Morphology of ice wear from rubber–ice friction tests and its dependence on temperature and sliding velocity. *Wear*, 265(5–6):634 – 644, 2008.

[130] A.D. Roberts and J.C. Richardson. Interface study of rubber-ice friction. *Wear*, 67(1):55 – 69, 1981.

[131] B. A. Marmo, J. R. Blackford, and C. E. Jeffree. Ice friction, wear features and their dependence on sliding velocity and temperature. *Journal of Glaciology*, 51(174):391–398, 2005.

[132] J. M. Thijssen. Computational physics. *Cambridge University Press*, 2nd ed., 2007.

[133] H. Goldstein, C. P. Poole, and J. L. Safko. Classical mechanics. *Pearse Educational International, USA*, 3rd ed., 2002.

[134] D. C. Rapaport. The art of molecular dynamics simulation. *Cambridge University Press*, 1996.

[135] R. McWeeny. Methods of molecular quantum mechanics. *New York Academy Press*, 3rd ed., 1989.

[136] A. Szabo and N. S. Ostlund. Modern quantum chemistry. *London, Macmillan*, 1982.

[137] M. E. Tuckerman and G. J. Martyna. Understanding modern molecular dynamics: Techniques and applications. *Journal of Physical Chemistry B*, 104:159–178, 2000.

[138] L. Verlet. Computer "experiments" on classical fluids. i. thermodynamical properties of lennard-jones molecules. *Physical Review*, 159:98–103, 1967.

[139] W. C. Swope, H. C. Andersen, P. H. Berens, and K. R. Wilson. A computer simulation method for the calculation of equilibrium constants for the formation of physical clusters of molecules: Application to small water clusters. *Journal of Chemical Physics*, 76, 1982.

[140] D. Chandler. Introduction to modern statistical mechanics. *Oxford University Press*, 1987.

[141] C. Hermann. Statistical physics, including applications to condensed matter. *Springer*, 2005.

[142] J. N. Israelachvili. Intermolecular and surface forces. *Academic Press, USA*, 3rd ed., 2011.

[143] K. A. Dill, T. M. Truskett, V. Vlachy, and B. Hribar-Lee. Modeling water, the hydrophobic effect, and ion solvation. *Annual Review of Biophysics and Biomolecular Structure*, 34:173, 2005.

[144] I. Nezbeda. Simple molecular models of water and their application. *Journal of Molecular Liquids*, 73:317–336, 1997.

[145] K. A. T. Silverstein, A. D. J. Haymet, and K. A. Dill. A simple model of water and the hydrophobic effect. *Journal of the American Chemical Society*, 120:3166–3175, 1998.

[146] T. Urbic, V. Vlachy, Yu. V. Kalyuzhnyi, N. T. Southall, and K. A. Dill. A two-dimensional model of water: Theory and computer simulations. *Journal of Chemical Physics*, 112:2843, 2000.

[147] T. M. Truskett and K. A. Dill. A simple statistical mechanical model of water. *The Journal of Physical Chemistry B*, 106(45):11829–11842, 2002.

[148] B. Hribar, N. T. Southall, V. Vlachy, and K. A. Dill. How ions affect the structure of water. *Journal of the American Chemical Society*, 124(41):12302–12311, 2002.

[149] A. Bizjak, T. Urbic, V. Vlachy, and K. A. Dill. Theory of three-dimensional mercedes-benz model of water. *Journal of Chemical Physics*, 131:194504, 2009.

[150] C. L. Dias, T. Ala-Nissila, M. Grant, and M. Karttunen. Three-dimensional “mercedes-benz” model for water. *Journal of Chemical Physics*, 131:054505, 2009.

[151] T. Hynninen, C. L. Dias, A.Mkrtchyan, V. Heinonen, M. Karttunen, A. S. Foster, and T. Ala-Nissila. A molecular dynamics implementation of the 3d mercedes-benz water model. *Computer Physics Communications*, 183:363–369, 2012.

[152] J. Leszczynski. Handbook of computational chemistry. *Springer*, 2012.

[153] M. P. Allen and D. J. Tildesley. Computer simulations of liquids. *Oxford University Press*, 1991.

[154] H. J. C. Berendsen, J. P. M. Postma, W. F. van Gunsteren, A. DiNola, and J. R. Haak. Molecular dynamics with coupling to an external bath. *Journal of Chemical Physics*, 81:3684, 1984.

[155] W. L. Jorgensen, J. Chandrasekhar, J. D. Madura, R. W. Impey, and M. L. Klein. Comparison of simple potential functions for simulating liquid water. *Journal of Chemical Physics*, 79:926, 1983.

[156] E. Sanz, C. Vega, J. L. F. Abascal, and L. G. MacDowell. Tracing the phase diagram of the four-site water potential (tip4p). *Journal of Chemical Physics*, 121:1165, 2004.

[157] E. Sanz, C. Vega, J.L. Abascal, and L.G. MacDowell. Phase diagram of water from computer simulation. *Physical Review Letters*, 92:255701, 2004.

[158] H. J. C. Berendsen, J. P. M. Postma, W. F. Van Gunsteren, and J. Hermans. Interaction models for water in relation to protein hydration. *The Jerusalem Symposia on Quantum Chemistry and Biochemistry*, 1981.

[159] F. H. Stillinger and A. Rahman. Improved simulation of liquid water by molecular dynamics. *Journal of Chemical Physics*, 60:1545, 1973.

[160] C. Vega, J. L. F. Abascal, M. M. Conde, and J. L. Aragones. What ice can teach us about water interactions: a critical comparison of the performance of different water models. *Faraday Discussions*, 141:251–276, 2009.

[161] H. W Horn, W.C. Swope, J. W. Pitera, J. D. Madura, T. J. Dick, G. L. Hura, and T. Head-Gordon. Development of an improved four-site water model for biomolecular simulations: Tip4p-ew. *Journal of Chemical Physics*, 120:9665–9678, 2004.

[162] C. Vega, J. L. F. Abascal, and I. Nezbeda. Vapor-liquid equilibria from the triple point up to the critical point for the new generation of tip4p-like models: Tip4p/ew, tip4p/2005, and tip4p/ice. *Journal of Chemical Physics*, 125:034503, May 2006.

[163] J. L. F. Abascal and C. Vega. A general purpose model for the condensed phases of water: Tip4p/2005. *Journal of Chemical Physics*, 123:234505, 2005.

[164] J. L. F. Abascal, E. Sanz, R. Garcia Fernandez, and C. Vega. A potential model for the study of ices and amorphous water: Tip4p/ice. *Journal of Physical Chemistry*, 122:234511, 2005.

[165] S. Picaud. Dynamics of tip5p and tip4p/ice potentials. *Journal of Chemical Physics*, 125:174712, 2006.

[166] Y. Koyama, H. Tanaka, G. Gao, and X. C. Zeng. Melting points and thermal expansivities of proton-disordered hexagonal ice with several model potentials. *Journal of Chemical Physics*, 121:7926, 2004.

[167] D. van der Spoel, E. Lindahl, B. Hess, A. R. van Buuren, and P. J. Meulenhoff E. Apol, and A. L. T. M. Sijbers D. P. Tieleman, K. A. Feenstra, R. van Drunen, and H. J. C. Berendsen. Gromacs: Fast, flexible, and free. *Journal of Computational Chemistry*, 26:1701–1718, 2005.

[168] P. H. Hunenberger. Thermostat algorithms for molecular dynamics simulations. *Advances in Polymer Science*, 173:105–149, 2005.

[169] W. G. Hoover. Canonical dynamics: Equilibrium phase-space distributions. *Physical Review A*, 31:1695–1697, 1985.

[170] M. Parrinello and A. Rahman. Polymorphic transitions in single crystals: A new molecular dynamics method. *Journal of Applied Physics*, 52:7182, 1981.

[171] A. Y. Toukmaji and J. A. Board Jr. Ewald summation techniques in perspective: a survey. *Computer Physics Communications*, 95:73–92, 1996.

[172] T. Darden, D. York, and L. Pedersen. Particle mesh ewald: An n-log(n) method for ewald sums in large systems. *Journal of Chemical Physics*, 98:100089, 1993.

[173] B. Hess, H. Bekker, H. J. C. Berendsen, and J. G. E. M. Fraaije. A linear constraint solver for molecular simulations. *Journal of Computational Chemistry*, 18:1463–1472, 1997.

[174] N. Samadashvili, B. Reischl, T. Hynninen, T. Ala-Nissilä, and A. S. Foster. Atomistic simulations of friction at an ice-ice interface. *Friction*, 1:242–251, 2013.

[175] J. R. Errington and P. G. Debenedetti. Relationship between structural order and the anomalies of liquid water. *Nature*, 409:318–321, 2001.

[176] M. R. Sorensen, K. W. Jacobsen, and P. Stoltze. Simulations of atomic-scale sliding friction. *Physical Review B*, 53:2101–2113, June 1995.

[177] U. Landman, W. D. Luedtke, and E. M. Ringer. Atomistic mechanisms of adhesive contact formation and interfacial processes. *Wear*, 153:3–30, March 1992.

[178] J. A. Harrison, C. T. White, R. J. Colton, and D. W. Brenner. Molecular-dynamics simulations of atomic-scale friction of diamond surfaces. *Physical Review B*, 46:9700–9708, Oct 1992.

[179] J.A. Nieminen, A.P. Sutton, and J.B. Pethica. Static junction growth during frictional sliding of metals. *Acta Metallurgica et Materialia*, 40:2503–2509, 1992.

[180] M. Vargonen, Y. Yang, L. Huang, and Y. Shi. Molecular simulation of tip wear in a single asperity sliding contact. *Wear*, 307:150–154, 2013.

[181] B. Li, P.C. Clapp, J.A. Rifkin, and X.M. Zhang. Molecular dynamics calculation of heat dissipation during sliding friction. *International Journal of Heat and Mass Transfer*, 46:37–43, 2003.

[182] P. Spijker, G. Anciaux, and J. Molinari. Relations between roughness, temperature and dry sliding friction at the atomic scale. *Tribology International*, 59:222–229, 2013.

[183] I. M. Sivebaek, V. N. Samoilov, and B. N. J. Persson. Velocity dependence of friction of confined hydrocarbons. *Langmuir*, 26:8721–8728, 2010.

[184] I. M. Sivebaek, V. N. Samoilov, and B. N. J. Persson. Effective viscosity of confined hydrocarbons. *Physical Review Letters*, 108:036102, 2012.

[185] S. Yim, N. Sonwalkar, and N. Saka. Molecular dynamics simulation of boundary lubricated interfaces. *Journal of Computer-Aided Materials Design*, 6:69–80, 1999.

[186] Y. Hu, T. Ma, and H. Wang. Energy dissipation in atomic-scale friction. *Friction*, 1:24–40, 2013.

[187] J. S. Wettlaufer. Impurity effects in the premelting of ice. *Physical Review Letters*, 82:2516–2519, 1999.

[188] T. Ikeda-Fukazawa and K. kawamura. Effects of ions on dynamics of ice surface. *Chemical Physics Letters*, 417:561–565, 2006.

[189] I. M. Svishchev and P. G. Kusalik. Crystallization of liquid water in a molecular dynamics simulation. *Physical Review Letters*, 73:975–978, 1994.

[190] I. M. Svishchev and P. G. Kusalik. Electrofreezing of liquid water: A microscopic perspective. *Journal of the American Chemical Society*, 118:649, 1996.

[191] I. Borzsak and P. T. Cummings. Electrofreezing of water in molecular dynamics simulation accelerated by oscillatory shear. *Physical Review E*, 56:R6279–R6282, 1997.

[192] H. Qiu and W. Guo. Electromelting of confined monolayer ice. *Physical Review Letters*, 110:195701–195705, 2013.

[193] E. C. Bingham. An investigation of the laws of plastic flow. *Bulletin of the Bureau of Standards*, 13:309–353, 1916.

[194] T. Hynninen, V. Heinonen, C. L., Dias, M. Karttunen, A. S. Foster, and T. Ala-Nissila. Cutting ice: nanowire regelation. *Physical Review Letters*, 105, 2010.

Aalto-DD 217/2013

ISBN 978-952-60-5509-1
ISBN 978-952-60-5510-7 (pdf)
ISSN-L 1799-4934
ISSN 1799-4934
ISSN 1799-4942 (pdf)

Aalto University
Aalto University School of Science
Department of Applied Physics
www.aalto.fi

BUSINESS + ECONOMY

ART + DESIGN + ARCHITECTURE

SCIENCE + TECHNOLOGY

CROSSOVER

DOCTORAL DISSERTATIONS